CFD ANALYSIS /OPTIMIZATION OF THERMO-ACOUSTIC INSTABILITIES IN LIQUID FUELLED AERO STATIONARY GAS TURBINE COMBUSTORS

A thesis submitted to The University of Manchester for the degree of
Doctor of Philosophy in the Faculty of Engineering and Physical Sciences

July 2010

Shenghui LEI

School of Mechanical, Aerospace and Civil Engineering

ABSTRACT

It has been recognized that the evaporation process is one of the pivotal mechanisms driving thermo-acoustic instability in gas turbines and rockets in particular. In this regard, this study is principally focused on studying the evaporation process relevant to thermo-acoustic instability from three complementary viewpoints in an effort to contribute to an overall instability model driven primarily by evaporation in gas turbine combustors. Firstly, a state of the art LES algorithm is employed to validate an evaporation model to be employed in predictive modelling regarding combustion instabilities. Good agreement between the numerical predictions and experimental data is achieved. Additionally, transient sub-critical droplet evaporation is investigated numerically. In particular, a numerical method is proposed to capture the extremely important pressure-velocity-density coupling. Furthermore, the dynamic system nonlinear behaviour encountered in classical thermo-acoustic instability is investigated. The Poincaré map is adopted to analyse the stability of a simple non-autonomous system considering a harmonic oscillation behaviour for the combustion environment. The bifurcation diagram of a one-mode model is obtained where the analysis reveals a variety of chaotic behaviours for some select ranges of the bifurcation parameter. The bifurcation parameter and the corresponding period of a two-mode dynamic model are calculated using both analytical and numerical methods. The results computed by different methods are in good agreement. In addition, the dependence of the bifurcation parameter and the period on all the relevant coefficients in the model is investigated in depth. Moreover, a discrete dynamic model accounting for both combustion and vaporization processes is developed. In terms of different bifurcation parameters relevant to either combustion or evaporation, various bifurcation diagrams are presented. As part of the nonlinear characterization, the governing process Lyapunov exponent is calculated and employed to analyze the stability of the particular dynamic system. The study has shown conclusively that the evaporation process has a significant impact on the intensity and nonlinear behaviour of the system of interest, vis-à-vis a model accounting for only the gaseous combustion process. Furthermore, two particular nonlinear control methodologies are adopted to control the chaotic behaviour displayed by the particular aperiodic motions observed. These algorithms are intended to be implemented for control of combustion instability numerically and experimentally to provide a rational basis for some of the control methodologies employed in the literature. Finally, a state of the art neural network is employed to identify and predict the nonlinear behaviour inherent in combustion instability, and control the ensuing pressure oscillations. Essentially, the NARMAX model is implemented to capture nonlinear dynamics relating the input and output of the system of interest. The simulated results accord with the results reported. Moreover, a control system using the NARMA-L2 algorithm is developed. The simulation conclusively points to the fact that the amplitude of pressure oscillations can be attenuated to an acceptable level and the controller proposed may be implemented in a practical manner.

DECLARATION

No portion of the work referred to in this thesis has been submitted in support of an application for another degree or qualification of this or any other university or institute of learning.

COPYRIGHT

i. The author of this thesis (including any appendices and/or schedules to this thesis) owns certain copyright or related rights in it (the "Copyright") and s/he has given The University of Manchester certain rights to use such Copyright, including for administrative purposes.

ii. Copies of this thesis, either in full or in extracts and whether in hard or electronic copy, may be made only in accordance with the Copyright, Designs and Patents Act 1988 (as amended) and regulations issued under it or, where appropriate, in accordance with licensing agreements which the University has from time to time. This page must form part of any such copies made.

iii. The ownership of certain Copyright, patents, designs, trade marks and other intellectual property (the "Intellectual Property") and any reproductions of copyright works in the thesis, for example graphs and tables ("Reproductions"), which may be described in this thesis, may not be owned by the author and may be owned by third parties. Such Intellectual Property and Reproductions cannot and must not be made available for use without the prior written permission of the owner(s) of the relevant Intellectual Property and/or Reproductions.

iv. Further information on the conditions under which disclosure, publication and commercialisation of this thesis, the Copyright and any Intellectual Property and/or Reproductions described in it may take place is available in the University IP Policy in any relevant Thesis restriction declarations deposited in the University Library, The University Library's regulations and in The University's policy on presentation of Theses.

ACKNOWLEDGEMENTS

First of all, I would like to express my deep gratitude to my supervisor, Professor Ali Turan. His enthusiastic encouragement, constant guiding and help were essential for carrying out my PhD studies and writing my thesis and scientific papers. I would also like to point out that his inspiration and his warm personality have won my highest respect.

I extend sincere appreciation to Dr. Sergei Utyuzhnikov, Professor Yang Zhang, Dr. Zheshu Ma, Professor Chibing Shen, Professor Shutang Liu, Professor Niaoqing Hu and Dr. Zhou Tian for providing their expert guidance. I would also like to thank my colleagues and friends, Jieyan Ma, Dr. Ran An, Amr Elbanhawy, Dr. Xuewu Dai, Qingfeng Xia, Leichao Yang, Qian Wang, Amel Boudjir, Dr. Rizwan Riaz, Dr. Melih Guleren, Liwei Chen, Khaled Al Farhany, Joseph Dawes, Y Mou, Yousuf Alhendal and Machimontorn Promtong for their support and many enlightening discussions.

I am deeply grateful to the university and the school for the ORS/MACE Scholarship. My special thanks also go to Simon Hood, Phil Dunne and Steve for their helps on parallel computation.

Last but not least, I would like to express my love and sincere thanks to my parents and my family for their endless love. In particular, I am deeply indebted to my wife, Wenjing Mo, for her constant patience and support.

To my family and my wife, Wenjing Mo

CONTENTS

LIST OF FIGURES

LIST OF TABLES

NOMENCLATURE

A	coefficients in discretization equations
$\bar{a}$	average speed of sound for the mixture
B	mass transfer number
c_0	sound speed
C_D	droplet drag coefficient
C_p	specific heat at constant pressure
C_v	specific heat at constant volume
$\overline{C}_v$	specific heats of gas/droplets mixture at constant volume
$\overline{C}_p$	specific heats of gas/droplets mixture at constant pressure
C_w	WALE constant
D	binary diffusion coefficient
d_p	particle diameter
E	oscillation energy in Chapter 6
E^*	modified oscillation energy
$e_{o,g}$	stagnation internal energy of gaseous species
$e_{o,d}$	stagnation internal energy of droplets
F^*	mass flux at cell surface in discretization equations

$\mathbf{F}_d$	inter-force between droplets and gases
G	Green function; filter function in Chapter 3
$\hat{h}_{fg}$	latent heat of evaporation
h	enthalpy
J_m	Bessel function of order m
k	thermal conductivity; constant in Chapter 6
k_n	waver number
L	Lyapunov exponent
L_s	mixing length of subgrid scales
m	mass fraction
$\dot{m}''$	mass flux
M_i	molecular weight of species *i*
Nu	Nusselt number
r	radial coordinate
R	radius
R_u	universal gas constant
$\overline{R}$	mass average gas constant for the gas/droplets mixture
Re	Reynolds number
Re_d	relative Reynolds number
p	pressure
Pr	Prandtl number
$\mathbf{Q'}$	combustion rate per unite volume
$\dot{Q}$	heat released by reactions
S	surface area; cell surface area
S_{ij}	rate-of-strain tensor

Sc	Schmidt number
Sc_t	SGS turbulent Schmidt number
Sh	Sherwood number
t	time
T	temperature
$\mathbf{u}$	velocity vector
u_i	velocity component ($i = 1, 2, 3$)
v_r	radial velocity
V	volume; modified velocity in Chapter 4
$V_{k,i}$	i-component of diffusion velocity V_k of species k
W	molecular weight
W_d	rate of conversion of droplets to gas
x	dimensionless radial coordinate
y	droplet distortion
Y_k	mass fraction of species k

Greek symbols

α	thermal diffusivity
β	proportionality constant in Chapter 6
γ	heat capacity ratio
$\bar{\gamma}$	ratio of heat heats for the gas/droplets mixture
δ_{ij}	Kronecker-delta function
ε	acoustic energy
η	amplitude function in Chapter 6
θ	dimensionless temperature

κ	Karman constant; ratio of droplets to the mass of gas in a unit volume of chamber in Chapter 6
λ	bifurcation parameter in Chapter 6
μ	dynamic viscosity; bifurcation parameter in Chapter 6
μ_t	subgrid-scale viscosity
ν	kinematic viscosity
ξ	dimensionless radius
$\dot{\xi}(\tau)$	$=\mathrm{d}\xi(\tau)/\mathrm{d}\tau$
ρ	density
σ_{ij}	stress tensor
σ_t	SGS turbulent Prandtl number
τ	dimensionless time
τ_{ij}	shear stress tensor
ϕ	flow variable
$\boldsymbol{\psi}_n$	mode shape

Subscripts

0	at initial time
1	fuel species
2	air
d	droplet
l	liquid phase
g	gaseous phase
s	surface of droplet

sat	saturation
∞	far away from droplet surface

Superscripts

$\prime$	correction part in Chapter 4; fluctuating part in Chapter 6
sgs	subgrid-scale
p	period in Chapter 6

CHAPTER 1

INTRODUCTION

1.1 Motivation

The problem of thermo-acoustic instability in practice can occur in many different ways with liquid-fuelled gas turbine combustors, which is more likely as a consequence of the interaction between the combustion chamber acoustics and one or more processes related to liquid injection, primary atomization, secondary atomization, chemical kinetics, evaporation and liquid heating and mixing. If compensating influences to attenuate the resulting oscillations are relatively weak, unsteady motions in combustors may reach sufficient amplitude which can interfere with the proper operation of the system, have serious impact on behaviour and performance of engines and even cause the impairment of components of combustors.

In the past, thermo-acoustic instability has been investigated experimentally, analytically and computationally. It has been extensively appreciated that nonlinear behaviour inherent to this problem is the key to have an in-depth understanding of the potential mechanisms. In addition, it is of particular significance to delineate comprehensive mechanisms for thermo-acoustic instability, as the bifurcation behaviour and the multiplicity of solutions for a given nonlinear system are seldom considered in the currently employed experimental and numerical studies (CFD) carried out for thermo-acoustic instability. Therefore, it is extremely necessary to study the nonlinear behaviour associated with thermo-acoustic instability using tools that can explore the variation of certain parameters covering the entire operational conditions. Such considerations also pointed out by Culick (2006), enforce the notion that each numerical (CFD) simulation is, in general, only one particular case and it is, to some extent, difficult to generalize limited results to gain a fundamental understanding of thermo-acoustic instability in totality.

Furthermore, as pointed out by Sirignano and co-workers (1989; 1994; 1996), the vaporization of droplets is the key process in the driving mechanism for thermo-acoustic instability in liquid fuelled gas turbine combustors and the simple steady state vaporization models routinely employed in the literature in the context of gas turbine combustion are not appropriate for use in the study of thermo-acoustic instability for vaporizing sprays, when the ambient is unsteady. Thus, the two-way coupling between the vaporization and acoustic fields for droplet should be paid more attention to. Moreover, as thermo-acoustic/combustion instability occurs, corresponding control methods should be employed to eliminate the interaction between heat released by reactions and acoustics in the combustion chamber.

1.2 Objective and Strategy

It has been recognized that the evaporation process is one of the key mechanisms driving thermo-acoustic instability in gas turbines and rockets in particular, as pointed out by Sirignano and co-workers (1989; 1994; 1996; 1999). In this regard, this crucial process is investigated in a progress update manner in this thesis. Furthermore, this study is primarily focused on studying the evaporation process relevant to thermo-acoustic instability from three complementary viewpoints in an effort to contribute to an overall instability model driven primarily by evaporation in gas turbine combustors. In terms of the vaporization of a single droplet surrounded by hot air, a detailed numerical simulation in conjunction with the pressure-velocity-density coupling is developed to capture the two-way coupling between the evaporation process and pressure oscillations inherent in thermo-acoustic instability, whereas the influence of forced convection effects is neglected, but is taken into account in the nonlinear analysis that follows by incorporating velocity dependent terms in the perturbation energy field. Moreover, Large Eddy Simulations (LES) in conjunction with appropriate evaporation model are used to validate evaporation cases. Since the environment outside droplets is relatively stationary (free from oscillations and hence quasi-steady), it is justifiable to employ the energy balance and the Frössling correlation to obtain the droplet temperature and droplet radius in the classical manner without the benefit of a detailed model to account for the unsteady influences, which however are crucially important for an oscillating environment as pointed out previously. Hence for this simple hydrodynamic validation case, the two-way coupling mentioned above can be neglected. Furthermore, work on nonlinear/chaotic analysis is required to delineate the entire operational map of relevant parameters regarding the nonlinear behaviour associated with thermo-acoustic instability, an effort that has seldom been attempted/accomplished in the past. As pointed out by Culick (2006), each numerical (CFD) simulation is, in general, only one particular case and it is, to some extent, difficult to generalize limited results to gain a fundamental understanding of thermo-acoustic instability in totality. The evaporation model used here can physically represent the mass transfer between the droplets and the host fluid as a monopole sound source is a crucial driver of thermo-acoustic instability. Consequently, the variation of certain parameters covering the entire operational conditions can be explored by the dynamic model accounting for intricate coupling between combustion, evaporation and acoustics. Additionally, Poincaré map and bifurcation are adopted to demonstrate the nonlinear performance and Lyapunov exponents are calculated to reveal the stability of the system. Moreover, different control algorithms are proposed to control thermo-acoustic instability.

1.3 Outline of the Thesis

In this thesis, the work done is arranged into 8 chapters. Chapter 2 presents a review regarding the problem of thermo-acoustic/combustion instabilities, which covers most of the relevant mechanisms reported in the literature, providing the background of this research.

Numerical simulations of liquid fuel injection, evaporation and mixing in a gas turbine combustion chamber are implemented using LES in Chapter 3. Validation of the numerical predictions is performed in comparison with the experimental data provided by Sommerfeld and Qiu (1998). This work is intended to validate the evaporation model, as a good primer for the future numerical studies on thermo-acoustic instabilities.

Transient analyses of sub-critical evaporation of fuel droplet are presented in Chapter 4. A detailed numerical simulation is implemented and the numerical method of pressure-velocity-density coupling is developed to capture the two-way coupling between the evaporation process and pressure oscillations inherent in thermo-acoustic instabilities.

Chapter 5 is concerned with the dynamic system nonlinear behaviour encountered in classical thermo-acoustic instability. The Poincaré map is adopted to analyze the stability of a simple non-autonomous system considering a harmonic oscillation behaviour for the combustion environment. The bifurcation diagram of a one-mode model is obtained. Moreover, the bifurcation parameter and the corresponding period of a two-mode dynamic model are calculated using both analytical and numerical methods. In addition, the dependence of the bifurcation parameter and the period on all the relevant coefficients in the model is investigated in depth.

In Chapter 6, a discrete dynamic model accounting for both combustion and vaporization processes is developed. In terms of different bifurcation parameters relevant to either combustion or evaporation, various bifurcation diagrams are presented. Furthermore, the Lyapunov exponent is calculated and employed to analyze the stability of the particular dynamic system. In addition, two particular nonlinear control methodologies are employed to control the chaotic behaviour displayed by the particular aperiodic motions observed. These algorithms are intended to provide a basis for some of the control methodologies numerically and experimentally employed in thermo-acoustic instability.

In terms of a typical gas turbine combustor, a state of the art neural network is employed to identify and predict the nonlinear behaviour inherent in combustion instability, and control the ensuing pressure oscillations in Chapter 7.

Finally, chapter 8 concludes the thesis with a summary regarding the results obtained. In addition, further work on the subject is put forward.

CHAPTER 2

BACKGROUND

2.1 Introduction

In this chapter, a brief review regarding the prior studies of thermo-acoustic/combustion instabilities reported in the literature is presented to build up the background on the subject under concern. The following sections primarily cover discussions on the driving mechanisms, stability criteria, numerical simulations, nonlinear/chaotic behaviour, and control of thermo-acoustic/combustion instabilities, which may benefit understanding the complexity of the problem of interest.

2.2 Mechanisms for Combustion Instabilities

It is presently realized that the heat release from chemical reactions is the main source of energy driving unsteady flow oscillations and the energy needed to induce unsteady motions is an exceedingly small fraction of the heat release (Culick and

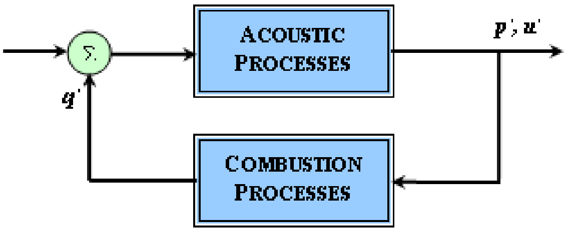

Fig. 2.1 Schematic Diagram of a Combustion System as a Feedback Amplifier

Yang, 1992; Culick and Yang, 1995). Nevertheless, combustion instabilities may not be excited and/or sustained unless a certain dynamic condition between heat release fluctuations and acoustic pressure oscillations is satisfied in a combustion chamber as shown in Fig. 2.1, which was first identified by Lord Rayleigh (1945). In his book, The Theory of Sound, a clear physical interpretation of the interchange of energy between sound waves and unsteady heating in a Rijke tube is given as

> "*If heat be periodically communicated to, and abstracted from, a mass of air vibrating (for example) in a cylinder bounded by a piston, the effect produced will depend upon the phase of the vibration at which the transfer of heat takes place. If heat be given to the air at the moment of greatest condensation, or be taken from it at the moment of greatest rarefaction, the vibration is encouraged. On the other hand, if heat be given at the moment of greatest rarefaction, or abstracted at the moment of greatest condensation, the vibration is discouraged.*" (Rayleigh, 1945)

which is the well-known Rayleigh criterion. It states that the amplitude of a sound wave will increase when heat is added in phase with its pressure perturbation, whereas the addition of heat out of phase with its pressure oscillation may attenuate the amplitude. Moreover, Chu (1965) proposed a generalized Rayleigh's criterion in a comprehensive manner, considering the effect of boundary conditions and viscous dissipation in addition to the exchange of energy between combustion and the acoustic waves. In the case of a combustor of volume *V* bounded by the surface *S* demonstrated in Fig. 2.2, it may be written as (Crighton et al., 1992)

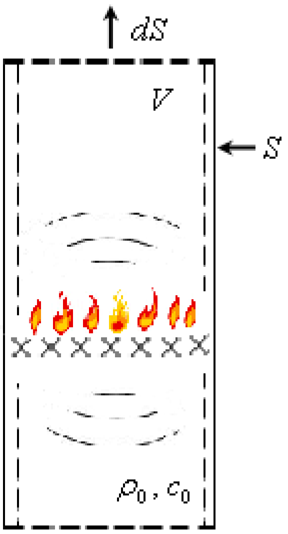

Fig. 2.2 Combustion within a Resonator

$$\frac{\partial}{\partial t}\int_V \varepsilon dV = \frac{\gamma-1}{\rho_0 c_0^2}\int_V p'\mathbf{Q}'dV - \int_S \left(p'u' - u'\tau_{ij}\right)dS - \int_V (\nabla\cdot u')\tau_{ij}dV \tag{2.1}$$

in which

$$\varepsilon = \frac{1}{2}\rho_0 u'^2 + \frac{1}{2}\frac{p'^2}{\rho_0 c_0^2} = \varepsilon_K + \varepsilon_P \tag{2.2}$$

where ε is the acoustic energy which contains the kinetic energy, ε_K, and potential energy, ε_P; ρ' and p' denote the perturbation in density and pressure, respectively; c_0 and ρ_0 are the mean values of sound speed and density, respectively; $\mathbf{Q}'$ represents the combustion rate per unit volume; γ is the ratio of specific heat , defined as the ratio of the heat capacity at constant pressure, C_p, to heat capacity at constant volume, C_v, viz., $\gamma = C_p/C_v$.

The term of the left-hand side of Equation (2.1) represents the rate of change of the acoustic energy within a combustion chamber; the first term of the right-hand side denotes the interchange between the combustion and the acoustic waves, which is intended to rise in the case of p' in phase with $\mathbf{Q}'$, as noted by Rayleigh (1945); the second term of the right-hand side denotes the loss of energy through the boundary, *S*; the last term is the loss of energy due to the viscous disspation. Equation (2.1) exhibits that the acoustic energy will grow, if the energy gain from combustion is greater than the entire losses of energy across the bounding surface and/or by the viscous dissipation. Therefore, the amplitude of acoustic modes will increase as the sum of the righ-hand side of Eq. (3.6) is positive, viz.,

$$\frac{\gamma-1}{\rho_0 c_0^2}\int_V \overline{p'\mathbf{Q}'}dV > \int_S \overline{\left(p'u' - u'\tau_{ij}\right)}dS - \int_V \overline{(\nabla \cdot u')\tau_{ij}}dV \qquad (2.3)$$

where $\overline{(\cdot)}$ denotes an average over one period of the acoustic oscillation. If this condition is satisfied, the thermo-acoustic/combustion instability consequently occurs. Furthermore, experimental and numerical findings have revealed that, during the growth of the amplitude of pressure perturbuation, the primary acoustic energy increases exponentially, and ultimately levels off at a certain limiting amplitude (defined as a limit cycle) owing to the nonlinear effects for a given system. In terms of some particular cases, the overshoot growth zone, in which the amplitude of pressure oscillation is slightly larger than the limit cycle amplitude, has been identified probably because of the inertia effect of the medium within the combustion chamber (Poinsot and Veynante, 2005).

As far as liquid-fuelled gas turbine combustors are concerned, thermo-acoustic/combustion instability can arise from various fundamental processes involved within a combustion chamber as summarized in Fig. 2.3. It was reported by Culick and Yang (1995) that the interactions between combustion chamber acoustics and one or more processes displayed in Fig. 2.3 may act as a mechanism for exciting and sustaining thermo-acoustic instability. Among candidate driving mechanisms, Sirignano et al. (1994) categorized three types of mechanisms. The first type is related to a combustion process which is rate controlling and has a characteristic time of the same order of the period of pressure oscillation, such as evaporation of droplets and chemical kinetics. The second type is associated with processes which may affect the characteristic time of some other rate-controlling process. An example of this type is atomization which has impact on the droplet distribution and, consequently, affects evaporation. The third type also has an indirect influence and may contribute to the spatial distribution of the combustion, which could generate variations in the local response associated with the coupling with a particular mode of acoustics, for example, mixing and injection.

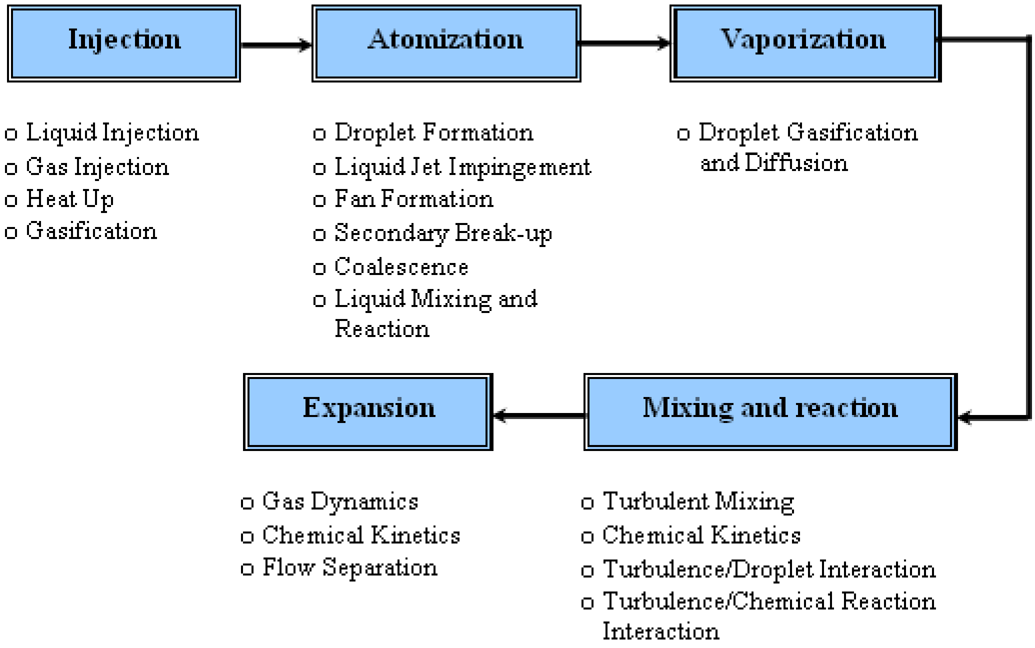

Fig. 2.3 Schematic Summary of Processes in Liquid-Fuelled Combustors

Particularly, in the past, the vaporization process, as one of the key factors driving thermo-acoustic instability, has been investigated by a number of researchers (Strahle, 1965; Harrje and Reardon, 1972; Culick, 1988; Tong and Sirignano, 1989; Sirignano et al., 1994; Duvvur, Chiang, Sirignano, 1996; Lei and Turan, 2009b). Compared with the other processes within combustion chamber, vaporization, in general, is the slowest, and hence may be the rate-controlling process, as argued by Sirignano et al. (1995). To understand the interaction of a vaporizing droplet with a surrounding oscillating field, transient droplet heating and vaporization have been studied by a number of researchers (Tong and Sirignano, 1989; Hsieh, Shuen and Yang, 1991; Delplanque and Sirignano, 1993; Abramzon and Sirignano, 1989; Chiang and Sirignano, 1993; Duvvur et al., 1996). Recently, the effect of the oscillating gas pressure and velocity on the evaporation rate of droplets was examined by Tong and Sirignano (1989) and it was revealed that, under certain circumstances, the vaporization-rate response function can be sufficient to induce combustion instability. More recently, using a detailed calculation of a single droplet surrounded by the oscillating field, Duvvur et al. (1996) concluded that for certain frequency ranges and initial droplet sizes, instabilities can arise in an evaporation-rate-controlled chamber owing to the vaporization process. Moreover, in terms of the vaporization process, a general Rayleigh criterion was evaluated by Sirignano and co-workers (Tong and Sirignano, 1989; Duvvur, Chiang and Sirignano, 1996). The growth and decay of the wave can be determined by the net in-phase or out-of-phase mass addition (Sirignano, 1999). Therefore, the method involving modulations of the evaporation process for liquid fuels has been extensively employed to control combustion instability (Sattinger et al., 2000; Dowling and Morgans, 2005; Lee, Lubaarsky and Zinn, 2005; Paschereit and Gutmark, 2008).

2.3 Acoustic Motions in Combustion Chambers

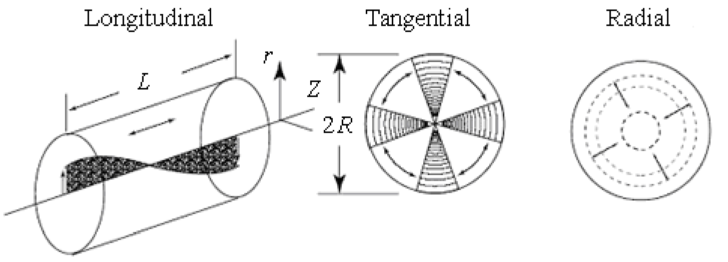

Fig. 2.4 Acoustic Modes of a Cylindrical Chamber

As mentioned above, combustion instabilities are, in general, characterized by the coupling between combustion processes and acoustic motions within a combustion chamber. In terms of a cylindrical chamber with length L and radius R as shown in Fig.

2.4, the corresponding acoustic modes (l, m, s) for each frequency are expressed as (Yang, Wicker and Yoon, 1995; Poinsot and Veynante, 2005)

$$\psi_n(r,\theta,z) = \cos\left[\left(\frac{\pi l}{L}\right)\cdot z\right] J_m(\pi\beta_{ms} r / R)\begin{Bmatrix}\cos(m\theta)\\ \sin(m\theta)\end{Bmatrix}, \quad \begin{cases} l = 0, 1, 2, ... \\ m = 0, 1, 2, ... \\ s = 0, 1, 2, ... \end{cases} \tag{2.4}$$

where l, m and s represent the longitudinal, tangential and radial mode numbers, respectively; (r, θ, z) represent cylindrical coordinates; J_m is the Bessel function of order m; the values of β_{ms} are the roots of $J'_m(\pi\beta_{ms}) = 0$.

Fig. 2.4 displays three types of acoustic modes in the chamber under consideration. Although there are, in nature, infinite acoustic modes existing in the chamber, just certain modes excited can interact with the combustion processes, a fact that has been recognized experimentally, numerically and analytically (Yang et al., 1995; Huang et al., 2003; Huang and Yang, 2005; Culick, 2006). Furthermore, it should be noted that the mutual coupling between acoustic modes may occur and the acoustic energy can be transferred from lower modes to higher modes and vice versa owing to the nonlinear gasdynamics in a chamber, as reported by Ananthkrishnan et al. (2005).

2.4 Numerical Simulations on Gas Turbine Combustors

One of the challenging difficulties on combustion instability studies is that the vortices created during instabilities are generally never observed in stable regimes (Poinsot and Veynante, 2005). Therefore, appropriate numerical methods are required to capture large-scale vortices in reacting flows for combustion instabilities. In the past, a state of the art computational fluid dynamics (CFD) has been extensively employed for gas turbine combustion chambers (Baum and Levine, 1982, 1983, 1988; Lupoglazoff and Vuillot, 1991; Menon and Jou, 1991; Wang, 1997; Kim, et al., 1999; Angelberger, Veynante and Egolfopoulos, 2000; Huang et al., 2003; Roux et al., 2005; Selle, Benoit et al., 2006; Selle, Lartigue et al., 2006; Menon and Patel, 2006; Martin et al., 2006; Schmitt, Poinsot et al., 2007). In particular, Large Eddy Simulations (LES) of reactive flows are utilized as a standard technique for understanding combustion instabilities, since LES can capture large-scale vortices in reacting flows and mimic the fine-scale turbulent structures indirectly by a subgrid model. In addition, because combustion instability mainly depends on very large scale structures, LES may perform better to characterize the dynamics of turbulent flame.

Kim et al. (1999) investigated a swirl-stabilized gas turbine combustor flow, and a complex vortex shedding pattern with significant azimuthal structures was identified. The combustion dynamics in a lean-premixed swirl-stabilized gas-turbine combustor was reported by Huang et al. (2003). More recently, LES in conjunction with acoustic flame-acoustic modelling and the NSCBC (Navier-Stokes Characteristic Boundary Conditions) method was employed to predict combustion instability for premixed gas turbine combustors by Poinsot and co-workers (Selle et al., 2004; Roux et al., 2005; Selle, Benoit et al., 2006; Selle, Lartigue et al., 2006; Martin et al., 2006; Schmitt, Poinsot et al., 2007). However, in terms of the liquid-fuelled gas turbine combustors, few studies regarding thermo-acoustic/combustion instability have been reported due to the complicated processes particularly involving atomization and vaporization of the liquid fuel. In the past, more efforts on multiphase reacting flows have been made to validate the detailed processes within liquid-fuelled combustors, such as droplet dispersion, droplet evaporation, breakup etc. (Apt, Gorokhovski and Moin, 2003; Moin and Apte, 2006; Menon and Patel, 2006).

2.5 Nonlinear Behaviours of Combustion Instability

As discussed in Section 2.2, there are various resulting performances involving the limit cycle emerged in gas turbine combustors, which may be stemmed from the nonlinear effects. Hence, it is primarily necessary to identify the nonlinear/chaotic behaviours inherent in thermo-acoustic/combustion instabilities. Historically, the analytical methods can be categorized into two groups characterized as linear analysis (Culick, 1961; Culick, 1963) and nonlinear analysis chronologically. In particular, the various nonlinear behaviours observed in combustion instability have been investigated experimentally, analytically and computationally by a number of authors (Culick, 1976a, 1976b; Dubinkin et al., 1978; Levine and Baum; 1981; Yang, Kim and Culick, 1988, 1990; Sterling, 1993; Huang et al., 2002; Ananthkrishnan et al., 2005; Lieuwen, 2002; Lei and Turan, 2009a, 2009b). Culick (1976a, 1976b) put forward a second-order nonlinear dynamic model using the Galerkin method, which was extended to third-order by Yang et al. (Yang, Kim and Culick, 1987, 1988). This dynamic model is widely utilized to analyze the nonlinear behaviour inherent in combustion instability for a combustion chamber. The triggering conditions for the different modes in the chamber were given by Yang, Kim and Culick (1987, 1988, 1990). The bifurcation phenomena and the transitional process were reported by Sterling (1993). The limit cycle occurring in solid rocket motors was discussed using a numerical method by Levine and Baum (1981). The bifurcation occurring in a dump combustor was confirmed by experiments in literature (Lieuwen and Yang, 2005). More recently, to understand fully the underlying mechanisms relevant to combustion instability, nonlinear analyses have been employed in a more comprehensive manner (Dubinkin et al., 1978; Levine and Baum, 1981; Sterling, 1993; Huang et al., 2002; Lieuwen, 2002; Ananthkrishnan et al., 2005). Huang et al. (2002) argued that the heat transfer coefficient between the wall and the burned gas is an important bifurcation parameter for the combustion instability. Ananthkrishnan et al. (2005) stated the dependence of the inter-modal energy transfer on the relevant parameters and reported the existence of a Hopf bifurcation related to thermo-acoustic instability. The bifurcation behaviour of a flame in a combustion chamber was reported in the work (Dubinkin et al., 1978). The fractal dimension of the corresponding attractors associated with the acoustic modes participating in the pressure oscillations in a combustion chamber was outlined by Sterling (1993). Lei and Turan (2009a) identified the nonlinear/chaotic behaviour inherent in thermo-acoustic instability using dynamic models based on reasonable considerations. The hysteresis inherent to combustion instability was revealed in addition to other interesting phenomena. Moreover, a discrete dynamic model accounting for both combustion and vaporization processes was developed (Lei and Turan, 2009b). In terms of the different bifurcation parameters related to combustion and/or evaporation, various bifurcation diagrams are correspondingly presented. In addition, the governing process Lyapunov exponent was calculated and employed to analyze the stability of the particular dynamic system.

2.6 Control of Combustion Instabilities

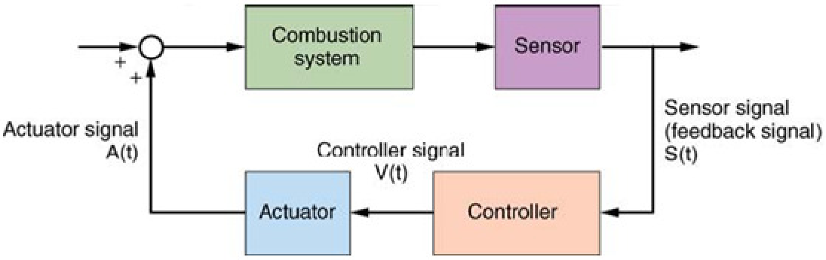

Fig. 2.5 Genetic System for Active Control of Combustion Instabilities

The generalized Rayleigh criterion given by Equation (2.3) in essence demonstrates the measurements taken to eliminate thermo-acoustic instability in terms of a certain system. Physically, the damping sources by the bounding surface and/or viscous dissipation should be enhanced and, alternatively, the interaction of combustion with acoustics, $\int_V \overline{p'\mathbf{Q}'} dV$, should be interrupted. In the past, to reverse this criterion, passive control and active control have been used (Tsien, 1952; Putnam, 1971; Lang, Poinsot et al., 1987; Bloxsidge et al., 1988; Culick 1988; Langhorne, Dowling and Hooper, 1990; Richards and Janus, 1998; Steele et al. 2000; Eldredge and Dowling 2003; Richards et al. 2003; Dowling and Morgans, 2005; Coker, 2006; Conrad, Zinn et al., 2007; Morgans and Stow, 2007; Richards et al., 2007; Yi and Gutmark, 2008; Morgans and Annaswamy, 2008; Cohen et al., 2008). For passive control, the insertion of baffles within the combustor (Richards and Janus 1998; Steele et al., 2000) or the installation of Helmholtz resonators (Gysling et al., 2000; Bellucci et al., 2004), quarter wave tubes (Joshi et al., 1994), perforated plates, or acoustic liners (Eldredge and Dowling, 2003) was applied to attenuate thermo-acoustic instability. However, the problems associated with passive approaches are that they tend to be effective only over a limited range of operating conditions, they may be ineffective at the low frequencies at which some of the most damaging instabilities occur, and the changes of design involved are usually costly and time consuming, as pointed out by Dowling and Morgans (2005). Alternatively, active control of combustion instabilities has demonstrated more advantages in applicability and effectiveness. A genetic system of active control is given in Fig. 2.5 (Dowling and Morgans, 2005), in which an actuator is exerted to modify a certain system parameter according to a feedback signal measured, and the relationship between the measured signal and the signal used to drive the actuator is appropriately specified by the controller to decouple the interaction between the unsteady heat release and acoustic waves (Langhorne, Dowling and Hooper, 1990; Richards et al., 2007; Yi and Gutmark, 2008). In particular, Lei and Turan (2010c) identified and predicted the nonlinear behaviour inherent in combustion instability and correspondingly developed a control system using a state of the art neural network.

CHAPTER 3

MODELLING OF LIQUID FUEL INJECTION, EVAPORATION AND MIXING IN A GAS TURBINE COMBUSTION CHAMBER USING LES

3.1 Introduction

To obtain high-fidelity numerical solution of reacting flows associated with liquid-fuelled gas turbine combustors, it is required to accurately capture momentum coupling, mass and energy interaction, subgrid-scale (SGS) modulation of turbulence, the resulting turbulent combustion processes, etc. As part of an effort to capture these phenomena mentioned above, the two-phase flow in a coaxial combustion chamber is studied. The primary objectives of this work are to have an in-depth understanding of the effectiveness and limitations of current state-of-art SGS models and evaporation model.

In the past, most numerical studies emphasized the particle-turbulence coupling in simplified geometries and the influences of gas-phase velocity fluctuations on the particle dispersion behaviour (Eaton and Fessler, 1994; Maxey and Patel, 2001; Apte et al., 2003). Here, these analyses, by taking advantage of the most recent modelling approach in conjunction with LES, are extended and validated to make this state-of-art framework feasible for more complex systems in the future work.

3.2 Formulation

3.2.1 Gas Phase LES Equations

Generally, to obtain the governing equations employed for LES, the time-dependent Navier-Stokes equations are filtered in either the Fourier (wave-number) space or configuration (physical) space (Pope, 2000; Poinsot and Veynante, 2005). The filtering operation can effectively eliminate eddies with the scales smaller than the filter width or grid spacing specified in the computations. In FLUENT (2006), the space filtering procedure is used and a filtered variable is defined as

$$\widetilde{\phi}(\mathbf{x}) = \frac{1}{V}\iiint_{V}\phi(\mathbf{x}')d\mathbf{x}', \quad \mathbf{x}' \in V \tag{3.1}$$

where V is the volume of a computational cell. The filter function, $G(\mathbf{x},\mathbf{x}')$, adopted here is

$$G(\mathbf{x},\mathbf{x}') = \begin{cases} \frac{1}{V}, & \mathbf{x}' \in V \\ 0, & \mathbf{x}'\,\mathbf{otherwise} \end{cases} \tag{3.2}$$

Thus, the governing equations by filtering the instantaneous balance equations are obtained as:

Mass

$$\frac{\partial\bar{\rho}}{\partial t}+\frac{\partial}{\partial x_i}(\bar{\rho}\tilde{u}_i)=\overline{\dot{m}}_s \tag{3.3}$$

Momentum

$$\frac{\partial\bar{\rho}\tilde{u}_i}{\partial t}+\frac{\partial}{\partial x_j}\left(\bar{\rho}\tilde{u}_i\tilde{u}_j\right)=-\frac{\partial\bar{p}}{\partial x_i}+\frac{\partial}{\partial x_j}\left[\tilde{\sigma}_{ij}-\bar{\rho}\left(\widetilde{u_iu_j}-\tilde{u}_i\tilde{u}_j\right)\right]+\overline{\dot{F}}_{i,s} \tag{3.4}$$

Chemical Species

$$\frac{\partial\bar{\rho}\tilde{Y}_k}{\partial t}+\frac{\partial}{\partial x_j}\left(\bar{\rho}\tilde{u}_j\tilde{Y}_k\right)=\frac{\partial}{\partial x_j}\left[-\widetilde{V_{k,i}Y}-\bar{\rho}\left(\widetilde{Y_ku_j}-\tilde{Y}_k\tilde{u}_j\right)\right]+\overline{\dot{S}}_{k,s},\quad k=1,N \tag{3.5}$$

Energy

$$\begin{aligned}\frac{\partial\bar{\rho}\tilde{h}_s}{\partial t}+\frac{\partial}{\partial x_j}\left(\bar{\rho}\tilde{u}_j\tilde{h}_s\right)=\widetilde{\frac{Dp}{Dt}}+\frac{\partial}{\partial x_j}\left(\widetilde{\lambda\frac{\partial T}{\partial x_j}}-\bar{\rho}\left(\widetilde{h_su_j}-\tilde{h}_s\tilde{u}_j\right)\right)\\+\overline{\sigma_{ij}\frac{\partial u_i}{\partial x_j}}-\frac{\partial}{\partial x_j}\left(\widetilde{\bar{\rho}\sum_{k=1}^{N}V_{k,i}Y_kh_{s,k}}\right)+\overline{\dot{Q}}_{k,s}\end{aligned} \tag{3.6}$$

where $V_{k,i}$ is the i-component of the diffusion velocity V_k of species k; $\overline{\dot{m}}_s$, $\overline{\dot{F}}_{i,s}$, $\overline{\dot{S}}_{k,s}$ and $\overline{\dot{Q}}_{k,s}$ represent the source terms in continuity, momentum, species and energy equations, respectively;

$$\widetilde{\frac{Dp}{Dt}}=\frac{\partial\tilde{p}}{\partial t}+\widetilde{u_i\frac{\partial p}{\partial x_i}} \tag{3.7}$$

and $\tilde{\sigma}_{ij}$ is the stress tensor due to molecular viscosity given as

$$\tilde{\sigma}_{ij} = \left[\mu \left(\frac{\partial \tilde{u}_i}{\partial x_j} + \frac{\partial \tilde{u}_j}{\partial x_i} \right) - \frac{2}{3} \mu \frac{\partial \tilde{u}_l}{\partial x_l} \delta_{ij} \right] \tag{3.8}$$

In terms of filtered laminar diffusion fluxes for species and enthalpy, these molecular fluxes may be modelled through a gradient assumption, viz.

$$\widetilde{V_{k,i} Y_k} = -\bar{\rho} \bar{D}_k \frac{\partial \tilde{Y}_k}{\partial x_i} \; ; \; \overline{\lambda \frac{\partial T}{\partial x_j}} = \bar{\lambda} \frac{\partial \tilde{T}}{\partial x_j} \tag{3.9}$$

and the energy flux $\bar{q}_i$ is defined as

$$\bar{q}_i = -\bar{\lambda} \frac{\partial \tilde{T}}{\partial x_i} + \bar{\rho} \left(\sum_{k=1}^{N} \bar{h}_{s,k} \bar{D}_k \frac{\partial \tilde{Y}_k}{\partial x_i} \right) \tag{3.10}$$

In addition, the subgrid terms representing the subgrid-scale stress tensor τ_{ij}^{sgs}, the subgrid heat flux $h_{s,j}^{sgs}$, the subgrid viscous work T_j^{sgs}, the subgrid species mass fraction flux $Y_{k,j}^{sgs}$ and the subgrid enthalpy flux q_j^{sgs}, are respectively defined as

$$\tau_{ij}^{sgs} = -\bar{\rho} \left(\widetilde{u_i u_j} - \tilde{u}_i \tilde{u}_j \right) \tag{3.11}$$

$$h_{s,j}^{sgs} = -\bar{\rho} \left(\widetilde{h_s u_j} - \tilde{h}_s \tilde{u}_j \right) \tag{3.12}$$

$$T_j^{sgs} = -\bar{\rho} \left(\widetilde{\sigma_{ij} u_i} - \tilde{\sigma}_{ij} \tilde{u}_i \right) \tag{3.13}$$

$$Y_{k,j}^{sgs} = -\bar{\rho} \left(\widetilde{Y_k u_j} - \tilde{Y}_k \tilde{u}_j \right) \tag{3.14}$$

$$q_j^{sgs} = -\bar{\rho} \sum_{k=1}^{N} \left[\overline{h_{s,k} D_k \frac{\partial Y_k}{\partial x_j}} - \bar{h}_{s,k} \bar{D}_k \frac{\partial \tilde{Y}_k}{\partial x_i} \right] \tag{3.15}$$

and the pressure-velocity term in Equation (3.7) is approximated by

$$\widetilde{u_i \frac{\partial p}{\partial x_i}} = \tilde{u}_i \frac{\partial \tilde{p}}{\partial x_i} \tag{3.16}$$

Consequently, the Favre filtered Navier-Stokes equations for mass, momentum, species and energy may be rewritten as (Poinsot and Veynante, 2005)

$$\frac{\partial \bar{\rho}}{\partial t} + \frac{\partial}{\partial x_i}\left(\bar{\rho}\tilde{u}_i\right) = \overline{\dot{m}}_s \tag{3.17}$$

$$\frac{\partial \bar{\rho}\tilde{u}_i}{\partial t} + \frac{\partial}{\partial x_j}\left(\bar{\rho}\tilde{u}_i\tilde{u}_j\right) = -\frac{\partial \bar{p}}{\partial x_i} + \frac{\partial\left(\tilde{\sigma}_{ij} + \tau_{ij}^{sgs}\right)}{\partial x_j} + \overline{\dot{F}}_{i,s} \tag{3.18}$$

$$\frac{\partial \bar{\rho}\tilde{Y}_k}{\partial t} + \frac{\partial}{\partial x_j}\left(\bar{\rho}\tilde{u}_j\tilde{Y}_k\right) = \frac{\partial}{\partial x_j}\left(\bar{\rho}\bar{D}\frac{\partial \tilde{Y}_k}{\partial x_j}\right) + \frac{\partial Y_{k,j}^{sgs}}{\partial x_j} + \overline{\dot{S}}_{k,s}, \quad k = 1, N \tag{3.19}$$

$$\frac{\partial \bar{\rho}\tilde{h}_s}{\partial t} + \frac{\partial}{\partial x_j}\left[\left(\bar{\rho}\tilde{h}_s + \bar{p}\right)\tilde{u}_j + \bar{q}_j\right] = \frac{\partial}{\partial x_j}\left(\tilde{u}_i\tilde{\sigma}_{ij} + h_{s,j}^{sgs} + T_j^{sgs} + q_j^{sgs}\right) + \overline{\dot{Q}}_{k,s} \tag{3.20}$$

It should be noted that in these filtered equations, the unresolved SGS terms involving τ_{ij}^{sgs} , $h_{s,j}^{sgs}$, T_j^{sgs} , $Y_{k,j}^{sgs}$ and q_j^{sgs} must be modelled to close the system of interest.

3.2.2 SGS Fluxes Modelling

This section is to provide the closure models regarding the unresolved SGS fluxes discussed above including SGS stresses $\left(\widetilde{u_i u_j} - \tilde{u}_i\tilde{u}_j\right)$, SGS mass fraction fluxes $\left(\widetilde{Y_k u_j} - \tilde{Y}_k\tilde{u}_j\right)$, SGS enthalpy fluxes $\left(\widetilde{h_s u_j} - \tilde{h}_s\tilde{u}_j\right)$ and all the other SGS terms.

Wall-Adapting Local Eddy-Viscosity (WALE) Model

In the past decades, considerable SGS models have been proposed. Among these models, the Smagorinsky-Lilly model (Smagorinsky, 1963; Lilly, 1966) is popular due to its simple formulation. To remove the uncertainties inherent in the Smagorinsky-Lilly Model in terms of the Smagorinsky coefficient, the Dynamic Smagorinsky-Lilly Model was developed by Germano et al. (1991). More recently, the Wall-Adapting Local Eddy-Viscosity (WALE) Model was proposed by Nicoud and Ducros (1999) and the Dynamic Kinetic Energy Model was developed by Kim and Menon (1995). In this work, WALE is employed to calculate the SGS viscosity.

To calculate the subgrid-scale stresses resulting from the filtering operation, Boussinesq hypothesis (Hinze, 1975) is used

$$\tau_{ij} - \frac{1}{3}\tau_{kk}\delta_{ij} = -2\mu_t \bar{S}_{ij} \tag{3.21}$$

where μ_t is the subgrid-scale turbulent viscosity; τ_{kk} represents the isotropic part of the subgrid-scale stresses, which, in FLUENT, is added to the filtered static pressure term; δ_{ij} is the Kronecker-delta function; $\bar{S}_{ij}$ is the rate-of-strain tensor for the resolved scale defined by

$$\bar{S}_{ij} = \frac{1}{2}\left(\frac{\partial \tilde{u}_i}{\partial x_j} + \frac{\partial \tilde{u}_j}{\partial x_i}\right) \tag{3.22}$$

Furthermore, WALE may be employed to obtain the SGS viscosity shown in Equation (3.21), which takes into consideration both the effects of strain and rotation rates. Thus, the SGS viscosity is defined as

$$\mu_t = \bar{\rho} L_s^2 \frac{\left(S_{ij}^d S_{ij}^d\right)^{\frac{3}{2}}}{\left(\bar{S}_{ij}\bar{S}_{ij}\right)^{\frac{5}{2}} + \left(S_{ij}^d S_{ij}^d\right)^{\frac{5}{4}}} \tag{3.23}$$

where

$$S_{ij}^d = \frac{1}{2}\left(\bar{g}_{ij}^2 + \bar{g}_{ji}^2\right) - \frac{1}{3}\delta_{ij}\bar{g}_{kk}^2 \tag{3.24}$$
$$\bar{g}_{ij} = \frac{\partial \tilde{u}_i}{\partial x_j}$$

and L_s is the mixing length for subgrid scales computed using

$$L_s = \min\left(\kappa d, C_w V^{\frac{1}{3}}\right) \tag{3.25}$$

in which κ is the von Kármán constant, d is the distance to the closest wall, C_w is the WALE constant, and V is the volume of the computational cell.

It should be noted that the true behaviour of the flow near the walls including transition effects and laminarization may be captured using WALE. The model constant, C_w, is specified to be 0.325 in order to consider both anisotropy and non-homogeneity inherent in the turbulent flow, as pointed out by Nicoud and Ducros (1999).

Unresolved Scalar Fluxes

The SGS mass fraction fluxes and the SGS heat fluxes are modelled using a gradient assumption given as (Poinsot and Veynante, 2005)

$$\widetilde{Y_k u_j} - \tilde{Y}_k \tilde{u}_j = -\frac{\nu_t}{Sc_t}\frac{\partial \tilde{Y}_k}{\partial x_j} \tag{3.26}$$

$$\widetilde{h_s u_j} - \tilde{h}_s \tilde{u}_j = -\frac{\nu_t}{\sigma_t}\frac{\partial \tilde{h}_s}{\partial x_j} \tag{3.27}$$

where Sc_t is the SGS turbulent Schmidt number and σ_t is the SGS turbulent Prandtl number. In addition, the other SGS terms including subgrid viscous work T_j^{sgs} and the subgrid enthalpy fluxes q_j^{sgs} are neglected in FLUENT.

3.2.3 Liquid Phase Treatment

To model the spray, the discrete phase model (DPM) is employed. Assuming that that each parcel has droplet particles with the same properties including droplet diameter, speed and temperature etc., the droplet parcels (groups of droplets) are tracked spatially and temporally using a Lagrangian formulation, in which the discrete phase and the continuous phase are coupled through source terms in the governing equations involving mass/species sources owing to evaporation, momentum source by the change of momentum of the phases, energy source due to heat transfer between two phases and/or the temperature variation through evaporation etc. Note that in this work, two-way coupling is taken into consideration, which indicates that source terms of both liquid phase and gaseous phase are updated in the computation.

Droplet Trajectory

To obtain the position of a parcel, one could explicitly integrate the parcel equation of motion

$$\mathbf{x}_p^{n+1} = \mathbf{x}_p^n + \int_{t_n}^{t_{n+1}} \mathbf{u}_p dt \tag{3.28}$$

where $\mathbf{x}_p^n$ is the location of the parcel at previous time step, t_n, and $\mathbf{u}_\mathrm{p}$ is the instantaneous parcel velocity updated by integrating the force balance on the parcel, which is written in a Lagrangian reference frame as

$$\frac{d\mathbf{u}_p}{dt} = F_D\left(\mathbf{u} - \mathbf{u}_p\right) \tag{3.29}$$

where $F_D\left(\mathbf{u} - \mathbf{u}_p\right)$ is the drag force per unit particle mass and

$$F_D = \frac{18\mu}{\rho_p d_p^2} \cdot \frac{C_D \operatorname{Re}_d}{24} \tag{3.30}$$

in which **u** is the gas phase velocity obtained using the filtered LES velocity, μ is the molecular viscosity of the fluid, ρ_g is the gas density, ρ_p is the density of the particle, d_p is the particle diameter, Re_d is the relative Reynolds number defined as

$$\operatorname{Re}_d = \frac{\rho_g d_p \left|\mathbf{u}_p - \mathbf{u}\right|}{\mu} \tag{3.31}$$

and C_D is the droplet drag coefficient calculated using

$$C_D = \begin{cases} \frac{24}{\operatorname{Re}_d}\left[1 + \frac{1}{6}\operatorname{Re}_d^{\frac{2}{3}}\right], & \mathit{if}\ \operatorname{Re}_d \le 1000 \\ 0.424, & \mathit{if}\ \operatorname{Re}_d > 1000 \end{cases} \tag{3.32}$$

which have been validated to yield a good agreement with experimental results by Caraeni et al. (2000). Additionally, in this work, other forces including gravity are neglected in the similar manipulation done by Caraeni et al. (2000) and James et al. (2006). Moreover, to account for the effects of droplet distortion, a modification regarding the drag coefficient proposed by Liu et al. (1993) is used as

$$C_D^* = C_D\left(1 + 2.632y\right) \tag{3.33}$$

where y is the droplet distortion, which is calculated in the same manner as the break-up process discussed later. Note that in the limit of no distortion, viz. y = 0, the drag coefficient of a sphere will be obtained, whereas at maximum distortion, viz. $y = 1$, the drag coefficient corresponding to a disk will be obtained.

Evaporation Model

The evaporation sub-model used in this work is based on the assumptions that the evaporation process may be regarded as representing single droplet evaporation and the droplets have homogeneous temperature and constant density. First of all, the droplet temperature is updated according to an energy balance related to the sensible heat change in the droplet and the convective and latent heat transfer between two phases, given as

$$\frac{4\pi r_p^3}{3}\rho_p C_{p,l}\frac{dT_d}{dt} - 4\pi r_p^2\frac{dr_p}{dt}L(T_d) = 4\pi r_p^3 Q_d \tag{3.34}$$

where $C_{p,l}$ is the liquid specific heat and $L(T_d)$ is the latent heat of evaporation and Q_d is the rate of heat conduction define using Ranz-Marshall correlation as

$$Q_d = \frac{\alpha(T_f)\cdot(T_g - T_d)}{2r_p}Nu_d \tag{3.35}$$

where $\alpha(T_f)$ is the thermal diffusivity, T_f is the film temperature defined using "1/3" rule, $T_f = T_d + 1/3(T_g - T_d)$, T_g and T_d are the gas and the droplet temperature respectively, and Nu_d is the Nusselt number taken as

$$Nu_d = 2.0 + 0.6\,\mathrm{Re}_d^{\frac{1}{2}}\,\mathrm{Pr}_d^{\frac{1}{3}} \tag{3.36}$$

in which Pr_d is the Prandtl number

$$\mathrm{Pr}_d = \frac{\mu_g(T_f)C_{p,g}(T_f)}{\alpha(T_f)} \tag{3.37}$$

where $C_{p,g}$ is the gas specific heat at constant pressure and μ_g is the gas viscosity. Note that the enthalpies, liquid vapour pressure and other properties for the material of interest are specified to be temperature-dependent (Polling et al., 2001).

In addition, the Frössling correlation is employed to obtain the droplet radius rate of change due to evaporation given as

$$\frac{dr_p}{dt} = -\frac{\rho_g D_m(T_f) B_d}{2\rho_p r_p} Sh \tag{3.38}$$

where D_m is the fuel diffusivity in the mixture, B_d is the mass transfer number and Sh is the Sherwood number, given respectively by

$$B_d = \frac{Y_l^s - Y_l}{1 - Y_l^s} \tag{3.39}$$

$$Sh = 2.0 + 0.6 Re_d^{\frac{1}{2}} Sc_d^{\frac{1}{3}} \tag{3.40}$$

$$Sc_d = \frac{\mu_g(T_f)}{\rho_g D_m(T_f)} \tag{3.41}$$

in which Y_l is the fuel vapour mass fraction, Sc_d is the Schmidt number and Y_l^s is the fuel mass fraction at the droplet surface obtained using Raoult's law

$$Y_l^s = \frac{W_l}{W_l + W_g\left(\frac{p}{p_v} - 1\right)} \tag{3.42}$$

where p_v is the liquid vapour pressure and p is the ambient pressure; W_g and W_l are the molecular weights for liquid and gaseous phases, respectively.

Breakup Model

Considering Webber number associated with this case of interest, the Taylor analogy breakup (TAB) model developed by Taylor (1963) and O'Rourke and Amsden (1987) is employed to model droplet break-up process. This method is based on Taylor's analogy (Taylor, 1963) between an oscillating and distorting droplet and a spring mass system. The distortion equation is given as:

$$\frac{d^2 y}{dt^2} = \frac{C_F}{C_b}\frac{\rho_g}{\rho_p}\frac{u_r^2}{R^2} - \frac{C_k \sigma}{\rho_p R^3} y - \frac{C_d \mu_p}{\rho_p R^2}\frac{dy}{dt} \tag{3.43}$$

where u_r is the relative velocity of the droplet, R is the undisturbed droplet radius, and σ is the droplet surface tension, μ_p is the droplet viscosity; C_k, C_F, C_d, and C_b are model constants, which in this work, are taken as 8.0, 1/3, 5.0 and 0.5, respectively, to match experiments (Lamb, 1945). Assuming the relative velocity is constant, one may obtain the solution of Equation (3.43)

$$y(t) = We_c + e^{-(t/t_d)}\left[(y_0 - We_c)\cos(\omega t) + \frac{1}{\omega}\left(\frac{dy_0}{dt} + \frac{y_0 - We_c}{t_d}\right)\sin(\omega t)\right] \tag{3.44}$$

where

$$We = \frac{\rho_g u_r^2 r}{\sigma} \tag{3.45}$$

$$We_c = \frac{C_F}{C_k C_b} We \tag{3.46}$$

$$\omega = \left(C_k \frac{\sigma}{\rho_p r^3} - \frac{1}{t_d^2}\right)^{\frac{1}{2}} \tag{3.47}$$

$$\frac{1}{t_d} = \frac{C_d}{2}\frac{\mu_l}{\rho_p r^2} \tag{3.48}$$

$$y_0 = y(0) \tag{3.49}$$

$$\frac{dy_0}{dt} = \frac{dy(0)}{dt} \tag{3.50}$$

in which *We* is the droplet Weber number and *ω* is the droplet oscillation frequency. In addition, breakup occurs, provided the following condition is satisfied

$$We_c + A > 1 \tag{3.51}$$

where *A* is the amplitude for an undamped oscillation defines as

$$A = \left[(y - We_c)^2 + \left(\frac{dy/dt}{\omega} \right)^2 \right]^{\frac{1}{2}} \tag{3.52}$$

In addition, the energy correlation between the energy of the parent droplet and the one of the child droplet is used to determine the size of the child droplets. The energy of the parent droplet was given by O'Rourke and Amsden (1987) as

$$E_{parent} = 4\pi r^2 \sigma + K \frac{\pi}{5} \rho_p r^5 \left[\left(\frac{dy}{dt} \right)^2 + \omega^2 y^2 \right] \tag{3.53}$$

where *K* is the ratio of the total energy in both distortion and oscillation to the energy in the fundamental mode, with the order of 10/3. The energy of the child droplet is

$$E_{child} = 4\pi r^2 \sigma \frac{r}{r_{32}} + \frac{\pi}{6} \rho_p r^5 \left(\frac{dy}{dt} \right)^2 \tag{3.54}$$

in which r_{32} is the Sauter mean radius of the droplet distribution. Equating the energy of the parent and child droplets and setting y = 1 and $\omega = \sqrt{8\sigma / \rho_p r^3}$, one may obtain the size of the child droplet

$$r_{32} = \frac{r}{1 + \dfrac{8Ky^2}{20} + \dfrac{\rho_p r^3 (dy/dt)^2}{\sigma}\left(\dfrac{6K-5}{120}\right)} \tag{3.55}$$

According to mass conservation, the number of child droplets can be calculated by

$$N = N^0 \left(\frac{r^0}{r}\right)^3 \tag{3.56}$$

where r^0 and N^0 are the radius and the number of droplets at the previous time step, respectively.

In terms of the velocity of child droplets, it is assumed that a velocity component normal to the parent droplet velocity is imposed on the child droplets. Thus, the velocity of child droplets is give by

$$v_{child} = C_v C_b r \frac{dy}{dt} \tag{3.57}$$

where C_v is a constant of order 1.

Turbulent Dispersion of Droplets

The stochastic tracking model (random walk) is also employed to predict the dispersion of droplets owing to turbulence in the carrier fluid. In this approach, the effect of instantaneous turbulence velocity fluctuations on the droplet trajectories is taken into consideration through integrating the trajectory equations for individual droplets along the droplet particle path. The droplet is assumed to interact with the carrier phase over the smaller of the eddy lifetime and the eddy crossing time, which are defined respectively as

$$\tau_e = -T_L \log(\chi) \tag{3.58}$$

$$\tau_{cross} = -\tau \ln\left(1 - \frac{L_e}{\tau |u_r|}\right) \tag{3.59}$$

where χ is a uniform random number between 0 and 1 and T_L is the integral time, which make use of the equivalent LES time scales for LES model in FLUENT; τ is the droplet relaxation time and L_e is the eddy length scale, $|u_r|$ is the magnitude of the relative velocity.

In terms of numerical methods employed for both gas phase and liquid phase, the details regarding temporal discretization, spatial discretization and pressure-velocity coupling etc. are provided in Appendix A.

3.3 Results and Discussion

3.3.1 Computation Domain and Flow conditions

Simulations of a coaxial jet are preformed based on the experiments of Sommerfield and Qiu (1998) to validate the capability of LES in conjunction with evaporation model. Fig. 3.1 shows the computational domain, which primarily contains the chamber with a diameter of 200 mm and a length of 1500 mm and the annulus with the inner diameter of 40 mm, the outer diameter of 64 mm and the length of 100 mm. The grid adopted for flow simulations consists of about 3.2 million cells shown in Figs. 3.2-3.3, validated to be grid-independent. The main parameters for different cases are summarized in Table 3.1. In terms of the cold case, the heated air with the temperature of 373 K and the air mass flow rate of 29.0 g/s is introduced into the chamber through the annulus and the maximum air velocity is 18 m/s. For the hot case, droplets of isopropyl alcohol with the initial uniform temperature of 311 K are injected through the central wall region according to the measured size-velocity correlations and the total droplet mass flow rate in this case is 0.44 g/s. It should be pointed out that the droplet velocity-size correlations adopted may mimic a conical spray with a spray angle of around 60 degree. The Reynolds number at inlet annulus is about 2.116×10^4.

To model the cases of interest numerically, the mass flow rate is specified at the inlet and a sufficiently long introduction section is defined to arrive at the fully developed flow into the chamber. In addition, the pressure outlet boundary conditions are specified at the outlet. It should be noted that the wall temperature profiles given by experiments (Sommerfeld and Qiu, 1998) are used, as shown in Fig. 3.4. The temperature-dependent relations regarding thermal properties of two phases involving heat capacity, viscosity and evaporation pressure etc. are employed, as given in Appendix B.

Table 3.1 Flow Condition for the Single- and Two-Phase Flows

Case	Air Vol. Flow Rate (m^3/s)	Air Mass Flow Rate (g/s)	Max. Air Velocity (m/s)	Air Temp. (^0C)	Flow Reynolds Number	Liquid mass Flow Rate (g/s)	Liquid Temp. at Nozzle Exit (^0C)
Cold Case	0.032	29.0	18.0	100.0	8,577.0	-	-
Hot Case	0.031	28.3	18.0	100.0	8,309.0	0.44	34.0

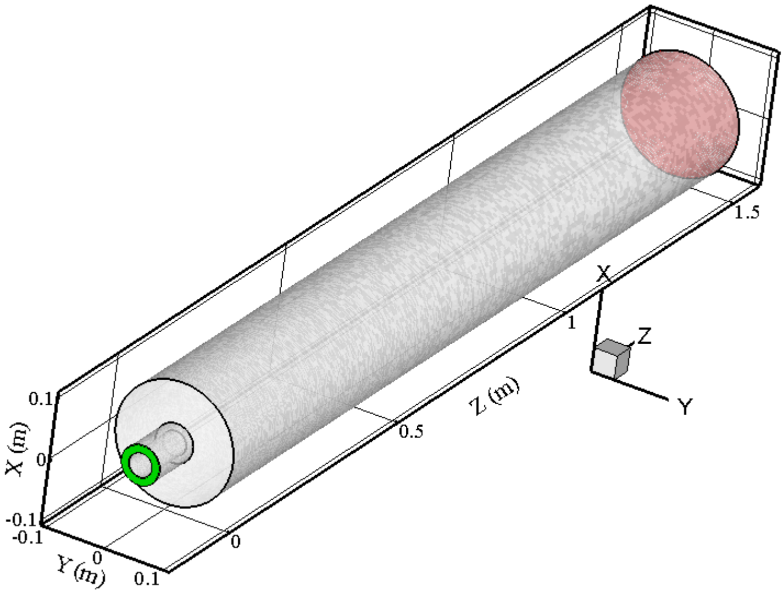

Fig. 3.1 Geometrical View of Computation Domain

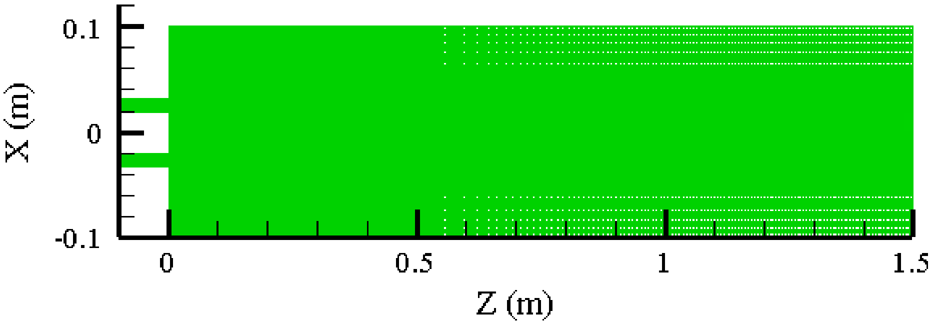

Fig. 3.2 Axial-Coordinate Mesh

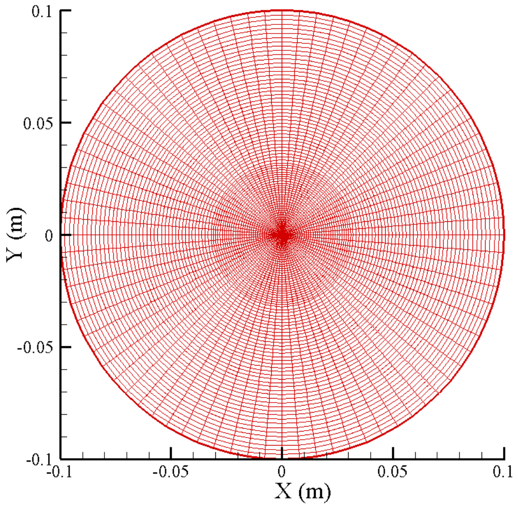

Fig. 3.3 Radial-Coordinate Mesh

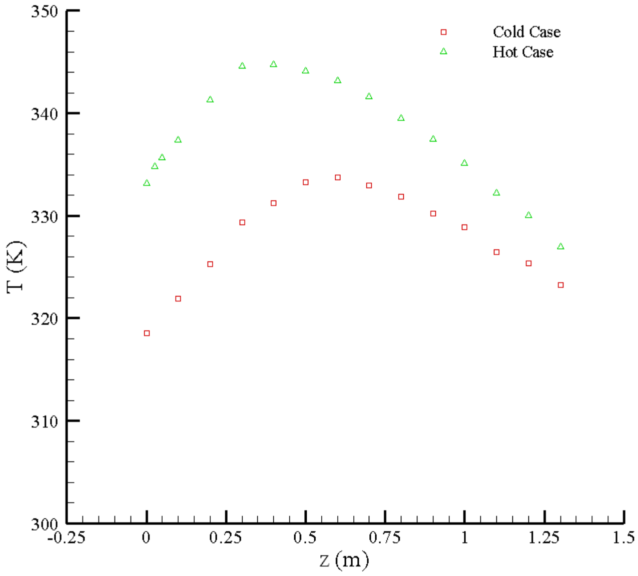

Fig. 3.4 Wall Temperature Profiles along the Axial Direction

3.3.2 Numerical Predictions for the Cold Flow

In terms of the cold flow case, comparisons between the current numerical predictions and experimental data measured by Sommerfeld et al. (1998) are presented in Figs. 3.5-3.6. It can be seen in Figs. 3.5-3.6 that good agreements between calculations and experimental data regarding both axial mean velocity and axial rms velocity are achieved. Additionally, two recirculation zones built up in the flow field are captured, as reported in experimental studies (Sommerfeld and Qiu, 1998). However, it should be noted that, in the central recirculation zone, the rms axial velocity is slightly under-predicted probably because of the SGS models used and/or measurement errors. Furthermore, the instantaneous contour of axial velocity in the symmetry plane, Y = 0, and the contours of mean axial velocity at different cross sections are shown in Figs. 3.7 and 3.8, respectively, in which the recirculation regions are clearly visible. These results may reveal that the present simulation can capture the flow characteristics for the cold case and can be extended to the evaporation case.

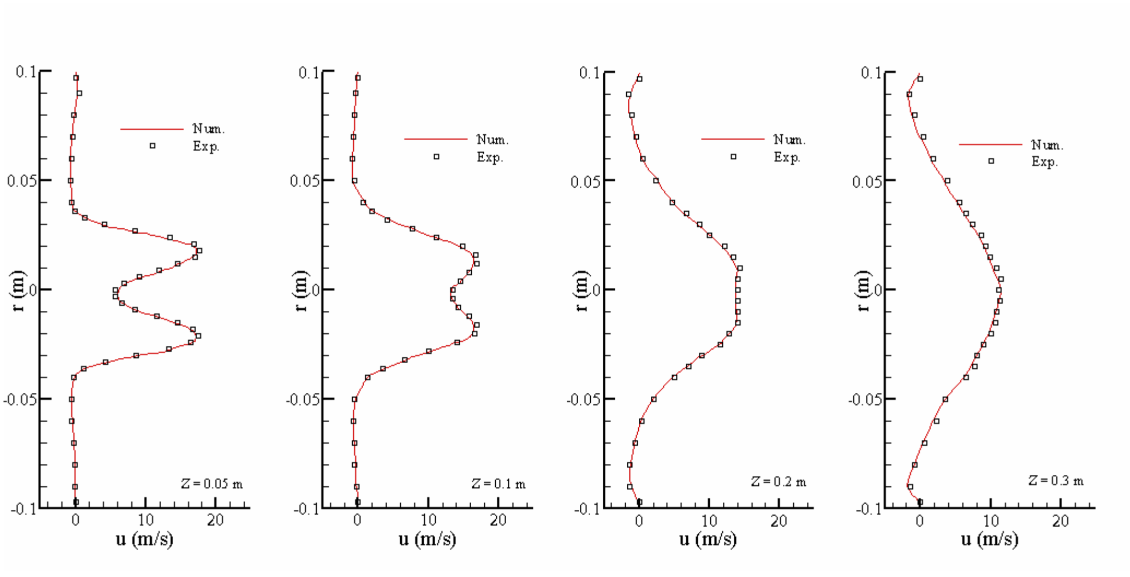

Fig. 3.5 Comparison of Numerical Predictions and Experimental Measurements on Mean Axial Velocities

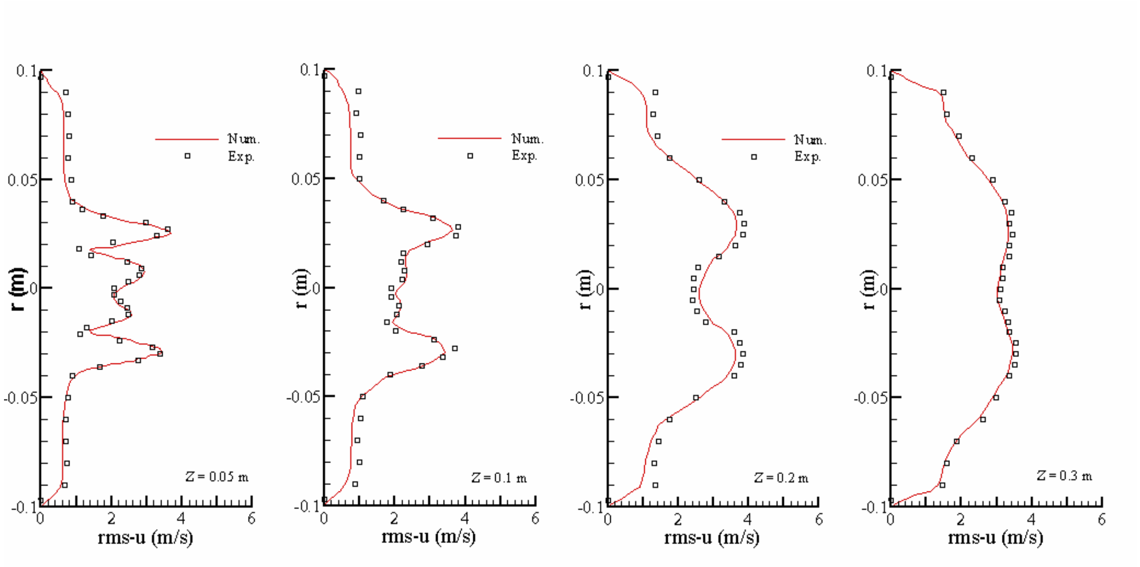

Fig. 3.6 Comparison of Numerical Predictions and Experimental Measurements on rms Axial Velocities

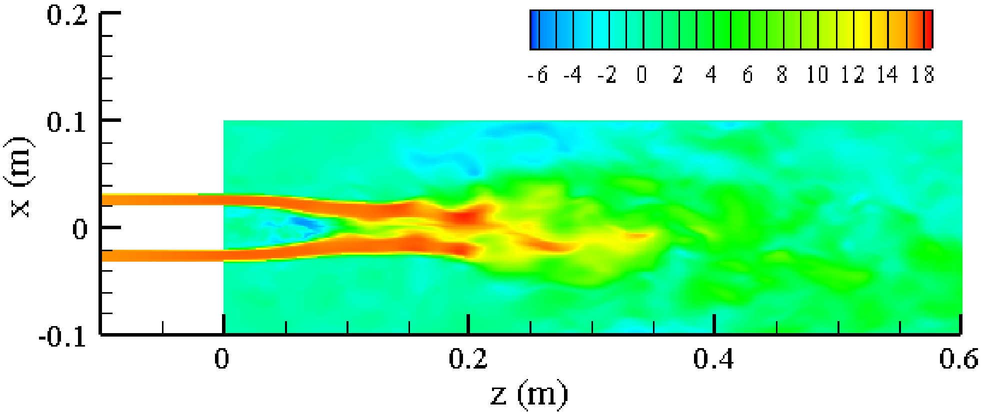

Fig. 3.7 Instantaneous Axial Velocity for Cold Case

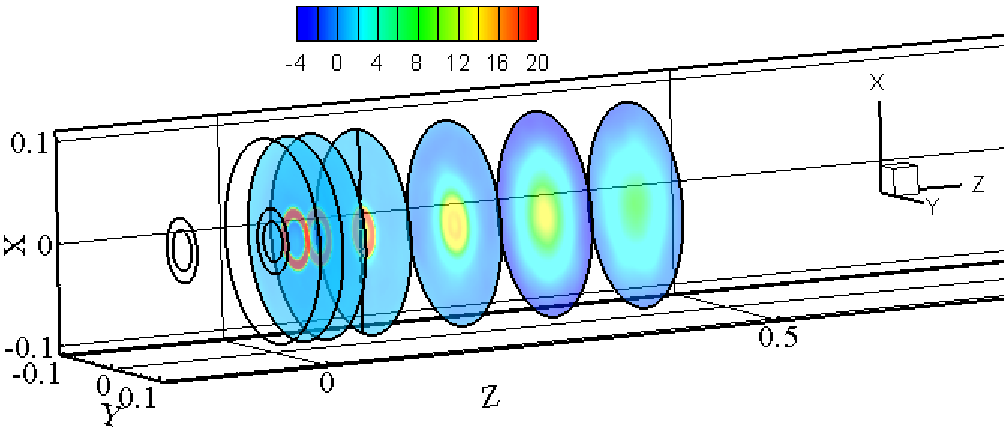

Fig. 3.8 Mean Axial Velocity at Different Cross Sections
(z = 0.025, 0.05, 0.1, 0.2, 0.3 and 0.4 m)

3.3.3 Numerical Predictions for the Hot Case

In terms of the hot case, comparisons between the current numerical predictions and experimental data measured by Sommerfeld et al. (1998) are presented in Figs. 3.9 - 3.11. It is seen in Figs. 3.9-3.11 that good agreements between calculations and experimental data in terms of mean axial velocity, rms axial velocity and droplet diameter obtained by averaging over the entire droplet size spectrum at each location are achieved. The profile of mean axial velocity at Z = 0.05m indicates two peaks associated to the hollow-cone spray. In particular, the recirculation regions developed downstream of the nozzle holder is properly captured, whereas, the axial velocity in the central recirculation is slightly under-predicted. Furthermore, the droplet diameter shown in Fig. 3.11 can display a characteristic profile related to a hollow-cone atomizer, in which the larger droplets appear near the edge of the spray and the smaller droplets exist in the core region. Moreover, the instantaneous axial velocity is presented in Fig. 3.12. In addition, the contours on temperature and mass fraction of isopropyl alcohol in the symmetry plane, Y = 0, and the mass fraction of liquid phase at different locations are shown in Fig. 3.13, Fig. 3.14 and Fig. 3.15, respectively.

It is seen that the current code could capture both the flow behaviour and droplets' characteristics and, therefore, can be extended to cases of combustion instabilities in which evaporation of droplets is a rate-controlling factor in the further research.

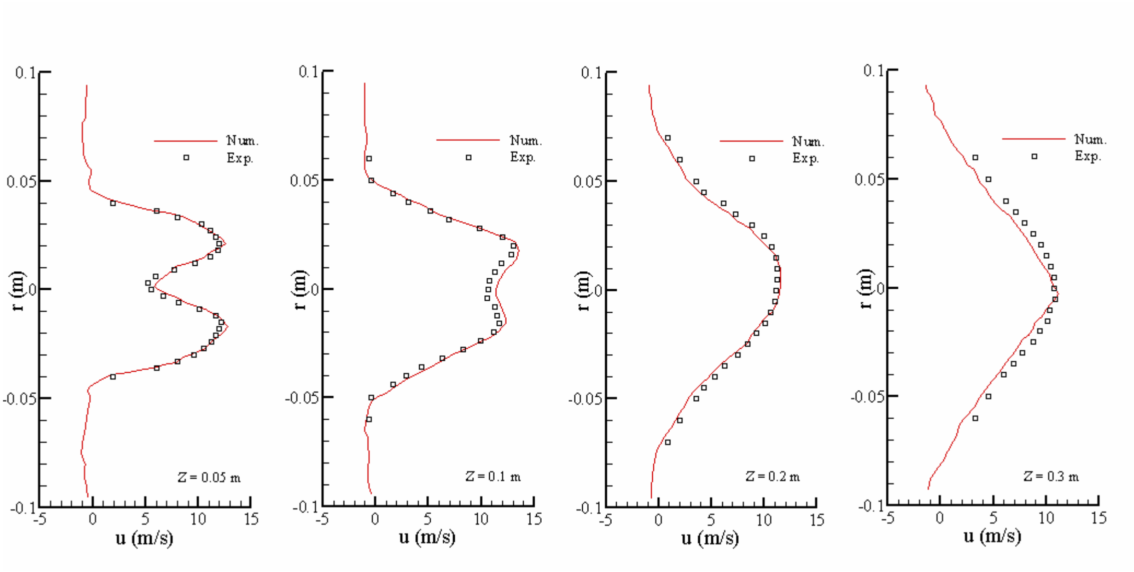

Fig. 3.9 Comparison of Numerical Predictions and Experimental Measurements on Mean Axial Velocities

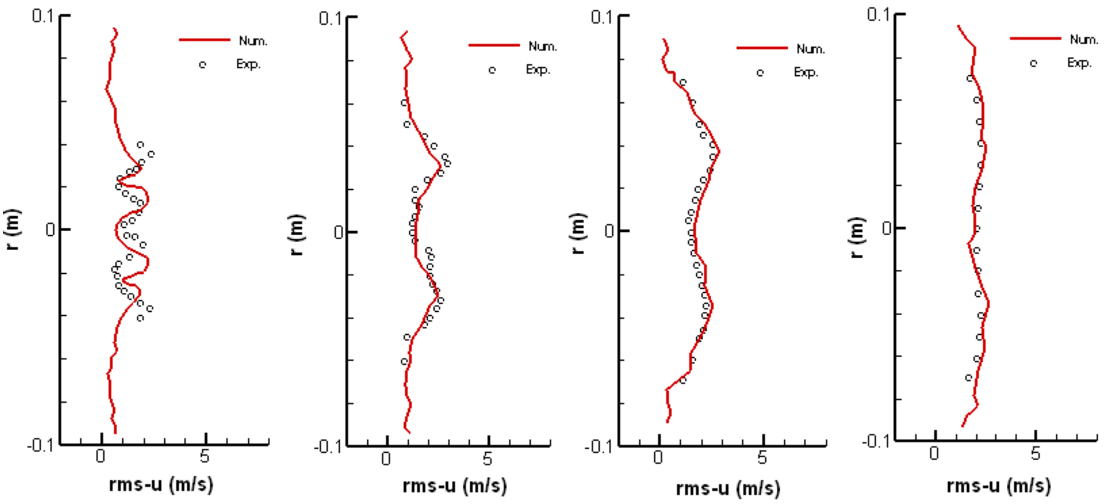

Fig. 3.10 Comparison of Numerical Predictions and Experimental Measurements on Mean rms Axial Velocities

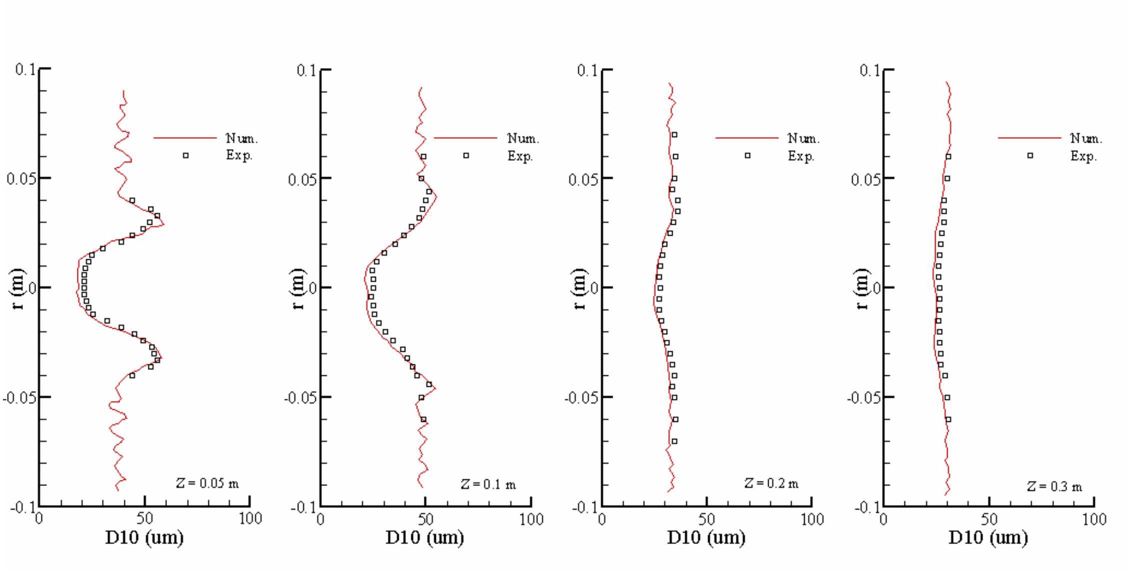

Fig. 3.11 Comparison of Numerical Predictions and Experimental Measurements on Droplet Diameter

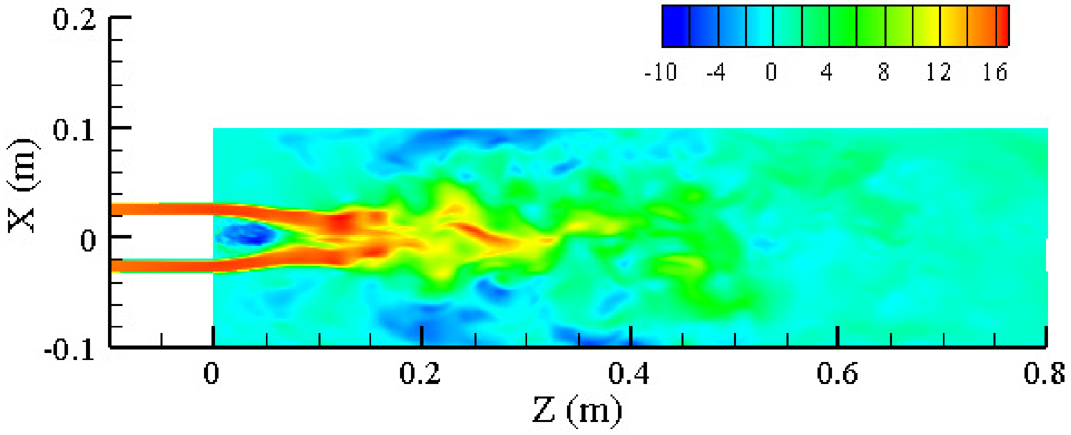

Fig. 3.12 Instantaneous Axial Velocity for Hot Case

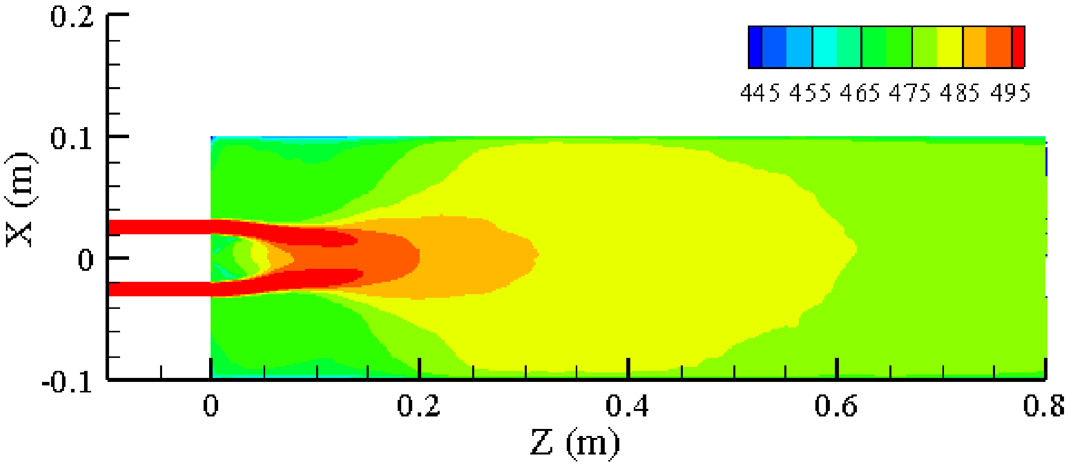

Fig. 3.13 Contour of Temperature

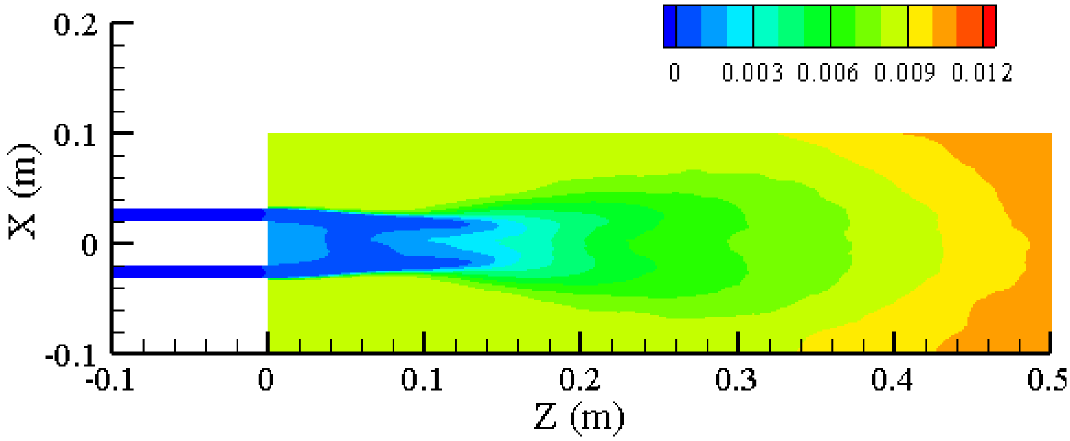

Fig. 3.14 Contour of Mass Fraction of Isopropyl Alcohol

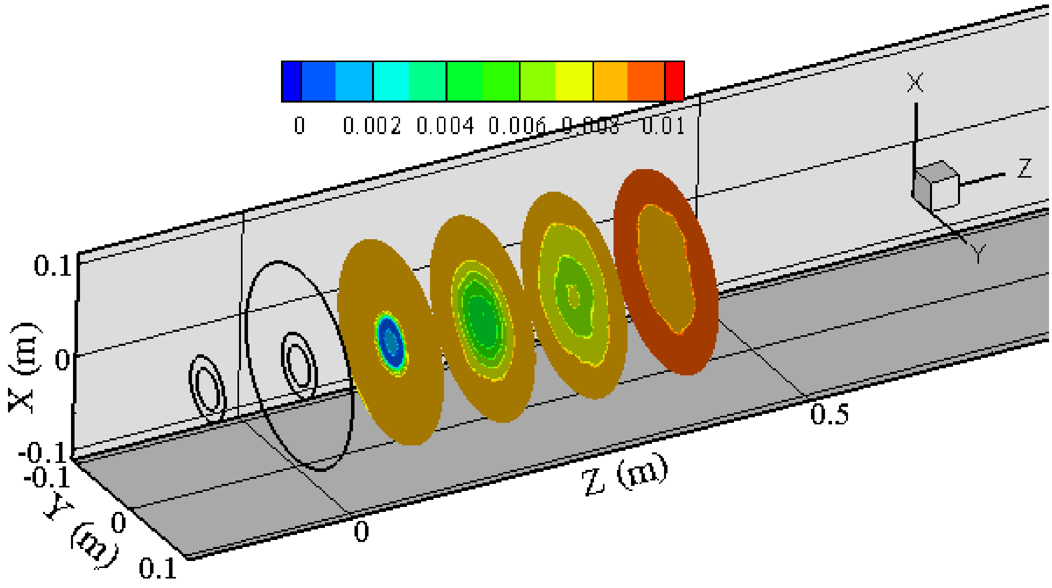

Fig. 3.15 Mass Fraction of Isopropyl Alcohol at Different Locations

CHAPTER 4

TRANSIENT ANALYSIS OF SUB-CRITICAL EVAPORATION OF FUEL DROPLET

4.1 Introduction

In this section, a brief description of the numerical vaporization model is presented to provide the context for the non-linear analysis that follows; furthermore, as emphasized emphatically by Sirignano and co-workers (1989; 1993; 1999), the simple steady state vaporization models routinely used in the literature in the context of gas turbine combustion and other less demanding applications are not appropriate for use in the study of thermo-acoustic instability for vaporizing sprays, when the ambient is unsteady. Thus, this section will highlight the important elements of the unsteady vaporization model, accounting at this point for the changing ambient conditions as forced by the acoustic field for a single stationary droplet. The numerical method of pressure-velocity-density coupling intended to capture the extremely important two-way coupling between the vaporization and acoustic fields for the quasi-stationary droplet is developed.

4.2 Formulation

4.2.1 Mathematical Model

A spherical droplet of pure liquid, initially at temperature T_0 and radius R_0, is suddenly subjected to a surrounding gas with high temperature and varying pressure as stated above. Classical Fick's law is used in the species transport equation while ignoring heat fluxes due to the inter-diffusion and Dufour effects and viscous dissipation. With these assumptions, the governing conservation equations are given as (Sirignano, 1999):

for the liquid phase, $r<R(t)$

energy equation

$$\frac{\partial\left(r^2 T_l\right)}{\partial t}=\frac{\partial}{\partial r}\left(\alpha_l r^2 \frac{\partial T_l}{\partial r}\right) \tag{4.1}$$

for the gaseous phase, $r>R(t)$

continuity equation

$$\frac{\partial\left(\rho_g r^2\right)}{\partial t}+\frac{\partial}{\partial r}\left(\rho_g r^2 v_r\right)=0 \tag{4.2}$$

momentum equation

$$\frac{\partial\left(\rho v_r r^2\right)}{\partial t}+\frac{\partial}{\partial r}\left(\rho r^2 v_r v_r\right)=\frac{\partial}{\partial r}\left(\frac{4}{3}\mu r^2 \frac{\partial v_r}{\partial r}\right)-\frac{8}{3}\mu v_r-\frac{4}{3}v_r r\frac{\partial \mu}{\partial r}-r^2\frac{\partial P}{\partial r} \tag{4.3}$$

species equation

$$\frac{\partial(\rho r^2 m_1)}{\partial t}+\frac{\partial}{\partial r}(\rho r^2 v_r m_1)=\frac{\partial}{\partial r}\left(\rho D_{12} r^2\frac{\partial m_1}{\partial r}\right) \tag{4.4}$$

energy equation

$$\begin{aligned}\frac{\partial(\rho r^2 T_g)}{\partial t}+\frac{\partial}{\partial r}(\rho r^2 v_r T_g)=\frac{1}{C_p}\frac{\partial}{\partial r}\left(kr^2\frac{\partial T_g}{\partial r}\right)+\frac{\rho r^2 D_{12}}{C_p}\frac{\partial T_g}{\partial r}\\ \cdot(C_{p1}-C_{p2})\frac{\partial m_1}{\partial r}+\frac{v_r r^2}{C_p}\frac{\partial P}{\partial r}\end{aligned} \tag{4.5}$$

where the subscript 1 denotes the fuel species and 2 represents air; subscript l indicates the liquid phase and subscript g denotes the gaseous phase.

Considering the case of interest with moving boundaries, non-dimensionalization was employed in this study so that the receding gas-liquid interface is stationary in the same manner used by Elperin and Krasovitov (2006). The following variables were defined as

$$x=\frac{r}{R(t)};\ \tau=\frac{\alpha_l t}{R_0^2};\ \theta_g=\frac{T_g}{T_{g,\infty}};\ \theta_l=\frac{T_l}{T_{g,\infty}};\ \xi(\tau)=\frac{R(t)}{R_0}$$

where α_l is thermal diffusivity of liquid, $T_{g,\infty}$ is the temperature at infinity and R_0 is the initial diameter of droplet.

Thus, the dimensionless governing equations can be rewritten as

For the liquid phase, $r < R(t)$

$$\frac{\partial(\xi^2\theta_l)}{\partial\tau}+\frac{\xi}{x^2}\frac{\partial(x^2 V_l\theta_l)}{\partial x}=\frac{1}{x^2}\frac{\partial}{\partial x}\left(x^2\frac{\partial\theta_l}{\partial x}\right)-\frac{1}{2}\frac{d\xi^2}{d\tau}\theta_l \tag{4.6}$$

where $V_l = -\frac{\alpha_l x}{R_0}\dot{\xi}(\tau)$.

For the gaseous phase, $r > R(t)$

continuity equation

$$\frac{\partial\left(\alpha_l \rho \xi^2\right)}{\partial \tau} + \frac{R_0 \xi}{x^2}\frac{\partial\left(\rho x^2 V_g\right)}{\partial x} = -\frac{1}{2}\frac{d\xi^2}{d\tau}\alpha_l \rho \tag{4.7}$$

where $V_g = v_r - \frac{\alpha_l x}{R_0}\dot{\xi}(\tau)$.

momentum equation

$$\begin{aligned}\frac{\partial\left(\alpha_l \rho \xi^2 v_r\right)}{\partial \tau} + \frac{R_0 \xi}{x^2}\frac{\partial\left(\rho x^2 V_g v_r\right)}{\partial x} &= \frac{1}{x^2}\frac{\partial}{\partial x}\left(\frac{4}{3}\mu x^2 \frac{\partial v_r}{\partial x}\right) - \frac{8}{3}\frac{\mu}{x^2}v_r \\ &\quad -\frac{4}{3}\frac{v_r}{x}\frac{\partial \mu}{\partial x} - R_0 \xi \frac{\partial p}{\partial r} - \frac{1}{2}\frac{d\xi^2}{d\tau}\alpha_l v_r\end{aligned} \tag{4.8}$$

species equation

$$\frac{\partial\left(\alpha_l \rho \xi^2 m_1\right)}{\partial \tau} + \frac{R_0 \xi}{x^2}\frac{\partial\left(\rho x^2 V_g m_1\right)}{\partial x} = \frac{1}{x^2}\frac{\partial}{\partial x}\left(\rho D_{12} x^2 \frac{\partial m_1}{\partial x}\right) - \frac{1}{2}\frac{d\xi^2}{d\tau}\alpha_l m_1 \tag{4.9}$$

energy equation

$$\begin{aligned}\frac{\partial\left(\alpha_l \rho \xi^2 C_p \theta_g\right)}{\partial \tau} + \frac{R_0 \xi}{x^2}\frac{\partial\left(\rho x^2 V_g C_p \theta_g\right)}{\partial x} &= \frac{1}{x^2}\frac{\partial}{\partial x}\left(k x^2 \frac{\partial \theta_g}{\partial x}\right) \\ &\quad + \frac{R_0 \xi}{T_{g,\infty}}\frac{\partial p}{\partial r} - \frac{1}{2}\frac{d\xi^2}{d\tau}\alpha_l \theta_g\end{aligned} \tag{4.10}$$

4.2.2 Boundary Conditions

The boundary conditions are:

At the droplet center:

$$\left.\frac{\partial \theta_l}{\partial x}\right|_{x=0} = 0 \tag{4.11}$$

As $x \rightarrow \infty$:

$$\left. m_1 \right|_{x\rightarrow\infty} = 0;\ \left. \theta_g \right|_{x\rightarrow\infty} = 1;\ \left. v_r \right|_{x\rightarrow\infty} = 0;\ \left. \rho \right|_{x\rightarrow\infty} = \rho_\infty;\ \left. p \right|_{x\rightarrow\infty} = p_\infty \tag{4.12}$$

At the droplet surface, $x = 1$:

temperature continuity

$$\left. \theta_g \right|_{x=1^+} = \left. \theta_l \right|_{x=1^-}$$

energy conservation

$$\left.\frac{k}{k_l}\frac{1}{\xi}\frac{\partial \theta_g}{\partial x}\right|_{x=1} = \left.\frac{1}{\xi}\frac{\partial \theta_l}{\partial x}\right|_{x=1} - \left.\frac{\hat{h}_{fg}}{C_{p,l}T_{g,\infty}}\right|_{x=1} \tag{4.13}$$

species conservation

$$\left. -\frac{1}{v_r}\frac{D_{12}}{\xi R_0}\left(1-\frac{\rho}{\rho_l}\right)\frac{\partial m_1}{\partial x}\right|_{x=1} = \left(1-m_1\right)_{x=1} \tag{4.14}$$

In addition, the mass flux is balanced at the gas-liquid interface, viz.,

$$\dot{m}'' = \rho_g\left(v_{r,s} - \frac{dR}{dt}\right) = -\rho_l\frac{dR}{dt}$$

which yields,

$$v_r\big|_{x=1} = \frac{\alpha_l}{R_0}\dot{\xi}(\tau)\left(1 - \frac{\rho_l}{\rho_g}\bigg|_{x=1}\right) \tag{4.15}$$

and

$$\dot{\xi}(\tau) = \left(\frac{\rho_g}{\rho_l \xi}\frac{D_{12}}{\alpha_l(1-m_1)}\right)_{x=1} \tag{4.16}$$

The mass fraction of vapour here depends on the saturation pressure and temperature, that is,

$$m_1\big|_{x=1} = m_1(P_{sat}, T_{sat})\big|_{x=1} \tag{4.17}$$

4.2.3 Velocity-Pressure-Density Coupling

In the past, the pressure field was generally calculated using the equation of state (Hubbard et al., 1975; Tong and Sirignano, 1989; Duvvur et al., 1996; Elperin and Krasovitov, 2006), which decouples the interaction of pressure with velocity. To capture the nature of evaporation relevant to the problem of interest, a numerical method for the pressure-velocity-density coupling is proposed in this work. The discretized continuity Equation (4.7) is given as

$$\frac{\rho^{m-1} - \rho^n}{\Delta\tau}\cdot\Delta V + F_e^* + F_w^* = Q_0 + Q_m^* \tag{4.18}$$

where * denotes that the mass conservation is not satisfied; F_e^* and F_w^* are the mass flux at the cell face e and w, respectively; Q_0 indicates the source term without accounting for pressure correction and Q_m^* denotes the imbalance which must be eliminated by a correction method; superscript m indicates the outer iteration for solving pressure-velocity-density coupling.

For compressible flows, the mass flux depends on the velocity component normal to the cell face and the density. Thus, the mass flux correction is

$$F' = F'_v + F'_\rho \tag{4.19}$$

where the first term on the right hand side denotes the velocity correction and the second represents the density correction. In addition, the second-order term is neglected since it becomes zero more rapidly than the two terms under consideration. It is noted that these terms become zero when convergence is achieved.

The SIMPLE method (Ferziger and Perić, 2002) was used to approximate the mass flux correction associated with the velocity correction, given as

$$F'_v = F'_v\left(\xi, \dot{\xi}, \rho, S, v, \frac{\partial p}{\partial x}\right) \tag{4.20}$$

where S is the cell surface area.

The second term in Equation (4.19) results from compressibility. Assuming the temperature is fixed for the outer iteration, one obtains

$$\rho' \approx \left(\frac{\partial \rho}{\partial p}\right)_T p' = C_\rho p' \tag{4.21}$$

where the coefficient C_ρ can be determined using the equation of state as,

$$C_\rho = \left(\frac{\partial \rho}{\partial p}\right)_T = \frac{1}{R_u T} \cdot \frac{1}{\sum_{i=1}^{K} \frac{m_i}{M_i}} \tag{4.22}$$

in which, in terms of the case of interest, K is 2.

Therefore, the second term in the mass flux correction can be obtained as,

$$F'_\rho = F'_\rho\left(\xi, \dot{\xi}, C_\rho, \rho, v, S\right) \tag{4.23}$$

Substitution of Equations (4.20) and (4.23) into Equation (4.18) yields

$$\frac{\rho'_P \Delta V}{\Delta \tau} + F'_e + F'_w + Q^*_m = 0 \tag{4.24}$$

If ρ'_P is expressed using p'_P in the above equation, one can obtain an algebraic system of equations for the pressure correction

$$A_P p'_P + A_e p'_e + A_w p'_w = -Q^*_m \tag{4.25}$$

where A_P, A_e and A_w are coefficients at cell centre, cell surface e and w, respectively and which yields the pressure correction that can be used for the outer iteration.

4.2.4 Numerical Methods

In this work, the finite volume method was used to solve Equations (4.6-4.10) numerically. The central differencing scheme with second-order accuracy was employed for the convective terms, whereas Crank-Nicolson scheme is used for the unsteady terms with second-order accuracy (Hubbard et al., 1975; Patankar, 1980). It is noted that the energy and species equations were solved initially and with the known temperature and mass fraction distributions, the mass equation was then dealt with. The above iterative procedure was continued until $\left|1 - \dot{m}''^0 / \dot{m}''\right| \le 10^{-5}$. Finally, the momentum equation was solved with the pressure correction obtained. In this work, the initial conditions were given by constructing self-consistent reasonable polynomial distributions for the field variables. The initial surface temperature of droplet was 285 K and the ambient temperature was 600 K. The initial diameter of the droplet was 250 μm and the end of the computation domain was specified to be at 300 instantaneous droplet radii. Additionally, a geometric mesh with points clustered near the droplet surface was used, and the mesh inside the droplet had 124 points with common ratio of 1.01, while 776 points with common ratio of 1.012 were distributed along the gaseous phase. Different meshes regarding both phases were tested and the current mesh may satisfy that the predicted droplet lifetime with finer mesh changed by less than 3%. The calculations were terminated when $R/R_0<0.1$.

4.2.5 Thermo-physical Properties

The properties of the liquid phase, *n*-Octane, were taken as constant, with ρ_l taken as 703.6 kg/m^3, C_{pl} = 2420 J/(kg·K) and k_l = 0.116 W/(m·K). For the gas phase, molecular weights of n-Octane and air were 114.13 and 29.87, respectively. The heat of vaporization was calculated by

$$\hat{h}_{fg} = 2.977\times10^5 - 2.6913\times10^3\zeta - 5.5287\times10^3\zeta^2 - 858.3\zeta^3,\ \text{J/kg}$$

where $\zeta = \ln P_{sat}$. The thermophysical properties for the pure species were obtained from polynomials given by Turns (2000). The method of Wilke was used for viscosity and the thermal conductivity was obtained by the Wassiljewa equation (Poling et al., 2001). The diffusion coefficient for the binary system was calculated from the Chapman-Enskog kinetic theory (Poling et al., 2001).

4.3 Results and Discussion

Different test cases were investigated for liquid phase and/or gaseous phase. Numerical results for a stationary *n*-Octane droplet evaporating in hot air environment are presented in Figs. 4.1-4.5. Fig. 4.1 shows the transient responses of droplet radius and surface temperature compared to the analytical solutions obtained by hydrodynamic model and kinetic model discussed by Sazhin et al. (2004) and Sazhin (2006). It was found that the predicted results are in reasonable agreement with analytical solutions and their tendencies are very similar. Nevertheless, the differences on the surface temperature of droplet are relatively apparent and the resulting deviation is mostly caused by the quasi-steady assumptions and limitations associated with the analytical models. Generally, for analytical methods, the temperature gradient inside the droplet is neglected and the gaseous temperature distribution is not taken into consideration (Lefebvre, 1989; Sazhin, 2006). Furthermore, the intrinsic moving boundary of droplet captured by the current model can result in the artificial diffusion within analytical solutions, and the resulting evaporation time is correspondingly reduced, as shown in Fig. 4.1. It should be pointed out that the pressure field obtained by the method of pressure-velocity-density coupling can play an important role in the transient behaviour of droplet vaporization. Moreover, Fig. 4.1 also exhibits that the kinetic model can predict longer evaporation time in comparison with the hydrodynamic model as reported by Sazhin et al. (2004). Figs. 4.2-4.5 show the temperature, mass fraction, velocity distributions and temperature distribution of droplet at different normalized times, respectively. The resulting tendencies of these variables are in reasonable agreement with the results reported by Hubbard et al.(1975).

In addition, it is noted that the model extensively employed in CFD simulations, denoted by dotted line in Fig. 4.1, is relatively inaccurate and not suitable for the study of thermo-acoustic/combustion instability in liquid-fuelled gas turbine combustors, although the advanced models detailedly reviewed and discussed by Sazhin (2006) are appreciated for most practical applications, and this study tends to extend the case of droplet vaporization accounting for both the convective heat transfer and the two-way coupling between vaporization and resulting acoustics in order to highlight the influence of the practical droplet vaporization process in an unstable combustion environment in the further work. Furthermore, the interaction between the mass addition and pressure oscillations will be investigated further in detail, to provide a basis for an improved understanding of the characteristic nonlinear behaviour regarding droplet evaporation, as qualitatively discussed in the following section.

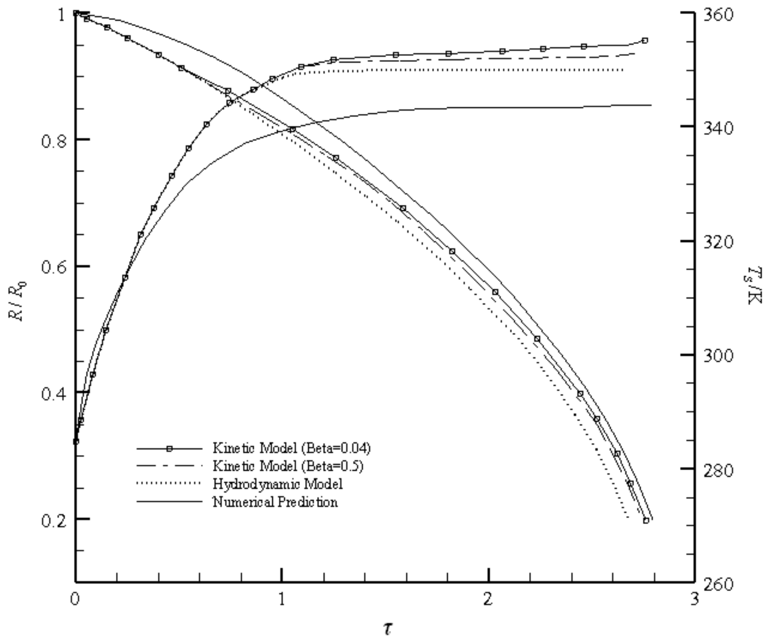

Fig. 4.1 Transient Response of Normalized Droplet Radius and Surface Temperature

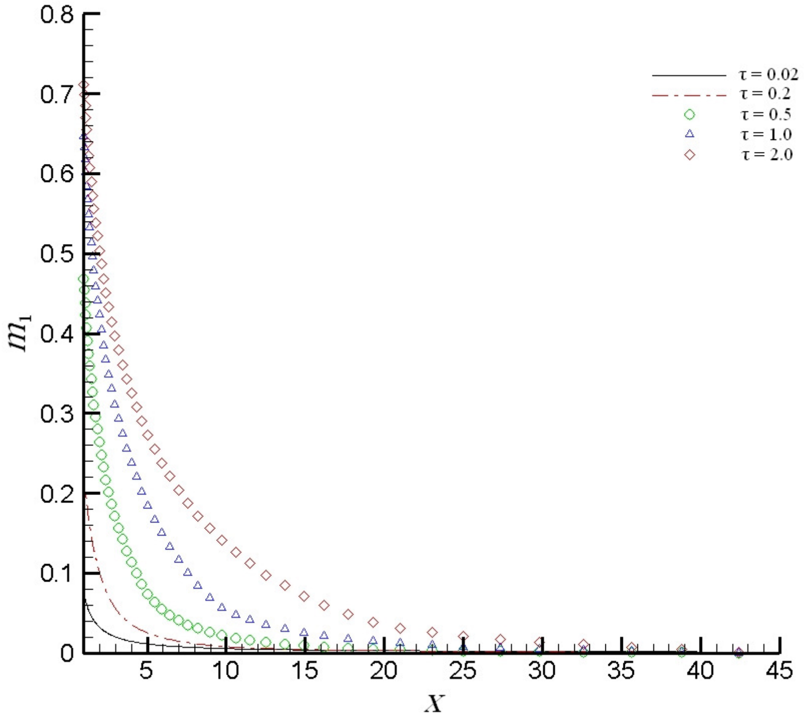

Fig. 4.2 Transient Mass Fraction Distribution at Different Normalized Time

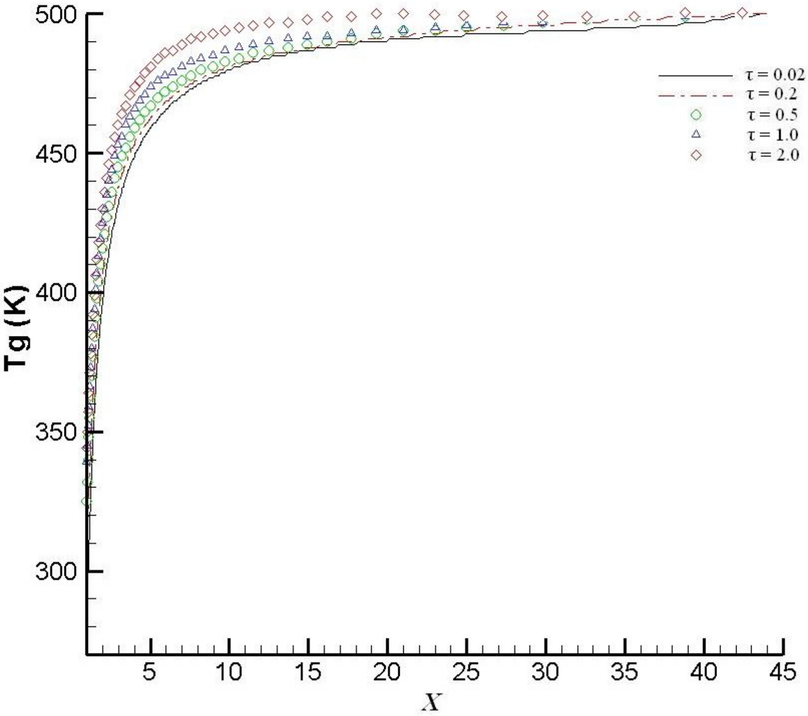

Fig. 4.3 Transient Temperature Distribution at Different Normalized Time

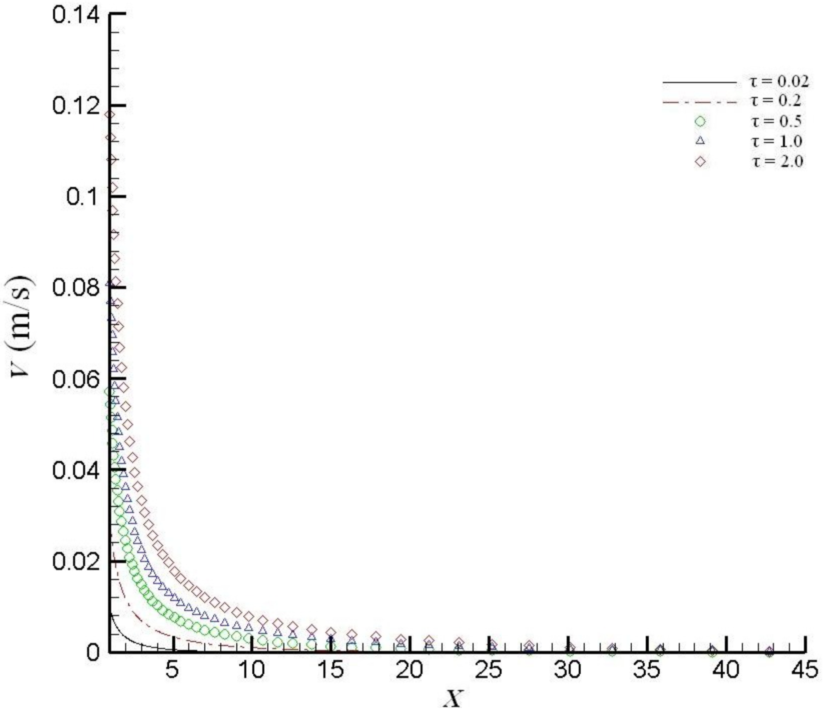

Fig. 4.4 Transient Velocity Distribution at Different Normalized Time

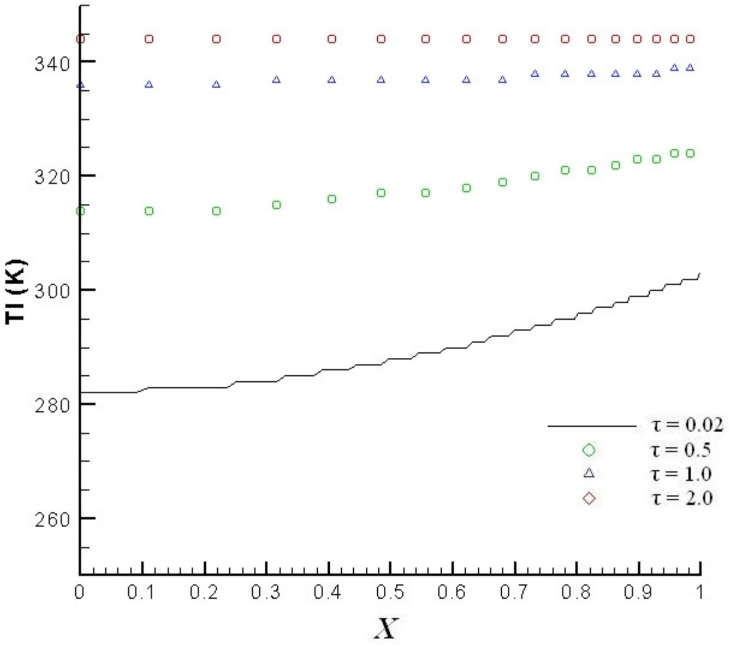

Fig. 4.5 Transient Temperature Distribution of Liquid Phase at Different Normalized Time

CHAPTER 5

NONLINEAR/CHAOTIC BEHAVIOUR IN THERMO-ACOUSTIC INSTABILITY

5.1 Introduction

As discussed above, it is of paramount importance to pay attention to system nonlinearities in thermo-acoustic/combustion instability. In this chapter, nonlinear analyses covering both the one-mode dynamic model considering a harmonic behaviour for the combustion process and the two-mode model initially put forward by Yang et al. (1987, 1988) are carried out. In terms of the former model, the Poincaré map is adopted to study the stability of the simple system and the corresponding bifurcation behaviour is computed. For the latter dynamic model, the bifurcation parameter and the corresponding period at Hopf points are calculated in detail using both numerical and analytical methods. These are of particular significance regarding the delineation of comprehensive mechanisms for thermo-acoustic instability as, the bifurcation behaviour and the multiplicity of solutions for a given nonlinear system are seldom considered in the currently employed experimental and numerical studies (CFD) carried out for thermo-acoustic instability. It makes sense to study the nonlinear behaviour inherent in thermo-acoustic instability using tools that can explore the variation of certain parameters covering the entire operational conditions. Such considerations, also pointed out by Culick (2006), enforce the notion that each numerical (CFD) simulation is, in general, only one particular case and it is, to some extent, difficult to generalize limited results to gain a fundamental understanding of thermo-acoustic instability in totality.

5.2 Modelling of Thermo-acoustic Instability

A methodology for the study of thermo-acoustic instabilities has been developed by Culick (1976a, 1976b) using the Galerkin method. The method employs a spectral representation of the unsteady velocity and pressure components in terms of the normal acoustic modes of the system. The sequential dynamic model associated with third-order nonlinearities was derived by Yang (1987, 1988). It is not necessary to reproduce the details, however a brief framework will be provided as baseline reference. The conservation equations in terms of a two-phase mixture are given as,

$$\frac{\partial \rho}{\partial t} + \nabla \cdot (\rho \mathbf{u}) = \mathbf{W} \tag{5.1}$$

$$\rho \frac{\partial \mathbf{u}}{\partial t} + \rho \mathbf{u} \cdot \nabla \mathbf{u} = -\nabla p + \mathbf{F} \tag{5.2}$$

$$\frac{\partial p}{\partial t} + \gamma p \nabla \cdot \mathbf{u} + \mathbf{u} \cdot \nabla p = \mathbf{P} \tag{5.3}$$

where ρ, p and the vector $\mathbf{u}$ are the density, pressure and velocity, respectively. **W** represents the mass conversion rate of condensed phases to gas per unit volume, **F** is the force of interaction of the gas with condensed phases, and **P** is the sum of the heat release associated with chemical reaction and the energy transfer between two phases. Here, the thermo-acoustic instability is mainly concerned with the representation and coupling of **P** which is expressed as,

$$\mathbf{P} = (\gamma - 1)q \tag{5.4}$$

in which q is the rate of heat addition and γ is the ratio of specific heats.

Subsequently, the flow variables are decomposed into mean and time-varying parts, given by,

$$\begin{aligned} \rho &= \bar{\rho} + \rho'(t, \mathbf{x}) \\ \mathbf{u} &= \bar{\mathbf{u}} + \mathbf{u}'(t, \mathbf{x}) \\ p &= \bar{p} + p'(t, \mathbf{x}) \\ q &= \bar{q} + q'(t, \mathbf{x}) \end{aligned} \tag{5.5}$$

Substitution of Equation (5.5) into (5.1)-(5.3) yields the nonlinear wave equation,

$$\frac{\partial^2 p'}{\partial t^2} - a^2 \nabla^2 p' = h \tag{5.6}$$

where a is the sound speed, and h denotes the source term of wave equation.

Taking the component $\nabla p'$ normal to the boundary, the corresponding boundary condition associated with Equation (5.6) is given as,

$$\mathbf{n} \cdot \nabla p' = -f \tag{5.7}$$

A solution for the time-varying pressure is expanded in terms of the orthogonal acoustics modes of the system, $\boldsymbol{\psi}_n$, defined as an eigenvalue problem,

$$\nabla^2 \boldsymbol{\psi}_n + k_n^2 \boldsymbol{\psi}_n = 0 \tag{5.8}$$

$$\mathbf{n} \cdot \nabla \boldsymbol{\psi}_n = 0 \tag{5.9}$$

where $k_n = \omega_n / a$ is the wavenumber for the *n*th mode with the frequency ω_n. the expansions of time-varying pressure and velocity are given as,

$$p'(\mathbf{x}, t) = \bar{p} \sum_n \eta_n(t) \boldsymbol{\psi}_n(\mathbf{x}) \tag{5.10a}$$

$$u' = \sum_n \frac{\dot{\eta}_n(t)}{\gamma k_n^2} \nabla \boldsymbol{\psi}_n(\mathbf{x}) \tag{5.10b}$$

These expressions are substituted into Equation (5.6) which is then multiplied by $\boldsymbol{\psi}_n(\mathbf{x})$, whereas Equation (5.8) is multiplied by p'. These two resulting equations are subtracted and integrated over the whole chamber volume. Using the orthogonal property of the acoustic modes, Green's theorem and their boundary conditions, the set of ordinary differential equations for the amplitude of each mode is then obtained as,

$$\ddot{\eta}_n + \omega_n^2 \eta_n = \mathbf{F}_n \tag{5.11}$$

where the forcing function $\mathbf{F}_n$ is

$$\mathbf{F}_n = -\frac{a^2}{\bar{p} E_n^2} \left[\iiint_{\Omega} \boldsymbol{\psi}_n(\mathbf{x}) h dV + \oiint_{\partial\Omega} \boldsymbol{\psi}_n(\mathbf{x}) f dS \right] \tag{5.12}$$

and

$$E_n^2 = \iiint_{\Omega} \boldsymbol{\psi}_n^2(\mathbf{x})dV$$

Yang et al. (1987) presented the simplified expression of $\mathbf{F}_n$ as,

$$\begin{aligned}\mathbf{F}_n = &-\sum_i \left[D_{ni}\dot{\eta}_i + E_{ni}\eta_i\right] \\ &-\sum_i\sum_j \left[A_{nij}\dot{\eta}_i\dot{\eta}_j + B_{nij}\eta_i\eta_j\right] \\ &-\sum_i\sum_j\sum \left[R_{nijm}\dot{\eta}_i\dot{\eta}_j\dot{\eta}_m + S_{nijm}\eta_i\eta_j\eta_m\right] \\ &+\mathbf{Q}\end{aligned} \tag{5.13}$$

where the coefficients associated with the acoustic wave motions are defined as,

$$A_{nij} = \frac{I_{nij}}{4\gamma k_i^2 k_j^2}\left[\left(k_i^2 + k_j^2\right)^2 - k_n^4 - 4\gamma k_i^2 k_j^2\right] \tag{5.14a}$$

$$B_{nij} = \frac{I_{nij}}{2\gamma}(\gamma - 1)a^2\left(k_i^2 + k_j^2\right) \tag{5.14b}$$

$$R_{nijm} = \frac{1}{2\gamma^2 k_i^2 k_j^2 E_n^2}\left[k_n^2 \iiint_{\Omega} \boldsymbol{\psi}_n \boldsymbol{\psi}_m \nabla\boldsymbol{\psi}_i \cdot \nabla\boldsymbol{\psi}_j dV - \iiint_{\Omega} (\nabla\boldsymbol{\psi}_n \cdot \nabla\boldsymbol{\psi}_m)(\nabla\boldsymbol{\psi}_i \cdot \nabla\boldsymbol{\psi}_j)dV\right] \tag{5.14c}$$

$$S_{nijm} = \frac{(\gamma - 1)a^2 k_n^2}{6\gamma^2 E_n^2}\iiint_{\Omega} \boldsymbol{\psi}_n \boldsymbol{\psi}_m \boldsymbol{\psi}_i \boldsymbol{\psi}_j dV \tag{5.14d}$$

$$I_{nij} = \frac{1}{E_n^2}\iiint_{\Omega} \boldsymbol{\psi}_n \boldsymbol{\psi}_i \boldsymbol{\psi}_j dV \tag{5.14e}$$

and the source term related to heat release is,

$$\mathbf{Q} = \frac{\gamma - 1}{\bar{p}E_n^2}\iiint_{\Omega} \psi_n \frac{\partial q'}{\partial t} dV \tag{5.14f}$$

It should be noted that D_{ni} and E_{nj} are related to linear processes of wave motions in a combustion chamber, whereas A_{nij}, B_{nij}, R_{nijm} and S_{nijm} are associated with the nonlinear processes governing the wave motion. The energy transfer between the acoustic modes is determined by these nonlinear terms in Equation (5.13), as argued by Ananthkrishnan et al. (2005). Nevertheless, phase heat transfer, such as evaporation and reactions, influence the nature of the term **Q**.

5.3 One-mode Dynamic Model

5.3.1 Formulation

The Poincaré map is an extremely useful tool for describing the dynamics of different types of nonlinear oscillatory system behaviour. In particular, arguments based on the Poincaré map establish the stability conditions for periodic orbits (Seydl, 1994). In this test case, the Poincaré map is used to study the stability of a simple dynamic system. In terms of Equations (5.11) and (5.13), the one mode is governed via the nonlinear ordinary equation which is simplified, using the orthogonal property of the acoustic modes as

$$\ddot{\eta}_n + \omega_n^2 \eta_n = -D_{nn}\dot{\eta}_i - E_{nn}\eta_i - R_{nnnn}\dot{\eta}_n^3 - S_{nnnn}\eta_n^3 + \mathbf{Q}$$

In terms of the combustion process and especially in the case of the Rijke tube, the mean rate of heat loss incorporating negligible fluctuations were assumed by McIntosh and Rylands (1996), whilst Heckl and Howe (2007) employed an appropriate Fourier series expansion for the process and pointed out a procedure whereby the above two approaches could be incorporated. However, in this study, to capture the inherent nonlinear characteristics pertaining to combustion instabilities and to provide a simplified albeit a generalized computational procedure, only a single domain Fourier series expansion corresponding to one specific mode of acoustics in the chamber is used in the same manner as that of Sterling (1993). The particular expression is given by the following:

$$\mathbf{Q} = \Gamma \cos(\omega_c t + \varphi)$$

where Γ, ω_c and φ represent the amplitude, frequency and phase angle of heat-release oscillation. Thus, the one-mode dynamic model is obtained as

$$\ddot{\eta}_n + \omega_n^2 \eta_n = -D_{nn}\dot{\eta}_i - E_{nn}\eta_i - R_{nnnn}\dot{\eta}_n^3 - S_{nnnn}\eta_n^3 + \Gamma\cos(\omega_c t + \phi) \qquad (5.15)$$

By introducing

$$\theta := \omega_c t + \phi,\ x_1 := \eta_n \text{ and } x_2 := \dot{\eta}_n$$

one can obtain a non-autonomous dynamic system written as,

$$\begin{aligned} \dot{x}_1 &= x_2 \\ \dot{x}_2 &= k_0 x_1 + k_1 x_2 + k_2 x_1^3 + k_3 x_2^3 + \Gamma\cos(\theta) \\ \dot{\theta} &= \omega_c \end{aligned} \qquad (5.16)$$

Here, the orthogonal property of harmonic functions is utilized and, as a result, the second-order nonlinear acoustics disappear. To simplify, consider the case of a tube with heat addition provided as previously discussed. Only the longitudinal modes are taken into consideration, and

$$\boldsymbol{\psi}_n = \cos(k_n z),\ k_n = \frac{\omega_n}{a} = n\frac{\pi}{L_c},\ E_n^2 = \tfrac{1}{2} S_c L_c$$

where S_c and L_c are the cross sectional area and the length of the combustion chamber respectively, and z denotes the longitudinal coordinate. For a general combustor chamber, the values of S_c and L_c are taken to be 0.6 m and 0.031 m^2, as used in (Culick, 1976a, 1976b). In addition, the ratio of specific heats, γ, is 1.23, the chamber temperature is 2000 K, and, correspondingly, the sound speed, a, is 849 m/s. Therefore, substitution of these parameters into Equation (5.14c) and (5.14d) yields, k_2 = -373494.7878; k_3 = 0.16525. In terms of k_0 and k_1, the expressions were given by Culick and his colleague (Culick, 1976a, 1976b; Yang et al., 1987, 1988, 1990) as,

$$k_0 = 2\theta_n \omega_n \text{ and } k_1 = 2\varsigma_n$$

Taking the particular values of ζ_n, θ_n employed by Culick (1976a, 1976b) as -0.5 and 3.0, respectively, one can obtain the following numerical values,

$$k_0 = 55.23 \text{ and } k_1 = -1.0$$

Γ is adopted as the variable bifurcation parameter which physically represents the intensity of heat-release oscillation, and the corresponding angular velocity, ω_c, is 1.5. The latter value is reasonable, in particular given the low-frequency nature of the combustion instability.

Due to θ monotonically increasing, a Poincaré section Ω, that is necessarily intersected by any trajectory, can be set up as,

$$\Omega = \{(\mathbf{x}, \theta) \in \mathbb{R}^2 \times S^1 \mid \theta = \theta_0\} \tag{5.17}$$

with $\theta_0 = 0$, that is, the plane at $t = 0$.Therefore, the Poincaré map (stroboscopic map) is obtained by observing the state of the system (5.16) at discrete time instances as,

$$t_n := n\frac{2\pi}{\omega_c} = nT_c \quad , n = 1, 2, \ldots$$

sampled at constant time intervals T_c.

In terms of the numerical integration of the dynamic system (5.16), a fourth order Runge-Kutta-Fehlberg method is employed by Mathews (1992). The bifurcation diagram is generated by using the second iterative method, which was adopted by Lynch (2005). The bifurcation parameter, Γ, is smoothly increased from 0 to 4.0 and then decreased back to zero. Note that the x_1 and x_2 are initially specified to comprise a random number field between 0 and 1, whereas for the case referring to decreasing Γ, the initial conditions are prescribed as the final results of the increase process. In addition, the appropriate integration time was specified to capture a duration as long as possible.

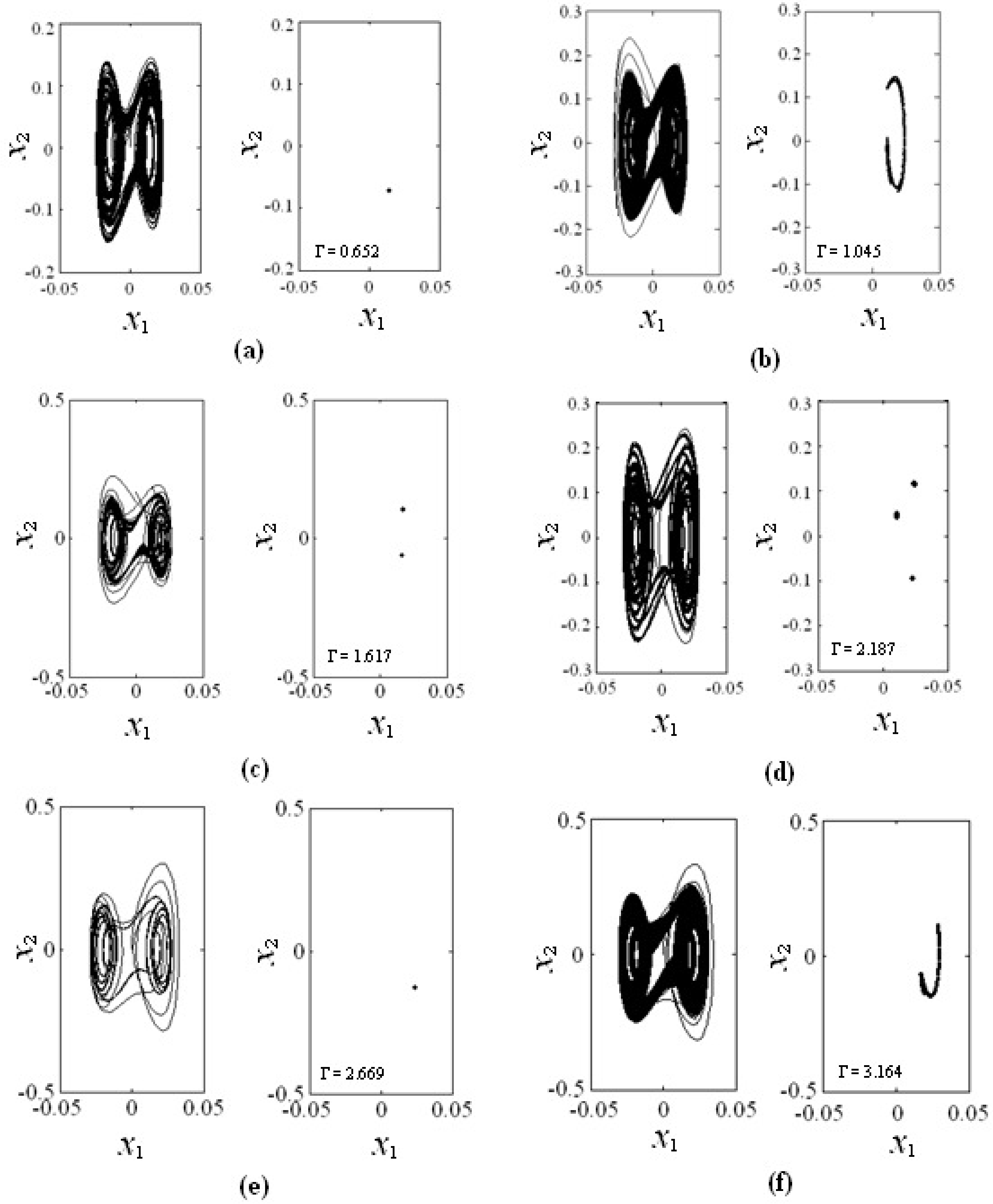

Fig. 5.1 A Gallery of Phase Portraits and Poincaré Maps for the Dynamic System (a) Γ = 0.652 (Forced period one); (b) Γ = 1.045 (Chaos);

(c) Γ = 1.617 (Period-two subharmonic);(d) Γ =2.187 (Period-three subharmonic);

(e) Γ = 2.669 (Forced period one); (f) Γ = 3.164 (Chaos)

5.3.2 Results and Discussion

Fig. 5.1 shows a set of phase portraits along with their Poincaré map at different bifurcation parameter values, Γ. When Γ = 0.652, there exists a period-one solution for the system (see Fig. 5.1 (a)), incorporating a closed curve in the phase plane and a single point in the section at $\theta = 0$. When Γ=1.045, the system becomes chaotic and on the Poincaré map, a strange attractor appears (see Fig. 5.1(b)). When Γ = 1.617, a period-two solution (subharmonic oscillations) appears and two intersection points are observed on the corresponding Poincaré map, while Γ = 2.187, a period-three solution (subharmonic oscillations) emerges. When Γ = 3.164, the system returns to a chaotic behaviour and when Γ assumes values of 3.4 and3.6, there appear period-one solutions again.

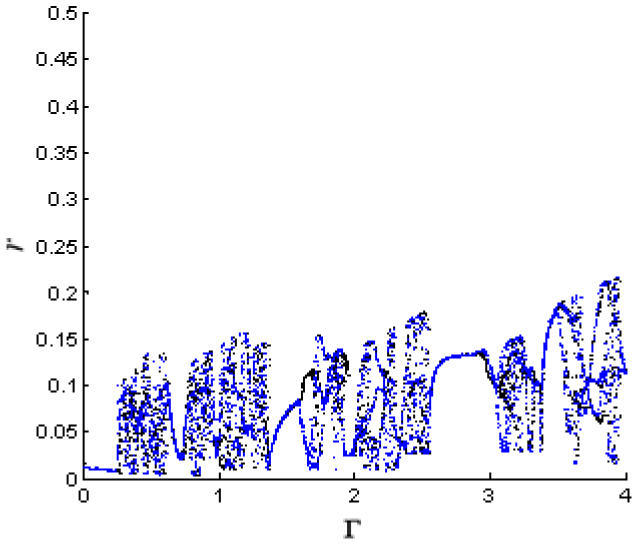

Fig. 5.2 Bifurcation Diagram for the One-Mode Dynamic System (r is the distance of the point in the Poincaré map from the origin and Γ is the bifurcation parameter.)

Fig. 5.2 shows a bifurcation diagram as the bifurcation parameter is increased from 0 to 4.0 and then decreased back to zero. The vertical axis labelled *r* denotes the distance of the point in the Poincaré map from the origin (0, 0). The solid curve lying between $0 \le \Gamma \le 0.3$ is characterized by the steady-state behaviour. If Γ is approximately in the range of 0.5-0.6, 1.01-1.3, and 2.3-2.4, the system exhibits chaos. It is interesting to note that a period-three solution appears as Γ is about 2.187. Although the above is an idealized example displaying a marginally significant behaviour in terms of physical relevance, even this simple system model can provide an indication of the behaviour regarding the cascading of the energy produced by combustion to finally end up as acoustic energy. Furthermore, the energy-flow process displays an extreme sensitivity to initial conditions, especially regarding the amplitude of the combustion fluctuations. If the bifurcation parameter Γ, is held below 2.5, the system may sample a chaotic neighbourhood of the phase space after which it mainly returns to a periodic behaviour.

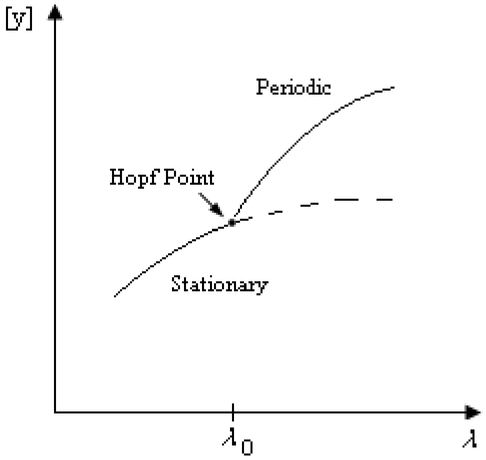

Fig. 5.3 Hopf Bifurcation Illustrated in Branching Diagrams

5.4 Two-mode Dynamic Model

The Hopf points play an extremely important role in nonlinear analysis, which connect a branch of equilibria and various periodic oscillations (Seydel, 1994), as shown in Fig. 5.3. This particular nonlinear analysis presented below is employed to study the Hopf points and the corresponding system behaviour existing in the neighbourhood of such points in detail. It was noticed that the Hopf bifurcation point, even for a steady state, has seldom been considered regarding the particular dynamic aspects of thermo-acoustic instability. Thus, it makes sense to identify and reveal the nature of the interchange between equilibrium state and periodic oscillations for the case of interest.

5.4.1 Formulation

(1) Analytical method

In this section, following the method of Yang et al. (1987, 1988), the time-varying amplitude η_n is defined as a function of A_n and B_n,

$$\eta_n(t) = A_n(t)\sin(\omega_n t) + B_n(t)\cos(\omega_n t) \tag{5.18}$$

and A_n and B_n are expressed as functions of the amplitude and phase,

$$A_n = y_n(t)\cos\varphi_n(t),\ B_n = y_n(t)\sin\varphi_n(t)$$

The combustion process employed in the paper was similar to that given by Yang et al. (1987), i.e., the model displays the appropriate sensitivity to pressure and velocity fluctuations. The nonlinear combustion response is given as,

$$\mathbf{Q} = \mathbf{Q}_p \left[1 + f_v |\mathbf{u}'|\right]$$

where $\mathbf{Q}_p$ is the heat release rate based on the linear pressure-coupled response, $\mathbf{Q}$ is the instantaneous heat release, and f_v is the velocity-coupled response function. Substitution of this expression into Equation (5.11-13) yields,

$$\{F_n\}_c = \frac{\gamma}{\bar{\rho} E_n^2} \oiint \psi_n \frac{\partial}{\partial t}\left[C_1 p' + C_2 p' |u'|\right] ds \tag{5.19}$$

in which, C_1 and C_2 are associated with the linear and nonlinear combustion process, given by Yang et al. (1987).

Considering the two modes, substitution of Equations (5.18) and (5.19) into (5.11) yields the two-mode dynamic model,

$$\frac{dy_1}{dt} = \mathbf{F}_{y,1}(\mathbf{y}, \xi) = \alpha_1 y_1 - \beta y_1 y_2 + \xi_1 y_1^2 \tag{5.20a}$$

$$\frac{dy_2}{dt} = \mathbf{F}_{y,2}(\mathbf{y}, \xi) = \alpha_2 y_2 + \beta y_1^2 + 4\xi_2 y_1 y_2 \tag{5.20b}$$

where y denotes the amplitude of pressure oscillation, and

$$\xi_1 = \frac{28}{45\pi} G \omega_1$$

$$\xi_2 = \tfrac{32}{35} \xi_1$$

$$G = \frac{L^2 R}{\pi} \frac{C_2 a^2}{\gamma E_n^2}$$

in which ξ_1 and ξ_2 result from the nonlinear combustion response, L and R denote the combustor length and diameter, respectively, and the dimensionless coefficient, G, was defined to capture the influence of combustion processes and combustor chamber dimensions, as in the work (Yang et al., 1987). β is derived from the second-order nonlinear acoustics, defined as,

$$\beta = \frac{\gamma + 1}{8\gamma}\omega_1$$

and α_1 and α_2 are model coefficients, which are related to first-order nonlinear acoustics, defined as

$$\alpha_1 = -\frac{1}{2}D_{11}$$

$$\alpha_2 = -\frac{1}{2}D_{22}$$

where, D_{11} and D_{22} are the coefficients in Equation of (5.15), which might be complex.

Initially, one calculates the steady states, viz., $\dot{\mathbf{y}} = 0$, to obtain,

$$\alpha_1 y_1 - \beta y_1 y_2 + \xi_1 y_1^2 = 0 \tag{5.21a}$$

$$\alpha_2 y_2 + \beta y_1^2 + 4\xi_2 y_1 y_2 = 0 \tag{5.21b}$$

Solving Equation (5.21a), the following results,

$$y_1^* = 0\text{ , or, } y_1^* = \frac{\beta y_2^* - \alpha_1}{\xi_1}$$

Correspondingly, Equation (5.21b) yields,

$$y_2^* = 0\text{ , or,}$$

$$\left(\frac{\beta^3}{\xi_1^2}+\frac{4\xi_2\beta}{\xi_1}\right)y_2^2+\left(\alpha_2-\frac{2\alpha_1\beta^2}{\xi_1}-\frac{4\xi_2\alpha_1}{\xi_1}\right)y_2+\frac{\beta\alpha_1^2}{\xi_1^2}=0$$

which leads to

$$\begin{cases} y_1^* = \dfrac{-(\alpha_2\xi_1+4\alpha_1\xi_2)\pm\left[(\alpha_2\xi_1+4\alpha_1\xi_2)^2-4\alpha_1\alpha_2\left(\beta^2+4\xi_1\xi_2\right)\right]^{\frac{1}{2}}}{2\left(\beta^2+4\xi_1\xi_2\right)} \\ y_2^* = \dfrac{\alpha_1+\xi_1 y_1^*}{\beta} \end{cases} \tag{5.22a}$$

$$\text{or, } \begin{cases} y_1^* = 0 \\ y_2^* = 0 \end{cases} \tag{5.22b}$$

The above results are in accord with those given by Yang et al. (1987). From Equation (5.20), one can derive the Jacobian matrix to check for stability,

$$\mathbf{J}_{\mathbf{y}} = \begin{bmatrix} \alpha_1-\beta y_2+2\xi_1 y_1 & -\beta y_1 \\ 2\beta y_1+4\xi_2 y_2 & \alpha_2+4\xi_2 y_1 \end{bmatrix} \tag{5.23}$$

For the trivial branch, substitution of Equation (5.22b) into (5.23) yields

$$\mathbf{J}_{\mathbf{y}} = \begin{bmatrix} \alpha_1 & 0 \\ 0 & \alpha_2 \end{bmatrix}$$

Hence, considering the particular nature of the resulting solution, i.e., the criterion of stability to ensure that the real parts of all eigenvalues are negative, is given as,

$$\mathrm{Re}[\alpha_1]<0$$

$$\mathrm{Re}[\alpha_2]<0$$

Taking into account the physical meaning of **y**, it is reasonable to choose the '+' sign in (5.22a). Thus, for the nontrivial branch, substituting Equation (5.22a) into Equation (5.23), the following is obtained,

$$\mathbf{J}_{\mathrm{y}} = \begin{bmatrix} \xi_1 S & -\beta S \\ 2\beta S + \dfrac{4\xi_2(\alpha_1 + \xi_1 S)}{\beta} & \alpha_2 + 4\xi_2 S \end{bmatrix} \tag{5.24}$$

where,

$$S := \frac{-(\alpha_2\xi_1 + 4\alpha_1\xi_2) + \left[(\alpha_2\xi_1 - 4\alpha_1\xi_2)^2 - 4\alpha_1\alpha_2\beta^2\right]^{\frac{1}{2}}}{2\left(\beta^2 + 4\xi_1\xi_2\right)}$$

and $\lambda = \xi_1$, as the branch parameter arising from combustion response, is incorporated in S. The eigenvalues μ are calculated via the determinant,

$$0 = \begin{vmatrix} \xi_1 S - \mu & -\beta S \\ 2\beta S + \dfrac{4\xi_2(\alpha_1 + \xi_1 S)}{\beta} & \alpha_2 + 4\xi_2 S - \mu \end{vmatrix} = \mu^2 + \Lambda_1\mu + \Lambda_2 \tag{5.25}$$

where

$$\Lambda_1 := -(\xi_1 S + 4\xi_2 S + \alpha_2)$$

and

$$\Lambda_2 := \left(2\beta^2 + 8\xi_1\xi_2\right)S^2 + (4\alpha_1\xi_2 + \alpha_2\xi_1)S$$

At the Hopf bifurcation point, the characteristic polynomial has a pair of purely imaginary roots defined as $\pm i\chi$. Hence, the polynomial can be written as,

$$\pm\left(\mu^2 + \chi^2\right) \tag{5.26}$$

It is noted that the value of χ is still unknown. However, this can be obtained by equating the coefficients of the characteristic polynomial of Equations (5.25) and (5.26) as they are identical at the Hopf bifurcation points. In this regard, one obtains,

$$\xi_1 S + 4\xi_2 S + \alpha_2 = 0 \tag{5.27a}$$

$$\chi^2 = \left(2\beta^2 + 8\xi_1\xi_2\right)S^2 + \left(4\alpha_1\xi_2 + \alpha_2\xi_1\right)S \tag{5.27b}$$

In addition, Equation (5.25) yields the eigenvalues as,

$$\mu_{1,2} = \frac{-\Lambda_1 \pm \sqrt{\Delta}}{2}$$

where $\Delta = \Lambda_1^2 - 4\Lambda_2$.

Obviously, if $\Delta \le 0$, the real part of the eigenvalues is,

$$\mathrm{Re}\left(\mu(\xi_1)\right) = -\frac{\Lambda_1}{2}$$

Thus, according to Hopf theorem, the corresponding non-degeneracy condition is,

$$\left.\frac{d(\xi_1 S)}{d\xi_1}\right|_{\xi_1=\xi_0} \neq 0 \tag{5.28a}$$

If $\Delta > 0$, the real parts of the eigenvalues are obtained respectively,

$$\mu_1 = \frac{-\Lambda_1 + \sqrt{\Delta}}{2} \text{ and } \mu_2 = \frac{-\Lambda_1 - \sqrt{\Delta}}{2}$$

After some manipulations, the corresponding non-degeneracy condition is,

$$\left(\left.\frac{d\Lambda_1}{d\xi_1}\right|_{\xi_1=\xi_0}\right)^2 \neq \left[\frac{\left(\Lambda_1\frac{d\Lambda_1}{d\xi_1}-2\frac{d\Lambda_2}{d\xi_1}\right)^2}{\Delta}\right]_{\xi_1=\xi_0} \tag{5.28b}$$

Provided the above non-degeneracy condition, viz. Equation (5.28), is satisfied, the value of bifurcation parameter at the Hopf point is derived as,

$$\xi_0 = \frac{\beta}{\left[1-\frac{163}{35}\left(\frac{\alpha_1}{\alpha_2}\right)\right]^{\frac{1}{2}}} \tag{5.29}$$

where $\frac{\alpha_2-\alpha_1}{\alpha_2} > \frac{128}{163}$, and then the corresponding initial period of the 'first' periodic oscillation is given by,

$$T_0 = \frac{2\pi}{\chi} \tag{5.30}$$

Furthermore, it is interesting to note that if $|\alpha_2| \to \infty$ and $|\alpha_2| > |\alpha_1|$, one finds,

$$\xi_{0,\lim} = \lim_{|\alpha_2|\to\infty} \frac{\beta}{\left[1-\frac{163}{35}\left(\frac{\alpha_1}{\alpha_2}\right)\right]^{\frac{1}{2}}} = \beta \tag{5.31}$$

(2) Numerical method

The algorithm to compute the Hopf points adopts the method proposed in (Seydel, 1994; Roose et al., 19; Sohn et al., 2000). As mentioned above, the Hopf points are characterized by a pair of purely imaginary eigenvalues (defined as $\pm i\chi$) of the Jacobian $\mathbf{J}_{\mathbf{y}}(\mathbf{y}_o, \xi_o)$. In this respect, the equation written as,

$$\mathbf{J}_{\mathrm{y}}(\mathbf{y}_{\mathbf{0}}, \xi_0)\mathbf{v} = i\chi\mathbf{v} \tag{5.32}$$

holds for a nonzero complex vector **v** = **h** + *i***g**. Substitution of this expression into Equation (5.29) yields two equations,

$$\mathbf{J}_{\mathrm{y}}\mathbf{h} = -\chi\mathbf{g} \tag{5.33a}$$

$$\mathbf{J}_{\mathrm{y}}\mathbf{g} = \chi\mathbf{h} \tag{5.33b}$$

In order to normalize **v**, impose, for example,

$$\mathbf{v}_k = 1$$

Combining Equations (5.21) and (5.33), one obtains the governing system with (3×2+2) equations given as,

$$\begin{pmatrix} \mathbf{F}_{\mathrm{y}}(\mathbf{y}, \xi) \\ \mathbf{J}_{\mathrm{y}}(\mathbf{y}, \xi)\mathbf{h} + \chi\mathbf{g} \\ \mathbf{J}_{\mathrm{y}}(\mathbf{y}, \xi)\mathbf{g} - \chi\mathbf{h} \\ h_k - 1 \\ g_k \end{pmatrix} = 0 \tag{5.33}$$

where k is an index, and, in general, one can pick any integer arbitrarily in the range $1 \le k \le 2$. In this study, k is taken to be 1. This system can be solved by adopting a routine nonlinear equation solver; here, Newton's method is employed. The above numerical method to calculate Hopf points is widely utilized in heat and mass transfer computations including chemical reactions as reported in (He and Clavin, 1993; Kubíček and Holodniock, 1984; Roose and Hlaváček, 1983).

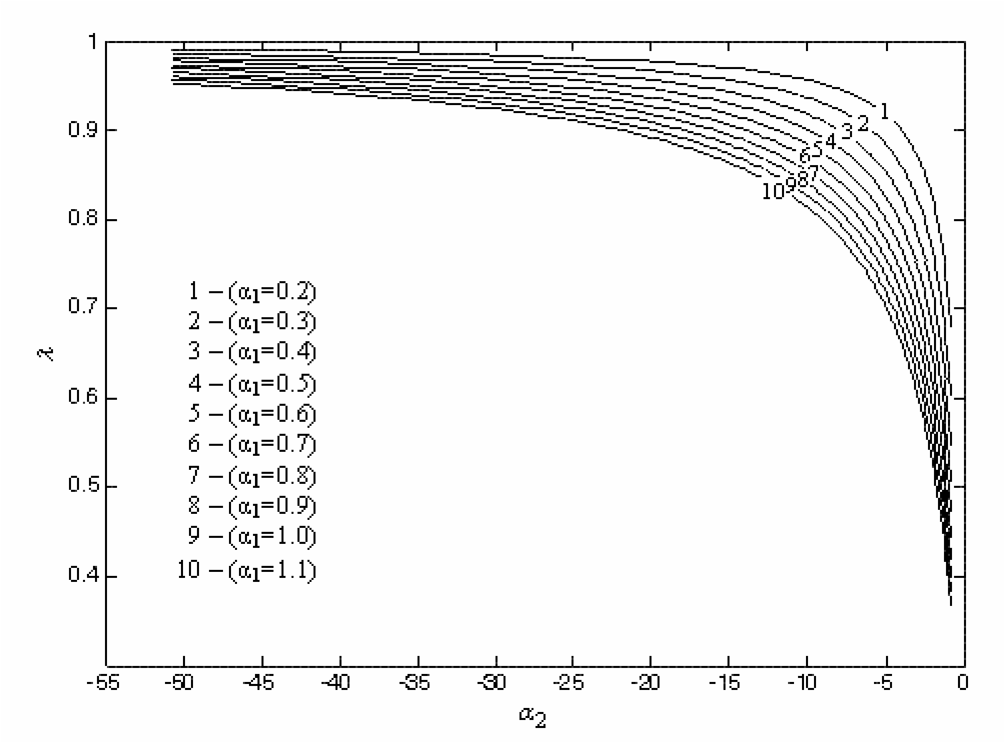

Fig. 5.4 Hopf Bifurcation vs. α_2 under Different α_1

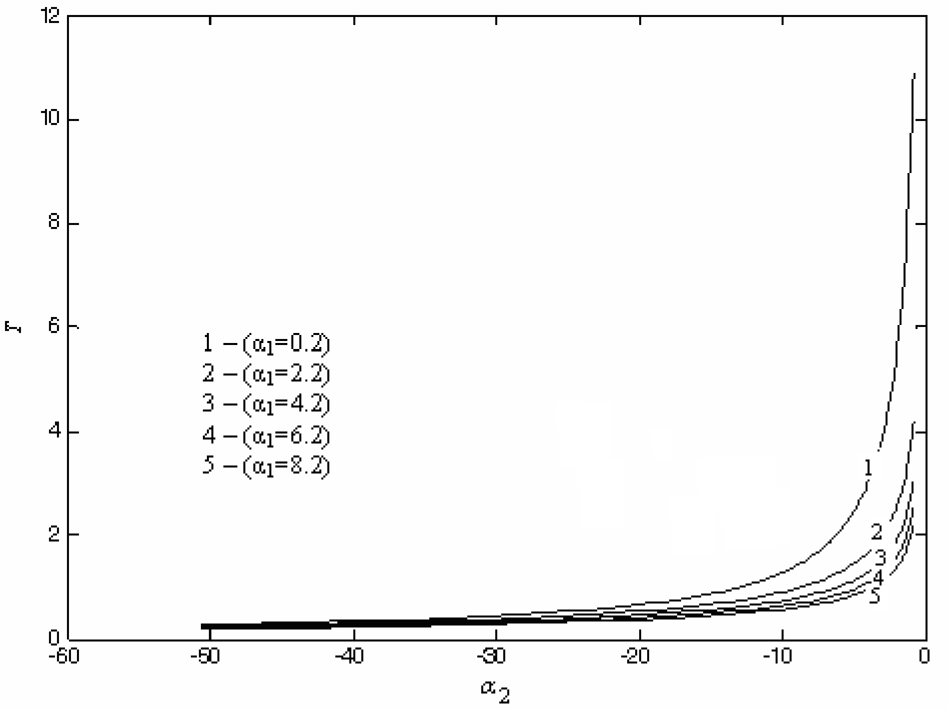

Fig. 5.5 Period at Hopf Points vs. α_2 under Different α_1

5.4.2 Results and Discussion

Table 5.1 shows the bifurcation parameter and the corresponding period at Hopf points under different coefficients as resolved by numerical and analytical methods. It is revealed that the analytical results are in good agreement with numerical values and the analytical formulae, (5.29) and (5.30), are reasonable to adopt. The slight difference between them is due to truncation errors during the numerical computations.

Fig. 5.4 shows that the values of bifurcation parameter at Hopf points vary with the co-efficient α_2, for different α_1. It is found that at a given α_1, the bifurcation parameter at a Hopf point increases rapidly with decreasing α_2 in the range from 0 to -10 and then climbs gradually. Its limited value tends to 1 as $\beta = 1.0$, as illustrated in Equation (5.31). At a given α_2, it decreases with increase in α_1, which can be anticipated in Equation (5.30) as well. Fig. 5.5 displays the dependence of the period at Hopf points on the coefficient α_2, under different α_1 values. It is seen that the period at Hopf points reduces sharply with decrease in α_2 in the range of 0 to -10 and then decreases gradually. In addition, at a given α_2, the period at Hopf points increases with decreasing of α_1.

Table 5.1 Comparison of Analytical and Numerical Results

$\beta = 1.0$		Analytical Results		Numerical Results	
α_1	α_2	ξ_0	T_0	ξ_0	T_0
0.2	-0.8	0.67973980655870	10.90825618788190	0.67973980656	10.90825618800
0.2	-0.6	0.62593214071185	13.30337193654330	0.62593214071	13.30337193700
0.4	-2.0	0.71954949745653	4.64380806193062	0.71954949746	4.64380806190
1.0	-10.0	0.82599104630559	1.08363591718134	0.82599104631	1.08363591720
5.0	-20.0	0.67973980655870	0.43633024751528	0.67973980656	0.43633024752
10.0	-40.0	0.67973980655870	0.21816512375764	0.67973980656	0.21816512376

As mentioned above, a Hopf bifurcation arises if a fixed point of a dynamical system loses stability as a pair of complex conjugate eigenvalues of the linearization around the fixed point cross the imaginary axis of the complex plane. Thus, it is expected to reveal the emergence of a limit cycle branching from the fixed point, which has been observed numerically and experimentally in terms of thermo-acoustic instability (Levine and Baum, 1981; Lieuwen, 2002). In this regard, the emergence of Hopf bifurcation might result in a limit cycle for the system of interest.

5.5 Energy Transition between Acoustic Modes

As pointed out in Section 2.3, there are infinite acoustic modes essentially existing in the combustion chamber. Thus, it is of paramount importance to identify the acoustic energy transited among modes.

5.5.1 Formulation

Neglecting the third-order effect since, as pointed out by Yang et al. (1995), the amplitudes and phases of each mode are slightly modified by third-order acoustics, the acoustic conservation equations for one-dimensional motions (Culick, 2006) are given as,

$$\bar{\rho}\frac{\partial u'}{\partial t} + \frac{\partial p'}{\partial x} = F \tag{5.34a}$$

$$\frac{\partial p'}{\partial t} + \gamma\bar{p}\frac{\partial u'}{\partial x} = P \tag{5.34b}$$

where

$$F = -\{[M]\}_1 - \{M\}_2 - \{[M]\}_2 \tag{5.35a}$$

$$P = -\{[p]\}_1 - \{p\}_2 + \frac{R}{C_v}\dot{\mathbf{Q}}' \tag{5.35b}$$

$$\{[M]\}_1 = \bar{\rho}\bar{u}\frac{\partial u'}{\partial x} \tag{5.35c}$$

$$\{M\}_2 = \rho'\frac{\partial u'}{\partial t} + \rho'\bar{u}\frac{\partial u'}{\partial x} + \bar{\rho}u'\frac{\partial u'}{\partial x} \tag{5.35d}$$

$$\{[M]\}_2 = \rho'\bar{u}\frac{\partial u'}{\partial x} \tag{5.35e}$$

$$\{[p]\}_1 = \bar{u}\frac{\partial p'}{\partial x} \tag{5.35f}$$

$$\{p\}_2 = u'\frac{\partial p'}{\partial x} + \gamma p'\frac{\partial u'}{\partial x} \tag{5.35g}$$

Combination of Equation (5.34a) and Equation (5.34b) yields,

$$\frac{\partial^2 p'}{\partial x^2} - \frac{1}{\bar{a}}\frac{\partial^2 p'}{\partial t^2} = \frac{\partial F}{\partial x} - \frac{1}{\bar{a}^2}\frac{\partial P}{\partial t} \tag{5.36}$$

Using Equation (5.10) and the properties associated with Green function given by Equations (5.8-9), one can obtain

$$\ddot{\eta}_n + \omega_n^2\eta_n = \underbrace{\frac{1}{\bar{p}E_n^2}\int_V \frac{\partial P}{\partial t}\psi_n(x)dV}_{\Im_1} - \underbrace{\frac{\bar{a}^2}{\bar{p}E_n^2}\int_V \frac{\partial F}{\partial x}\psi_n(x)dV}_{\Im_2} \tag{5.37}$$

In terms of a simplified case, viz., a Rijke tube shown in Fig. 5.6, only longitudinal modes in the chamber are considered and

$$\psi_m = \cos(k_m x) \tag{5.38a}$$

$$k_m = \frac{m\pi}{L} \tag{5.38b}$$

$$E_n^2 = \frac{1}{2} S \cdot L \tag{5.38c}$$

where L is the length of Rijke tube and S is the cross-section area of the tube.

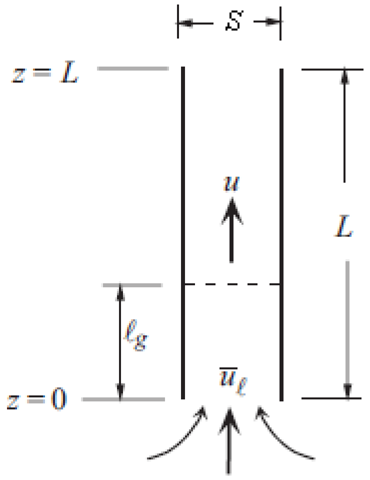

Fig. 5.6 Sketch of a Rijke Tube

Substituting Equation (5.35f) and Equation (5.35g) into the first term on the right side of Equation (5.37), one can obtain,

$$\begin{aligned}\Im_1 = \frac{1}{\bar{p}E_n^2}\int_V \frac{\partial P}{\partial t}\psi_n(x)dV = & \underbrace{-\frac{1}{\bar{p}E_n^2}\int_V \bar{u}\frac{\partial^2 p'}{\partial t\partial x}\psi_n(x)dV}_{\Lambda_1} \underbrace{-\frac{1}{\bar{p}E_n^2}\int_V \frac{\partial u'}{\partial t}\frac{\partial p'}{\partial x}\psi_n(x)dV}_{\Lambda_2} \\ & \underbrace{-\frac{1}{\bar{p}E_n^2}\int_V u'\frac{\partial^2 p'}{\partial t\partial x}\psi_n(x)dV}_{\Lambda_3} \underbrace{-\frac{1}{\bar{p}E_n^2}\int_V \gamma\frac{\partial p'}{\partial t}\frac{\partial u'}{\partial x}\psi_n(x)dV}_{\Lambda_4} \\ & \underbrace{-\frac{1}{\bar{p}E_n^2}\int_V \gamma p'\frac{\partial^2 u'}{\partial x\partial t}\psi_n(x)dV}_{\Lambda_5} + \underbrace{\frac{R/C_V}{\bar{p}E_n^2}\int_V \frac{\partial \dot{Q}'}{\partial t}\psi_n(x)dV}_{\Lambda_6}\end{aligned} \tag{5.39}$$

Substitutions of Equations (5.10a), (5.10b) and (5.38a) into Equation (5.39) yield,

$$\Lambda_1 = -\frac{\bar{u}SL}{E_n^2}\int_0^L \sum_{m=0}^{\infty} -k_m \dot{\eta}_m \sin(k_m x)\cdot\cos(k_n x)dx = 0 \tag{5.40a}$$

$$\begin{aligned}\Lambda_2 &= -\frac{S}{\gamma E_n^2}\sum_{i=1}^{\infty}\sum_{j=0}^{\infty}\int_0^L \frac{\ddot{\eta}_i}{k_i^2}\eta_j k_i k_j \sin(k_i x)\sin(k_j x)\cos(k_n x)dx \\ &= -\frac{LS}{4\gamma E_n^2}\left\{2\sum_{i=1}^{\infty}\ddot{\eta}_i\eta_i + \sum_{i=1}^{\infty}\frac{k_{i+n}}{k_i}\ddot{\eta}_i\eta_{i+n}\right\}\end{aligned} \tag{5.40b}$$

$$\begin{aligned}\Lambda_3 &= -\frac{S}{\gamma E_n^2}\sum_{i=1}^{\infty}\sum_{j=0}^{\infty}\int_0^L \frac{\dot{\eta}_i}{k_i^2}\dot{\eta}_j k_i k_j \sin(k_i x)\sin(k_j x)\cos(k_n x)dx \\ &= -\frac{LS}{4\gamma E_n^2}\left\{2\sum_{i=1}^{\infty}\dot{\eta}_i\dot{\eta}_i + \sum_{i=1}^{\infty}\frac{k_{i+n}}{k_i}\dot{\eta}_i\dot{\eta}_{i+n}\right\}\end{aligned} \tag{5.40c}$$

$$\begin{aligned}\Lambda_4 &= \frac{S}{E_n^2}\sum_{i=1}^{\infty}\sum_{j=0}^{\infty}\int_0^L \frac{\dot{\eta}_i}{k_i^2}\dot{\eta}_j k_i^2 \cos(k_i x)\cos(k_j x)\cos(k_n x)dx \\ &= \frac{LS}{4E_n^2}\left\{2\dot{\eta}_n\dot{\eta}_0 + \sum_{i=1}^{\infty}\left(2\dot{\eta}_i\dot{\eta}_i + \dot{\eta}_i\dot{\eta}_{i+n}\right) + \sum_{i=n+1}^{\infty}\dot{\eta}_i\dot{\eta}_{i-n} + \sum_{i=1}^{n-1}\dot{\eta}_i\dot{\eta}_{n-i}\right\}\end{aligned} \tag{5.40d}$$

$$\begin{aligned}\Lambda_5 &= \frac{S}{E_n^2}\sum_{i=1}^{\infty}\sum_{j=0}^{\infty}\int_0^L \frac{\ddot{\eta}_i}{k_i^2}\eta_j k_i^2 \cos(k_i x)\cos(k_j x)\cos(k_n x)dx \\ &= \frac{LS}{4E_n^2}\left\{2\ddot{\eta}_n\eta_0 + \sum_{i=1}^{\infty}\left(2\ddot{\eta}_i\eta_i + \ddot{\eta}_i\eta_{i+n}\right) + \sum_{i=n+1}^{\infty}\ddot{\eta}_i\eta_{i-n} + \sum_{i=1}^{n-1}\ddot{\eta}_i\eta_{n-i}\right\}\end{aligned} \tag{5.40e}$$

by using the triangular relation and the orthogonal property given as

$$\int_0^L \sin(k_m x)\cdot\cos(k_n x)dx = 0$$

$$\int_0^L \sin(k_i x)\sin(k_j x)\cos(k_n x)dx = \begin{cases} 0, & for\ i=n, j=0 \\ \dfrac{L}{2}, & for\ i-j=n=0, j\neq 0 \\ \dfrac{L}{4}, & for\ i-j=\pm n, j\neq 0 \\ -\dfrac{L}{4}, & for\ i+j=n, j\neq 0 \end{cases}$$

$$\int_0^L \cos(k_i x)\cos(k_j x)\cos(k_n x)dx = \begin{cases} \dfrac{L}{2}, & for\ i=n\neq 0, j=0 \\ \dfrac{L}{2}, & for\ i-j=n=0, j\neq 0 \\ \dfrac{L}{4}, & for\ i-j=\pm n, j\neq 0 \\ \dfrac{L}{4}, & for\ i+j=n\neq 0, j\neq 0 \end{cases}$$

Similarly, substitutions of the Equations (5.35c), (5.35d) and (5.35e) into the second term on the right side of Equation (5.37) lead to

$$\begin{aligned} \Im_2 = -\frac{\overline{a}^2}{\overline{p}E_n^2}\int_V \frac{\partial F}{\partial x}\psi_n(x)dV = & \underbrace{\frac{\overline{a}^2}{\overline{p}E_n^2}\int_V \overline{\rho}\overline{u}\frac{\partial^2 u'}{\partial x^2}\psi_n(x)dV}_{\Xi_1} + \underbrace{\frac{1}{\overline{p}E_n^2}\int_V \frac{\partial u'}{\partial t}\frac{\partial p'}{\partial x}\psi_n(x)dV}_{\Xi_2} \\ & \underbrace{+\frac{1}{\overline{p}E_n^2}\int_V p'\frac{\partial^2 u'}{\partial t\partial x}\psi_n(x)dV}_{\Xi_3} \underbrace{+\frac{1}{\overline{p}E_n^2}\int_V \overline{u}\frac{\partial p'}{\partial x}\frac{\partial u'}{\partial x}\psi_n(x)dV}_{\Xi_4} \\ & \underbrace{+\frac{1}{\overline{p}E_n^2}\int_V \overline{u}p'\frac{\partial^2 u'}{\partial x^2}\psi_n(x)dV}_{\Xi_5} + \underbrace{\frac{\overline{a}^2}{\overline{p}E_n^2}\int_V \overline{\rho}\frac{\partial u'}{\partial x}\frac{\partial u'}{\partial x}\psi_n(x)dV}_{\Xi_6} \\ & \underbrace{+\frac{\overline{a}^2}{\overline{p}E_n^2}\int_V \overline{\rho}u'\frac{\partial^2 u'}{\partial x^2}\psi_n(x)dV}_{\Xi_7} + \underbrace{\frac{1}{\overline{p}E_n^2}\int_V \overline{u}\frac{\partial p'}{\partial x}\frac{\partial u'}{\partial x}\psi_n(x)dV}_{\Xi_8} \\ & \underbrace{+\frac{1}{\overline{p}E_n^2}\int_V \overline{u}p'\frac{\partial^2 u'}{\partial x^2}\psi_n(x)dV}_{\Xi_9} \end{aligned} \tag{5.41}$$

Substituting Equations (5.35c), (5.35d) and (5.35e) into Equation (5.41), one can obtain,

$$\Xi_1 = \frac{k_n \overline{\rho}\,\overline{u}\,\overline{a}^2 SL}{2\overline{p}E_n^2\gamma}\dot{\eta}_n \tag{5.42a}$$

$$\Xi_2 = \frac{SL}{4\gamma E_n^2}\sum_{j=1}^{\infty}\left(2\ddot{\eta}_i\eta_i + \frac{k_{i+n}}{k_i}\ddot{\eta}_i\eta_{i+n}\right) \tag{5.42b}$$

$$\Xi_3 = -\frac{SL}{4\gamma E_n^2}\left\{2\ddot{\eta}_n\eta_0 + \sum_{i=1}^{\infty}\left(2\ddot{\eta}_i\eta_i + \ddot{\eta}_i\eta_{i+n}\right) + \sum_{i=n+1}^{\infty}\ddot{\eta}_i\eta_{i-n} + \sum_{i=1}^{n-1}\ddot{\eta}_i\eta_{n-i}\right\} \tag{5.42c}$$

$$\Xi_6 = \frac{\overline{a}^2\overline{\rho}SL}{4\overline{p}\gamma^2E_n^2}\left\{2\dot{\eta}_n\dot{\eta}_0 + \sum_{i=1}^{\infty}\left(2\dot{\eta}_i\dot{\eta}_i + \dot{\eta}_i\dot{\eta}_{i+n}\right) + \sum_{i=n+1}^{\infty}\dot{\eta}_i\dot{\eta}_{i-n} + \sum_{i=1}^{n-1}\dot{\eta}_i\dot{\eta}_{n-i}\right\} \tag{5.42d}$$

$$\Xi_7 = -\frac{\overline{\rho}\overline{a}^2 SL}{4\overline{p}\gamma^2E_n^2}\sum_{j=1}^{\infty}\left(2\dot{\eta}_i\dot{\eta}_i + \frac{k_{i+n}}{k_i}\dot{\eta}_i\dot{\eta}_{i+n}\right) \tag{5.42e}$$

$$\Xi_4 = \Xi_5 = \Xi_8 = \Xi_9 = 0 \tag{5.42f}$$

Substitutions of Equations (5.39), (5.40a-e), (5.41) and (5.42a-f) into Equation (5.37) yield

$$\begin{aligned}
\ddot{\eta}_n + \omega_n^2\eta_n = {} & \frac{R/C_v}{\overline{p}E_n^2}\int_0^L \frac{\partial\dot{Q}'}{\partial t}\psi_n dx \\
& + \Gamma_1\sum_{i=1}^{\infty}\left(2\dot{\eta}_i^2 + \frac{k_{i+n}}{k_i}\dot{\eta}_{\mathbf{i}}\dot{\eta}_{\mathbf{i+n}}\right) \\
& + \Gamma_2\left\{2\dot{\eta}_{\mathbf{n}}\dot{\eta}_{\mathbf{0}} + \sum_{i=1}^{\infty}\left(2\dot{\eta}_i^2 + \dot{\eta}_{\mathbf{i}}\dot{\eta}_{\mathbf{i+n}}\right) + \sum_{i=n+1}^{\infty}\left(\dot{\eta}_{\mathbf{i}}\dot{\eta}_{\mathbf{i-n}}\right) + \sum_{i=1}^{n-1}\left(\dot{\eta}_{\mathbf{i}}\dot{\eta}_{n-i}\right)\right\} \\
& + \Gamma_3\left\{2\ddot{\eta}_{\mathbf{n}}\eta_{\mathbf{0}} + \sum_{i=1}^{\infty}\left(2\ddot{\eta}_i\eta_i + \ddot{\eta}_{\mathbf{i}}\eta_{\mathbf{i+n}}\right) + \sum_{i=n+1}^{\infty}\left(\ddot{\eta}_{\mathbf{i}}\eta_{\mathbf{i-n}}\right) + \sum_{i=1}^{n-1}\left(\ddot{\eta}_{\mathbf{i}}\eta_{n-i}\right)\right\} \\
& + \Gamma_4\dot{\eta}_n
\end{aligned} \tag{5.43}$$

where,

$$\Gamma_1 = -\left[\frac{\overline{a}^2\overline{\rho}SL}{4\overline{p}\gamma^2E_n^2} + \frac{SL}{4\gamma E_n^2}\right]$$

$$\Gamma_2 = -\Gamma_1$$

$$\Gamma_3 = \frac{SL}{4E_n^2} - \frac{SL}{4E_n^2 \gamma}$$

$$\Gamma_4 = \frac{k_n \overline{\rho} \overline{u} \overline{a}^2 SL}{2\overline{p} E_n^2 \gamma}$$

5.5.2 Results and Discussion

Equation (5.43) can exhibit that the nonlinear coupling between acoustic modes exists and the energy can be transferred from lower modes to higher modes and vice versa, due to the nonlinear gasdynamics in the chamber. In terms of the first eight modes, the process of inter modal energy transfer is demonstrated in Table 5.2. The energy transferred from lower to higher modes is primarily due to the terms, $\dot{\eta}_i \dot{\eta}_{n-i}$ and $\ddot{\eta}_i \eta_{n-i}$, whereas the terms $\dot{\eta}_i \dot{\eta}_{n+i}$ and $\ddot{\eta}_i \eta_{n+i}$ cause the reverse energy transfer from higher to lower modes. In addition, it should be noted that the differences between the current work and the discussion reported by Culick (1975) are the terms of $\ddot{\eta}_i \eta_{n-i}$ and $\ddot{\eta}_i \eta_{n+i}$ in Equation (5.43). However, with the assumption $\ddot{\eta}_i \approx -\omega_i^2 \eta_i$ in Culick's work, $\eta_i \eta_{n-i}$ and $\eta_i \eta_{n+i}$ should be correspondingly equivalent to $\eta_i \eta_{n-i}$ and $\eta_i \eta_{n+i}$. Furthermore, it is shown in Equation (5.43) that the nonlinear coupling between the acoustic modes can cause an energy cascade and limit cycle consequently occurs, as pointed out by Yang et al (1995). In general, energy feeds into the system by the linear process of the unstable modes and is transferred/dissipated by the nonlinear coupling. Moreover, the first term on the right hand of Equation (5.43) representing the combustion process also interact with modes implicitly as one of the sources of the *n*th oscillator associated with all the others modes, as discussed in Section 5.3.

Table 5.2 Inter-modal Energy Transfers

Mode Number	**Energy Transfer Up the Modes**	**Reverse Energy Transfer**
1		12, 23, 34, 45, 56, 67, 78
2	11	13, 24, 35, 46, 57, 68
3	12, 21	14, 25, 36, 47, 58
4	13, 22, 31	15, 26, 37, 48
5	14, 23, 32, 41	16, 27, 38
6	15, 24, 33, 42, 51	17, 28
7	16, 25, 34, 43, 52, 61	18
8	17, 26, 35, 44, 53, 62, 71	
Terms	$\dot{\eta}_i\dot{\eta}_{n-i}$; $\ddot{\eta}_i\eta_{n-i}(\eta_i\eta_{n-i})$	$\dot{\eta}_i\dot{\eta}_{n+i}$; $\ddot{\eta}_i\eta_{n+i}(\eta_i\eta_{n+i})$

5.6 Conclusions

In terms of the one-mode dynamic model, which includes a simple harmonic oscillatory behaviour for combustion, the system exhibits a variety of chaotic behaviours for some select range of the bifurcation parameter. These results are of significance to partially illustrate the emergence of the overshoot zone accompanying the linear zone and the nonlinear limit cycle discovered in pressure trajectory with time (Sterling, 1993). The formulae for the bifurcation parameter and the period at Hopf points are derived for the two-mode dynamic model. In the range from 0 to -10, the bifurcation parameter and the corresponding period at Hopf points vary rapidly. The limit value of the bifurcation parameter tends to be β, which is one of coefficients in the model. As mentioned in the above section, the Hopf points appear at the intersection between a branch of equilibria and a branch of periodic oscillations. In this regard, it makes sense to note that the Hopf point computations are important to reveal the bifurcation structure associated with the thermo-acoustic instability in a given system and might result in the occurrence of limit cycle. Moreover, in terms of a simplified case, it is found in Equation (5.43) that the coupling and the resulting energy transfer between the acoustic modes are primarily caused by the nonlinear gasdynamics. Additionally, the nonlinear coupling between the acoustic modes can cause an energy cascade and limit cycle consequently occurs. The energy transferred from lower to higher modes results from the terms $\dot{\eta}_i\dot{\eta}_{n-i}$ and $\ddot{\eta}_i\eta_{n-i}$, whereas the terms $\dot{\eta}_i\dot{\eta}_{n+i}$ and $\ddot{\eta}_i\eta_{n+i}$ cause the reverse energy transfer from higher to lower modes.

This study can be extended to complement CFD simulations. As the experimental method used by Lieuwen (2002) to study the impact of mean inlet velocity on the pressure oscillations in a premixed combustor, a certain parameter, such as the equivalence ratio, which potentially might play an important role in thermo-acoustic instability, is highlighted and a set of CFD simulations with a limited variation of this parameter are conducted. This is likely to achieve an in-depth understanding of thermo-acoustic instability and obtain a typical transitional behaviour similar to the findings of nonlinearity/chaotic behaviour as exemplified in this work, even though the detailed CFD simulations are comparatively costly and computationally intensive.

CHAPTER 6

NONLINEAR/CHAOTIC ANALYSIS, MODELLING AND CONTROL OF THERMO-ACOUSTIC INSTABILITIES DUE TO VAPORIZATION

6.1 Introduction

In this chapter, a discrete dynamic model is developed that accounts for both the combustion and the evaporation processes as distinct from models employing just the typical combustion description. In terms of different bifurcation parameters relevant to either combustion or evaporation, various bifurcation diagrams are presented. As part of the nonlinear characterization, the governing process Lyapunov exponent is calculated and employed to analyze the stability of the particular dynamic system. Furthermore, the OGY (Ott, Grebogi and Yorke, 1990) method and the minimum entropy control method to be described later are employed to control the chaotic performance of certain a/periodic motion. These methods are intended to form a rational basis for active/passive control of combustion instability as reported in the literature.

6.2 Formulation

Based on the methodology developed by Culick (1976a; 1976b), a new model is developed, for simplicity, by neglecting body forces but accounting for heat release and mass transfer between the liquid phase and the gaseous phase. The governing conservation equations may be given as,

Mass equation:

$$\frac{\partial \rho}{\partial t} + \nabla \cdot (\rho \mathbf{u}) = W_d \tag{6.1a}$$

Momentum equation:

$$\rho \frac{\partial \mathbf{u}}{\partial t} + \rho \mathbf{u} \cdot \nabla \mathbf{u} + \nabla p = \mathbf{F}_d \tag{6.1b}$$

Pressure equation:

$$\frac{\partial p}{\partial t} + \bar{\gamma} p \nabla \cdot \mathbf{u} = \frac{\overline{R}}{\overline{C}_v} \left[(\mathbf{u}_d - \mathbf{u}) \mathbf{F}_d + \dot{Q} + (e_{o,d} - e_{o,g}) W_d + (1 + \kappa) \overline{C}_v T W_d \right] \tag{6.1c}$$

where, ρ, $\mathbf{u}$, p and T are the density, velocity vector, pressure and temperature of mixture, respectively; $\overline{R}$ is the mass average gas constant for the gas/droplets mixture; W_d is the rate of conversion of droplets to gas; $\mathbf{F}_d$ is the inter-force between droplets and gases; κ is the ratio of the mass of droplets to the mass of gas in a unit volume of combustion chamber, which is assumed to be a constant in both space and time (Culick, 1976a; 1976b); $e_{o,d}$ and $e_{o,g}$ are stagnation internal energy of droples and stagnation internal energy of gases respectively; $\dot{Q}$ is heat release by reactions; e_o and e_{do} are the stagnation internal energy of gases and the stagnation internal energy of droplets, respectively; $\overline{C}_v$ and $\overline{C}_p$ are specific heats of gas/droplets mixture at constant volume and constant pressure respectively, $\overline{C}_v = (C_{v,g} + \kappa C_{v,d})/(1+\kappa)$ and $\overline{C}_v = (C_{p,g} + \kappa C_{p,d})/(1+\kappa)$; $\overline{\gamma}$ is the ratio of heat heats for the gas/droplets mixture, $\overline{\gamma} = \overline{C}_p / \overline{C}_v$; $\overline{a}$ is the average speed of sound for the mixture, $\overline{a}^2 = \overline{\gamma}\overline{R}\overline{T}$. Additionally, when combustion occurs unsteadily in a low Mach number flow, the sources owing to combustion and evaporation processes are far larger than the sound resulted from the other source mechanisms, as pointed out by Dowling et al. (1992). Therefore, in terms of the case of interest in this work, it makes sense to neglect the momentum transfer term between the droplets and the host fluid demonstrated in Equation (6.1b) in order to specifically investigate the driving mechanisms related to combustion and evaporation of droplets to combustion instability.

The variables in Equation (6.1) may be decomposed into the usual mean and fluctuating parts, written as,

$$\rho = \overline{\rho} + \rho'$$

$$u = \overline{u} + u'$$

$$p = \overline{p} + p'$$

$$T = \overline{T} + T'$$

$$\dot{Q} = \overline{\dot{Q}} + \dot{Q}'$$

$$W_d = \overline{W}_d + W_d'$$

Substitution of these expressions into Equations (6.1a-c) yields the linearized equations as,

$$\frac{\partial \rho'}{\partial t} + \bar{\rho}\nabla \mathbf{u}' = W_d' \tag{6.2a}$$

$$\bar{\rho}\frac{\partial \mathbf{u}'}{\partial t} + \nabla p' = 0 \tag{6.2b}$$

$$\frac{\partial p'}{\partial t} + \gamma\bar{p}\nabla \mathbf{u}' = \frac{R}{C_v}\mathbf{M}' \tag{6.2c}$$

where the source term, $\mathbf{M}'$, is,

$$\mathbf{M}' = \dot{Q}' + \left[(e_{do} - e_o) + (1+\kappa)C_v\bar{T}\right]W_d' \tag{6.3}$$

Combination of Equation (6.2b) and Equation (6.2c) and rearrangement lead to,

$$\nabla^2 p' - \frac{1}{\bar{a}^2}\frac{\partial^2 p'}{\partial t^2} = \frac{R}{C_v}\frac{\partial \mathbf{M}'}{\partial t} \tag{6.4}$$

The solution of the above non-homogeneous wave Equation (6.4) is approximated via a combination of the normal modes in the combustion chamber with unknown time-varying amplitudes,

$$p'(x,t) = \bar{p}\sum_{m=0}^{M\to\infty}\eta_m(t)\boldsymbol{\psi}_m(x) \tag{6.5}$$

Here, one can define a Green function written as,

$$G(x|x_0) = \sum_{n=0}^{\infty} A_n \boldsymbol{\psi}_n(x)$$

where $\boldsymbol{\psi}_n(x)$ satisfies the following properties,

$$\nabla^2\boldsymbol{\psi}_n(x) + k_n^2\boldsymbol{\psi}_n = 0 \tag{6.6}$$

$$\int_V \boldsymbol{\psi}_m(x)\boldsymbol{\psi}_n(x)dV = E_n^2\delta_{mn} \tag{6.7}$$

in which $E_n^2 = \int_V \boldsymbol{\psi}_\mathbf{n}^\mathbf{2}(x)dV$ and with the boundary condition given as

$$\hat{\mathbf{n}}\cdot\nabla\boldsymbol{\psi}_n(x) = 0 \tag{6.8}$$

Subtracting Equation (6.6) multiplied by p' from Equation (6.4) multiplied by $\boldsymbol{\psi}_n(x)$, and then integrating over the entire volume, one obtains,

$$\int_V [\boldsymbol{\psi}_n(x)\nabla^2 p' - p'\nabla^2\boldsymbol{\psi}_n(x)]dV - \int_V \boldsymbol{\psi}_n(x)\frac{1}{\bar{a}^2}\nabla^2 p' dV$$
$$-k_n^2\int_V p'\boldsymbol{\psi}_n(x)dV = -\int_V \boldsymbol{\psi}_n(x)\frac{\partial\mathbf{M}'}{\partial t}dV$$

According to the orthogonal property of $\boldsymbol{\psi}_n(x)$, this may be written as

$$\ddot{\eta}_n + \omega_n^2\eta_n = \frac{R/C_v}{\bar{p}E_n^2}\int_V \frac{\partial\mathbf{M}'}{\partial t}\boldsymbol{\psi}_n(x)dV \tag{6.9}$$

Thus, the pressure variations in a combustion chamber are dependent on a set of coupled oscillators which are driven by the heat release and mass addition integrals exemplified by the right-hand side of Equation (6.9).

6.3 Extended Rayleigh Criterion and Nonlinear Models

A bifurcation diagram for the dynamic system given by Equation (6.9) can be obtained by observing the behaviour of the oscillation energy (Sterling, 1993). By multiplying Equation (6.9) by $\dot{\eta}_n$ and integrating over one period, $\tau_n = 2\pi/\omega_n$, of oscillation, the change of the oscillation energy over one period may be expressed, as,

$$\Delta E_n = \frac{R/C_v}{\bar{p}E_n^2}\int\left\{\int_t^{t+\tau_n}\mathbf{M}'\dot{\eta}_n dt\right\}\boldsymbol{\psi}_n dV \tag{6.10}$$

where $\tau_n = \dfrac{2\pi}{\omega_n}$.

Using the assumptions that the amplitudes are slowly varying and the second derivative of η with respect to time is approximately $-\omega_n^2\eta_n$, which is used in the same manner as in that of Culick (1976a; 1976b; 1988; 1990; 2006), Yang et al. (1987; 1988; 1990), and Sterling (1993), the simplification of Equation (6.10) yields,

$$\Delta E_n = \frac{\gamma-1}{\bar{p}E_n^2}\int\left\{\int_t^{t+\tau_n}\mathbf{M}'p_n dt\right\}dV \tag{6.11}$$

where, the time-dependent pressure of the *n*-th mode is given by,

$$p_n = \bar{p}\eta_n(t)\boldsymbol{\psi}_n(\mathbf{r})$$

Equation (6.11) is the extended Rayleigh criterion which may be employed to examine the stability of the system under consideration. It indicates that if the energy and/or mass addition is in phase with the particular chamber acoustics, the acoustic energy may increase and, consequently, the wave may be amplified. Conversely, if they are out of phase, the wave may be damped. A nonlinear expression for the source term $\mathbf{M}'$ in terms of the pressure and/or velocity is required to depict the behaviour for the dynamic system of interest. Different nonlinear models of the combustion and/or evaporation response to pressure and/or velocity oscillations are put forward in what follows.

6.3.1 Delayed Combustion Response

Combustion processes are sensitive to the macroscopic flow variables, especially, pressure, temperature and velocity. The time-lag model proposed by Crocco and Cheng (1972) is one of the most extensively used combustion response models, which in essence provides a way to explain the coupling of heat perturbations with flow-field oscillations. In this model, the work of Sterling (1993) was extended, based on the notion that the heat release is proportional to the velocity associated with only one mode, but responds with a time delay, and the mass transfer due to evaporation is neglected. Therefore, a sinusoidal velocity may lead to a time-shifted, sinusoidal heat release. Thus, the heat release is given by,

$$\dot{Q}' = Q(\mathbf{r})\dot{\eta}_n(t - \vartheta) \tag{6.12}$$

and the delay is

$$\vartheta = \beta E$$

where β is proportionality constant between the time delay for the heat release and the oscillation energy, E. Assuming that,

$$\eta \approx E^{\frac{1}{2}} \sin(\omega t)$$

and substituting this into Equation (6.11) and integrating, with the assumption of a slowly varying time delay, one obtains

$$\Delta E = \mu E \sin(\omega \vartheta) \tag{6.13}$$

where μ is a bifurcation parameter related to the chamber dimension and acoustic modes.

Thus, the energy of the oscillator at cycle n+1 is,

$$E^*_{n+1} = E^*_n\left(1 + \mu \sin\left(E^*_n\right)\right) \tag{6.14}$$

where $E^* = E/(\beta\omega)$.

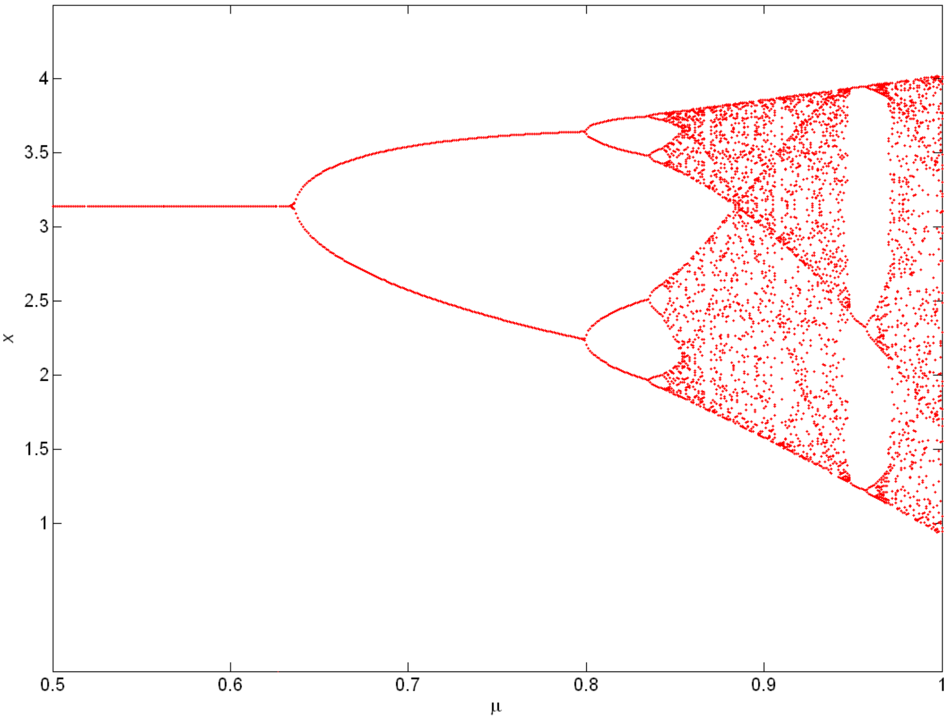

Fig. 6.1 Bifurcation Diagram for Time Delay Model

In terms of a typical system given by Sterling (1993), this discrete dynamical system was calculated assuming that μ is varying from 0.5 to 1.0, as a bifurcation parameter. A bifurcation diagram was obtained as shown in Fig. 6.1. For $\mu < 0.636$, a limit cycle occurs, as in Fig. 6.2 (a). When $0.636 < \mu < 0.799$, period-doubling bifurcations occur, as shown in Fig. 6.2(b), whereas, when $0.799 < \mu < 0.836$, period-four bifurcations appear in Fig. 6.2(c). When $0.836 < \mu < 0.8458$, period-eight bifurcations take place. As shown in Fig. 6.2(e), this discrete dynamic system displays a new type of behaviour known as intermittency, which indicates that periodic behaviour is interrupted by occasional chaotic bursts. It is noted that the transition to chaos occurs, as guided by the analysis regarding Lyapunov exponents presented in the following section.

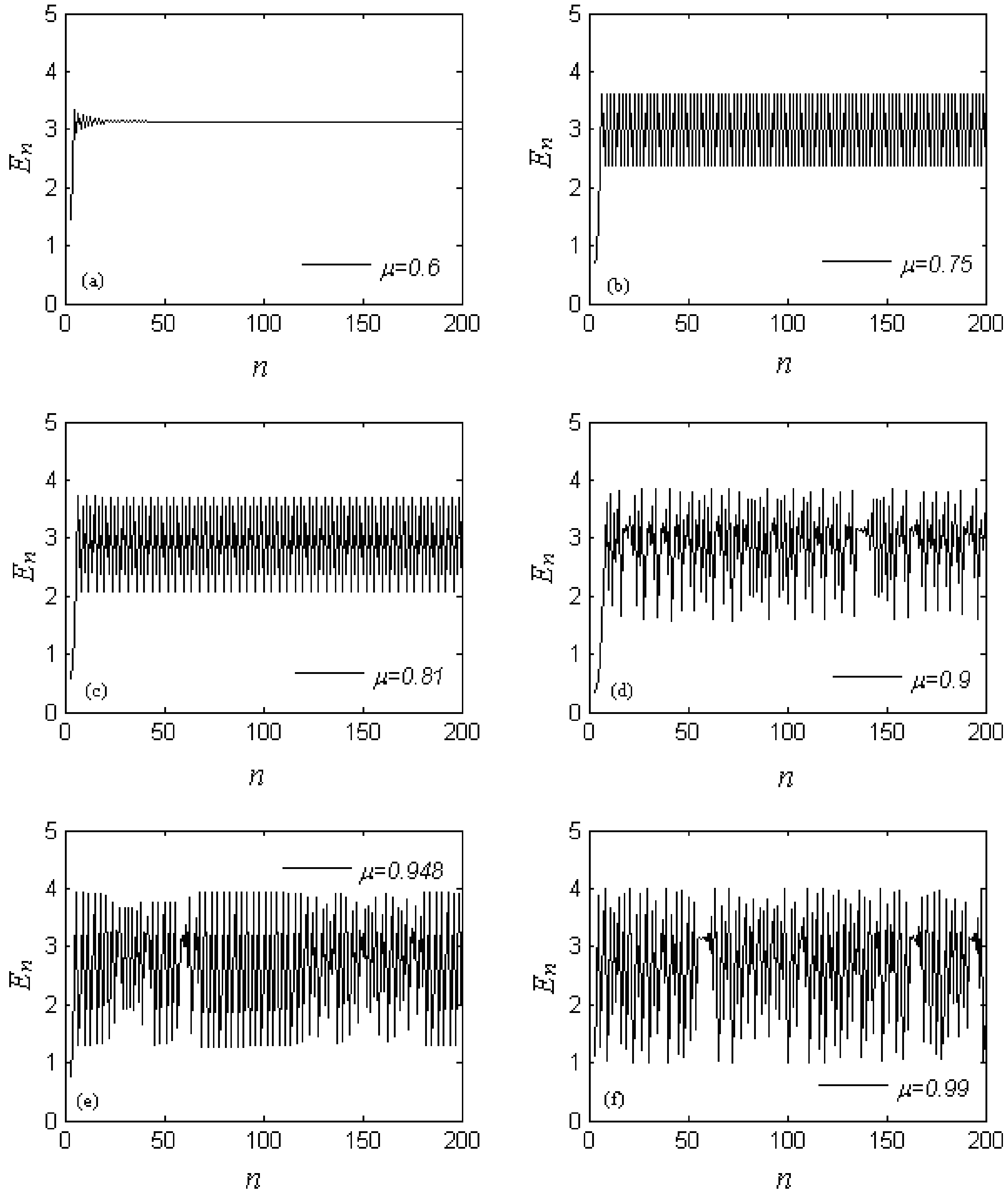

Fig. 6.2 Time Series Data of Oscillation Energy for Time Delay Model (a) Period-one (Limit cycle); (b) Period-doubling; (c) Period-four; (d) Chaos; (e) Intermittency Route; (f) Chaos

J. Feigenbaum discovered a remarkable a universal constant known as Feigenbaum constant in the mid-1970s, which is ubiquitous in nonlinear science (Lynch, 2004). The first six bifurcation points computed numerically are given in Table 1. If D_k is defined as,

$$D_k = b_{k+1} - b_k$$

then,

$$\delta = \lim_{k \to \infty} \frac{D_k}{D_{k+1}} = 4.669202....$$

In Table 6.1, the Feigenbaum constant calculated for the first six bifurcation points is slightly less than 4.669202. As expected, it should be approximated by the Feigenbaum constant if more bifurcation points are taken into account.

Table 6.1 Bifurcation Points and Feigenbaum Constant

Bifurcation Points (b_i)	**D_k**	**Feigenbaum Constant (δ)**
0.636	0.163	4.407
0.799	0.037	4.625
0.836	0.008	4.445
0.844	0.0018	4.510
0.8458	0.0004	
0.8462		

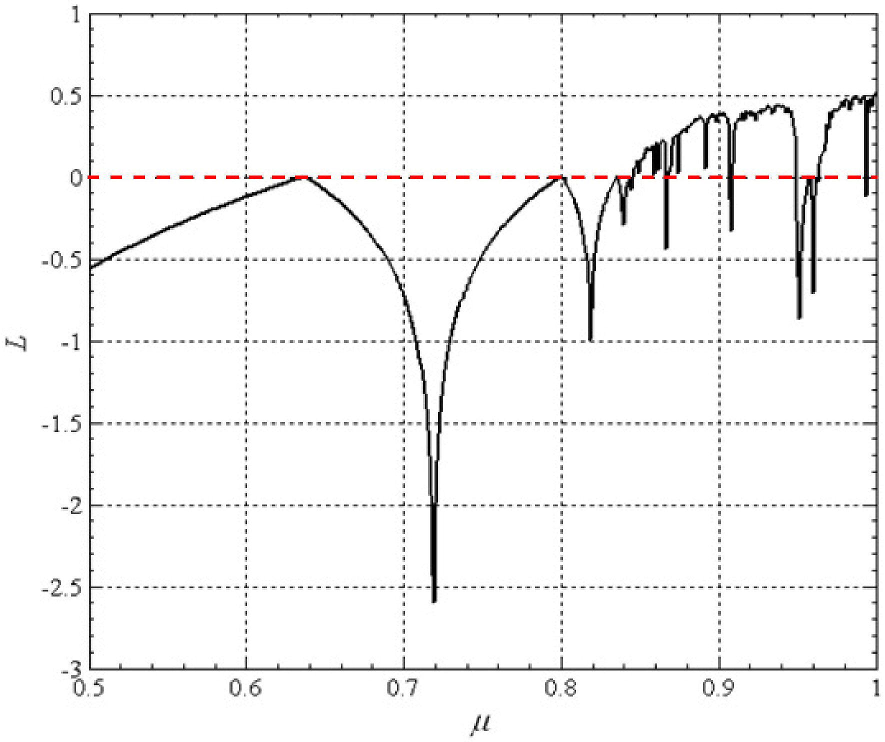

Fig. 6.3 Lyapunov Exponent for Time Delay Model

In addition, as indicated in/stability index, the Lyapunov exponent (Lynch, 2004), L, is computed using the derivative method defined by,

$$L = \frac{1}{n} \ln \left(\sum_i f'_\mu (x_i) \right) \tag{6.15}$$

where, f'_μ denotes differentiation with respect to x and x_1, x_2, …, x_i indicate successive iterations. Lyapunov theorem states that, if at least one of the average Lyapunov exponents is positive, then the system is chaotic; if the average Lyapunov exponent is negative, then the orbit is periodic; and when the average Lyapunov exponent is zero, a bifurcation occurs. Thus, Fig. 6.3 exhibits that the state of the system is stable initially, changes to chaotic and then restabilizes as shown in Fig. 6.2.

6.3.2 Bi-parameter Model

To further extend the above simple model, the droplet evaporation process is taken into consideration in addition to combustion. Equation (6.4) reveals that the evaporation rate of droplets may be thought of as a monopole source of sound, as the heat release resulting from combustion behaves in a similar vein to that of the heat release $\dot{\mathbf{Q}}'$, provided that the Doppler effect is neglected. In terms of evaporation, this model accounts for the following physicochemical processes related to the two distinct phases, (1) detachment of fuel molecules from the surface of the droplet into gas in the immediate vicinity of droplets, and (2) diffusion of fuel vapour from the surface of droplets into the ambient gas. In most practical applications, the second process is highlighted for modelling purposes, on the assumption that the fuel vapour in the vicinity of droplet surface is always saturated (Sazhin, 2006). A number of models have been proposed in the literature to account for the influence of the prevailing velocity field on the evaporation rate as given in literature (Abramzon and Sirignano, 1989; Zeng and Lee, 2002; Sazhin et al., 2004). In this work, it is assumed that the droplet radius rate of change owing to vaporization is mainly dependent on the relative velocity and temperature fields between phases, as provided by Sazhin (2006)

$$\frac{dR}{dt} = -\frac{\rho_g D_v B_d}{2\rho_l R}\mathbf{Sh}$$

where the Sherwood number, **Sh**, is expressed as (Sazhin, 2006),

$$\mathbf{Sh} = \left(2.0 + 0.6\mathbf{Re}_d^{1/3}\mathbf{Sc}_d^{1/3}\right)\frac{\ln(1 + B_d)}{B_d}$$

and

$$\mathbf{Re}_d \propto v$$

where **Re*d*** is the Reynolds number, $\mathbf{Re}_d = 2R\left|\mathbf{v}_p - \mathbf{u}_g\right| / \nu_g$; **Sc*d*** is the Schmidt number, $\mathbf{Sc}_d = \mu_g / \rho_g D_v$; ν_g is the kinematic viscosity of surrounding gas and D_v is the vapor diffusivity in air with density of ρ_g.

Thus, loosely speaking, the evaporation rate can be taken to depend proportionally on the cube root of the velocity of ambient gas, provided the temperature and velocity of droplets are constant. Assuming that,

$$W_d' = W(\mathbf{x})\left(\frac{\nabla \boldsymbol{\psi}_n(x)}{\bar{\gamma} k_n^2}\right)^{1/3} \dot{\eta}^{1/3}(t) \tag{6.16}$$

where $u' = \frac{1}{\bar{\gamma} k_n^2} \dot{\eta}(t) \nabla \boldsymbol{\psi}_n(\mathbf{x})$.

Substitution of Equations (6.16) and (6.12) into Equation (6.11) yields,

$$E_{n+1}^* = E_n^*\left(1 + \mu \sin\left(E_n^*\right) + \lambda E_n^{*-1/6}\right) \tag{6.17}$$

where λ is a bifurcation parameter related to the thermal dynamic properties of both ambient gas and droplets, chamber dimension and acoustic modes.

Taking into consideration a typical system given by by Culick (1976a; 1976b), this discrete dynamic system can be iterated numerically for any initial oscillation energy field. As the variable, μ, as a bifurcation parameter, is varying and λ is constant, bifurcation diagrams and corresponding Lyapunov exponent diagrams are obtained as shown in Figs. 6.4-5 and Figs. 6.6-7, respectively. Compared with Fig. 6.2, the evaporation effect plays an important role regarding the occurrence of chaos. It is found that chaos initially appears at $\mu \approx 0.84$ for $\lambda \approx 0$, at $\mu \approx 0.84$ for $\lambda \approx 1.0$, while the same behaviour is observed at $\mu \approx 0.96$ for $\lambda \approx 0.7$. In addition, the evaporation process as a source may substantially amplify the oscillatory performance of the system. In particular, the occurrence of the period-doubling bifurcation point is delayed, owing to the evaporation effect.

Assuming that the variable, λ, is varying from 0 to 1.1 and $\mu = 1.0$, a bifurcation diagram and a corresponding Lyapunov exponent diagram are obtained as shown in Fig. 6.8 and Fig. 6.9, respectively. The state of this dynamic system initially is chaotic and evolves into periodic motion at $\lambda \approx 0.4$ and then returns to chaos. This clearly indicates that the evaporation process, providing a driving force for combustion instabilities as pointed out by Tong and Sirignano (1989) and Duvvur et al. (1996), might complicate the analysis and understanding of the system of interest. Fig. 6.9 reveals that the occurrence of chaos has a high probability, compared with the case of no evaporation.

6.4 Controlling Chaos in the Nonlinear Model

6.4.1 OGY Method

6.4.1.1 Formulation

Since the publication of the seminal paper of Ott, Grebogi and Yorke (1990), the development of techniques for the control of chaotic phenomena has made great strides. In this work, the OGY method (Lynch, 2004) is developed for the control of instability and the analysis is restricted to control pulses designed to be proportionally periodic. In order to control the chaotic behaviour exemplified by the system given in Equation (6.17), instantaneous pulses may be employed to influence the variable E_n every p iterations, that is,

$$E_i \rightarrow kE_i$$

where k is a constant to be determined and p is the period. In addition, one may define,

$$f_{\lambda,\mu}(E_n) = E_n^*\left(1 + \mu \mathbf{sin}(E_n^*) + \lambda {E^*}_n^{-1/6}\right)$$

Thus, one defines a composite function $F_{\lambda,\mu}(E)$ by,

$$F_{\lambda,\mu}(E) = k f_{\lambda,\mu}^p(E) \tag{6.18}$$

A fixed point of the function $F_{\lambda,\mu}$ satisfies the equation,

$$k f_{\lambda,\mu}^p(E_s) = E_s \tag{6.19}$$

where, the fixed point E_s is stable if

$$\left| k \frac{d f_{\lambda,\mu}^p(E_s)}{dE} \right| < 1 \tag{6.20}$$

One further defines the function $C^p(E)$ by

$$C^p(E) = \frac{E}{f_{\lambda,\mu}^p(E)} \frac{d f_{\lambda,\mu}^p(E)}{dE}$$

Substituting this into Equation (6.20), one obtains

$$\left| C^p(E_s) \right| < 1 \tag{6.21}$$

Provided that Equation (6.21) holds, a fixed point of the system is a stable point of period p when the control is switched on. The functions, $C^i(E)$, i =1, 2, 3, 4, are shown in Fig. 6.10. Fig. 6.10 (a) indicates that fixed points of period one can be stabilized in three ranges of E_s values. For p = 2, Fig. 6.10 (b) shows that fixed points of period two can be stabilized in six ranges of E_s values, whereas Fig. 6.10 (c) and (d) exhibit that there are 11 and 24 acceptable ranges for fixed points of period three and four, respectively. This also shows that the control ranges are becoming restricted with the increase of periodicity.

6.4.1.2 Results and Discussion

Figs. 6.11-14 show time series data for specific examples when chaos is controlled to period-one, period-two, period-three and period-four behaviors. Note that the values of E_s chosen in Figs. 6.11-14 were derived from Fig. 6.10. The values of k were calculated using Equation (6.19). It was found that when the control is switched on, chaotic non-linear behaviour transitions onto specific periodic motions as a result, amplitudes damp considerably. In addition, this control methodology using instantaneous pulses prescribed via the algorithm just described may be regarded as providing the fundamental rational basis to influence combustion instability as exercised in current practice (Hathout et al., 2002; Paschereit and Gutmark, 2008).

6.4.2 Minimum Entropy Method

6.4.2.1 Formulation

In the past, a number of nonlinear control algorithms have been proposed for stochastic control in the literature (Chen, 2000; Yue and Wang, 2003; Lynch, 2004; Liu and Chen, 2004; Fuh and Tsai, 2007; Salarieh and Alasty, 2008). In this section, the minimum entropy control method is employed for the nonlinear models discussed above. Generally, the recurrence property is characteristic of chaotic systems, which have stationary probability density functions. Thus, the appropriately formulated entropy function for a nonlinear system based on the probability density reaches a minimum value and, correspondingly, the fixed point arises. As pointed out by Salarieh and Alasty (2008), the advantage of this method is that there is no need to present any information regarding the characteristic mathematical model of the system.

To generalize, consider a stochastic system as,

$$X_{n+1} = f(X_n, r_n) \tag{6.22}$$

where X_n is the state vector and r_n is the control action.

In the sense of Shannon, the entropy function of the chaotic system is defined as,

$$S(r) = -\int_{X \in \Omega} P(X,r) \ln P(X,r) dX \tag{6.23}$$

where P is the probability function and Ω is the whole phase space covering the states of the system which could be further divided into Z sub-regions denoted by Ω_i, $i = 1, 2, \ldots, Z$. Therefore, the probability function at the nth iteration is defined as

$$P_i(X,r) = \frac{N_i}{n} \tag{6.24}$$

where N_i is the number of points in the sub-region Ω_i.

Equation (6.24) may lead to

$$\frac{\partial P_i}{\partial r} = \frac{1}{n}\frac{\partial N_i}{\partial r} - \frac{N_i}{n^2}\sum_{k=1}^{Z}\frac{\partial N_k}{\partial r} \tag{6.25}$$

Thus, Equation (6.23) becomes

$$S(r) = -\sum_{i=1}^{Z} P_i \ln P_i \cdot \Delta\Omega \tag{6.26}$$

in which $\Delta\Omega$ is the length of sub-region.

To computationally implement the local minimum entropy, the gradient descent method is employed,

$$r_{n+1} = r_n - \omega \left.\frac{\partial S}{\partial r}\right|_{r=r_n} \tag{6.27}$$

where $\omega>0$ indicates that the entropy of the system is decreasing, as probed in (Yang et al., 1988, 1990).

Substitution of Equation (6.23) into Equation (6.27) may yield,

$$r_{n+1} = r_n + \omega \int_{X\in\Omega} \left[1 + \ln P(X,r)\right] \frac{\partial P(X,r)}{\partial r} dX \tag{6.28}$$

which can be approximated numerically,

$$r_{n+1} = r_n + \omega \sum_{i=1}^{Z} \left[1 + \ln P_i\right] \frac{\partial P_i}{\partial r} \Delta\Omega \tag{6.29}$$

Substituting Equation (6.25) into Equation (6.29), one may obtain

$$r_{n+1} = r_n + \omega \sum_{i=1}^{Z} \left[1 + \ln\left(\frac{N_i}{n}\right)\right] \cdot \left[\frac{1}{n}\frac{\partial N_i}{\partial r} - \frac{N_i}{n^2}\sum_{k=1}^{Z}\frac{\partial N_k}{\partial r}\right] \Delta\Omega \tag{6.30}$$

which may be rewritten numerically as

$$r_{n+1} = r_n + \omega \sum_{i=1}^{Z} \left[1 + \ln\left(\frac{N_i}{n}\right)\right] \cdot \left[\frac{1}{n}\frac{\Delta N_i}{\Delta r} - \frac{N_i}{n^2}\sum_{k=1}^{Z}\frac{\Delta N_k}{\Delta r}\right] \Delta\Omega \tag{6.31}$$

where $\Delta N_i = N_i(n)$-$N_i(n$-1) and $\Delta r = r(n)$-$r(n$-1). Additionally, since if the nth interation point lies in Ω_i, $\Delta N_i = 1$, otherwise, $\Delta N_i = 0$, Equation (6.31) becomes

$$r_{n+1} = r_n + \frac{\omega}{n\left(r_n - r_{n-1}\right)} \left\{\left[1 + \ln\left(\frac{N_i}{n}\right)\right] - \sum_{i=1}^{Z}\frac{N_i}{n} \cdot \left[1 + \ln\left(\frac{N_i}{n}\right)\right]\right\} \Delta\Omega \tag{6.32}$$

In addition, the control function r_n is changed to the following form

$$r_n = \varsigma_n \cdot \varepsilon_n = \varsigma_n \left(X_n - X^*\right) \tag{6.33}$$

where ε_n is the error feedback and X^* is the fixed value as defined.

Substitution of Equation (6.33) into Equation (6.32) leads to,

$$\varsigma_{n+1} = \varsigma_n + \frac{\omega}{n}\frac{1}{\varsigma_n - \varsigma_{n-1}}\left\{\left[1+\ln\left(\frac{N_k}{n}\right)\right] - \sum_{i=1}^{Z}\frac{N_i}{n}\left[1+\ln\left(\frac{N_i}{n}\right)\right]\right\}\cdot\Delta\Omega \tag{6.34}$$

Iterating the above equation in conjunction with Equation (6.22), it is easily seen that the entropy of the system continuously reduces, eventually to zero. Consequently, a fixed point can be arrived at.

6.4.2.2 Results and Discussion

Fig. 6.15 shows emergence of the fixed point for the nonlinear model, Equation (6.14) with μ = 0.94, in which chaotic behavior appears as shown in Fig. 6.1. In this case, the parameters of Equation (6.34) are defined as Z = 25, ω = 0.15. It was found that when the control is switched on, chaotic non-linear behaviour transitions onto specific periodic motions as a result, amplitudes damp considerably, as shown in Fig. 6.15 (a). In addition, the entropy of the system decreases as shown in Fig. 6.15 (b).

Stabilizing the fixed point of the nonlinear model, viz. Equation (6.17), with μ = 1.1 and λ = 0.7 is shown in Fig. 6.16, in which chaotic behavior appears as shown in Fig. 6.4. In this case, the parameters of Equation (6.34) are defined as Z = 25, ω = 0.23. It was found that when the control is switched on, the state converge to the fixed point, i.e. X^* = 2.8527, as shown in Fig. 6.16 (a). In addition, the entropy of the system reduces as shown in Fig. 6.16 (b).

6.5 Conclusions

Discrete dynamic models of the system under consideration are proposed, in which the nonlinearity is associated with the response of the heat release and mass transfer to pressure and/or velocity oscillations. In terms of the first model of delayed combustion response which was originally put forward by Sterling (1993), additional details regarding the nonlinear dynamic performance is presented. The transformation between a limit cycle, periodic motion and chaos is highlighted. Furthermore, the Feigenbaum constant is calculated, to be in line with the universally reported value. In addition, the Lyapunov exponent is obtained and it is found out that for $0<\mu<0.85$, the system is, in general, stable. This exponent may be used to capture the stability of the system of interest numerically and experimentally.

Moreover, the more complicated dynamic model which accounts for both the combustion and evaporation processes is developed as well. The bifurcation diagrams show that the mass addition can greatly influence the occurrence of bifurcation points and the amplitude of oscillation. For the case of varying λ and $\mu = 1.0$, initially chaotic behaviour arises, reflecting that, under certain circumstances, the vaporization of droplets will strengthen the heat release to drive the combustion instability. Additionally, the Lyapunov exponent is calculated pointing to the fact that that the chaotic range extent may increase in the presence of the vaporization process. Furthermore, the OGY method and minimum entropy method are employed to control the chaotic performance of the system. These can be complemented either numerically or experimentally to control the prevailing combustion instability.

A study of the bifurcation diagrams reveals that subharmonics can occur under various operating conditions. In experiments, one model parameter may be sufficient to highlight and control one or more of the bifurcation points influenced by the prevailing chaotic/subharmonic behaviour. For a velocity oscillation, the mass addition and heat release may be in phase with the pressure oscillation. Thus, it is reasonable to expect that certain bifurcations may result from combinations of certain droplet velocity and dropsize distribution.

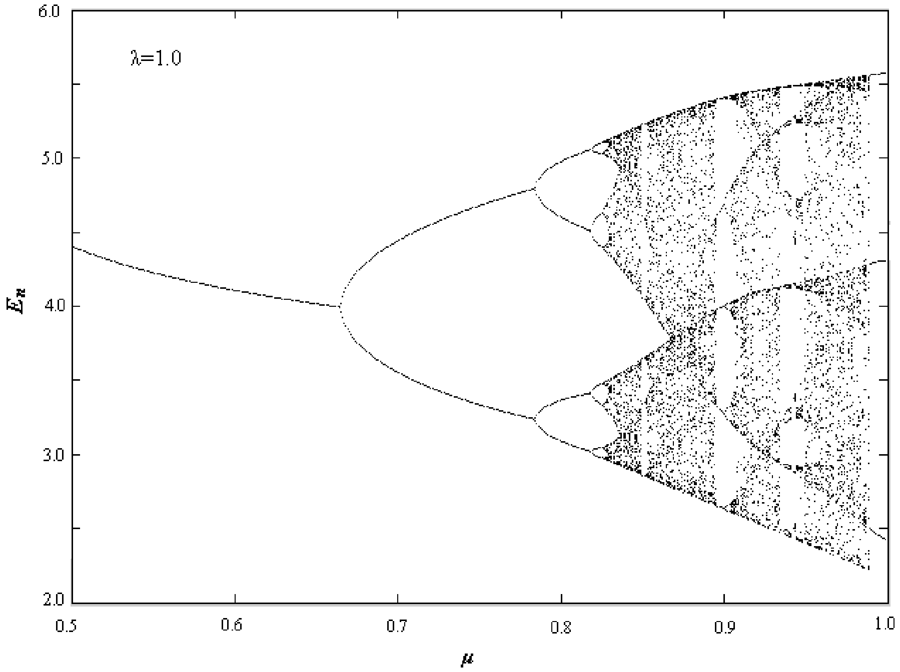

Fig. 6.4 Bifurcation Diagram for $\lambda = 1.0$

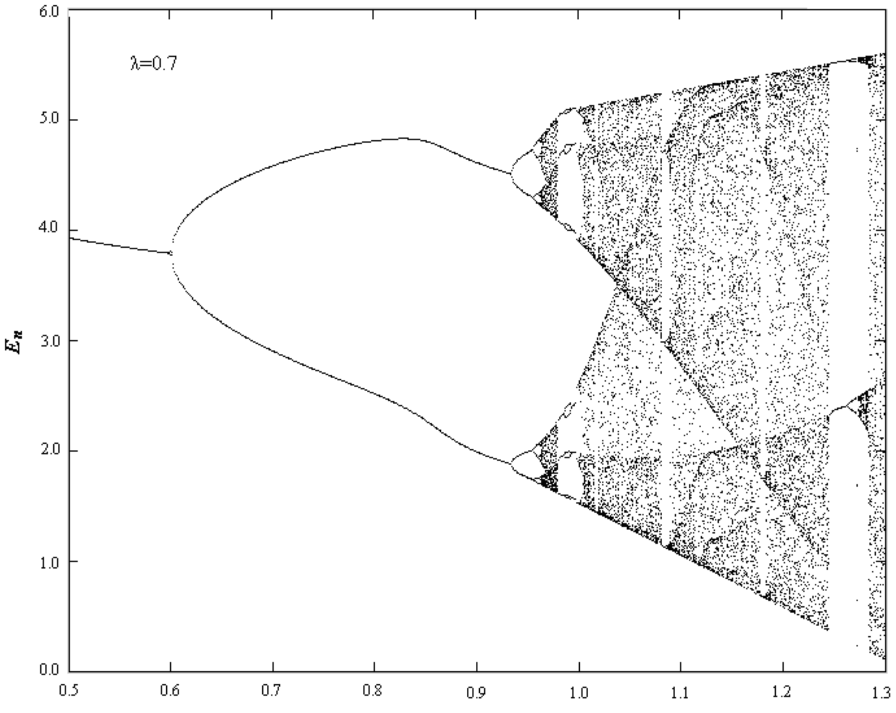

Fig. 6.5 Bifurcation Diagram for $\lambda = 0.7$

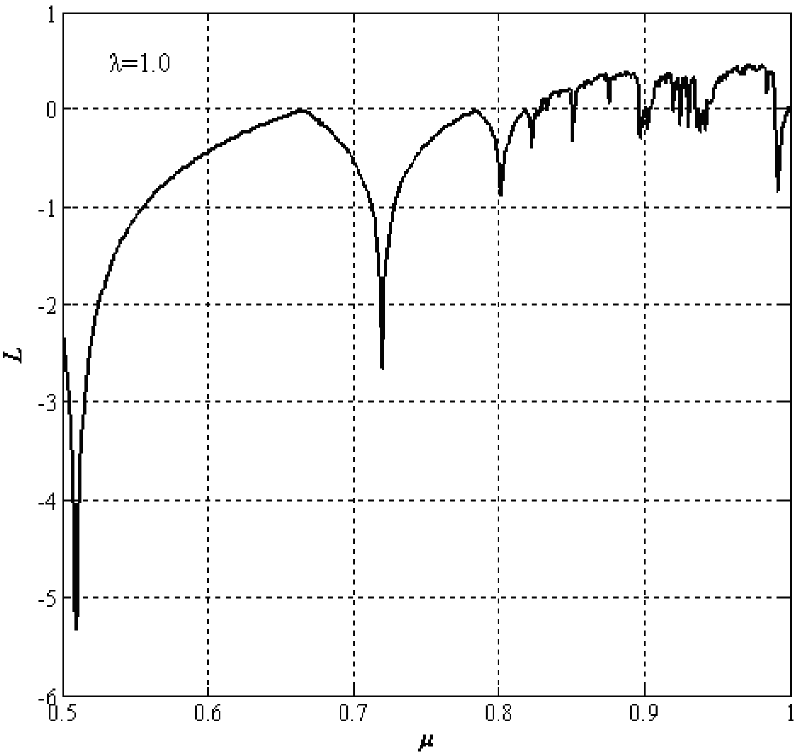

Fig. 6.6 Lyapunov Exponent Diagram for $\lambda = 1.0$

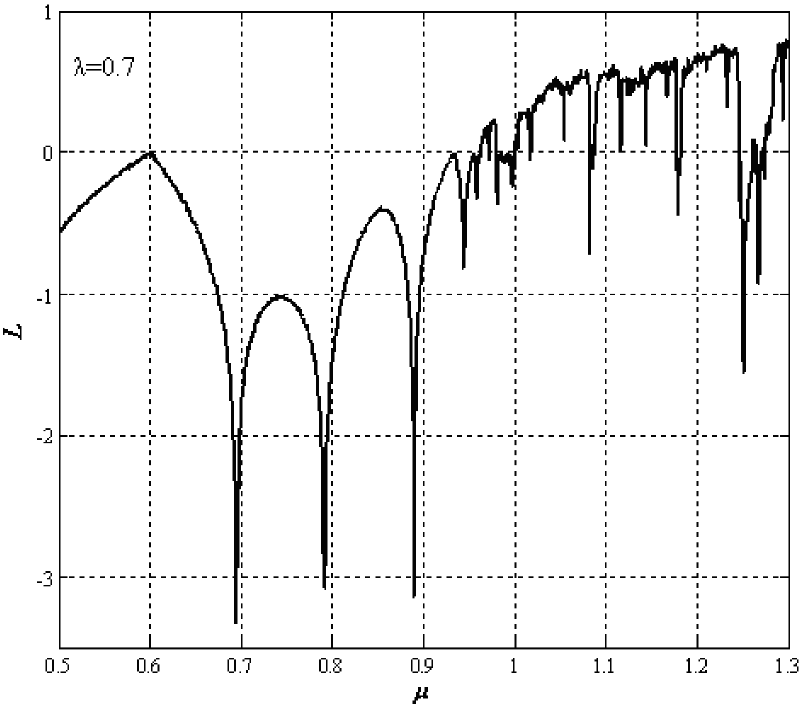

Fig. 6.7 Lyapunov Exponent Diagram for $\lambda = 0.7$

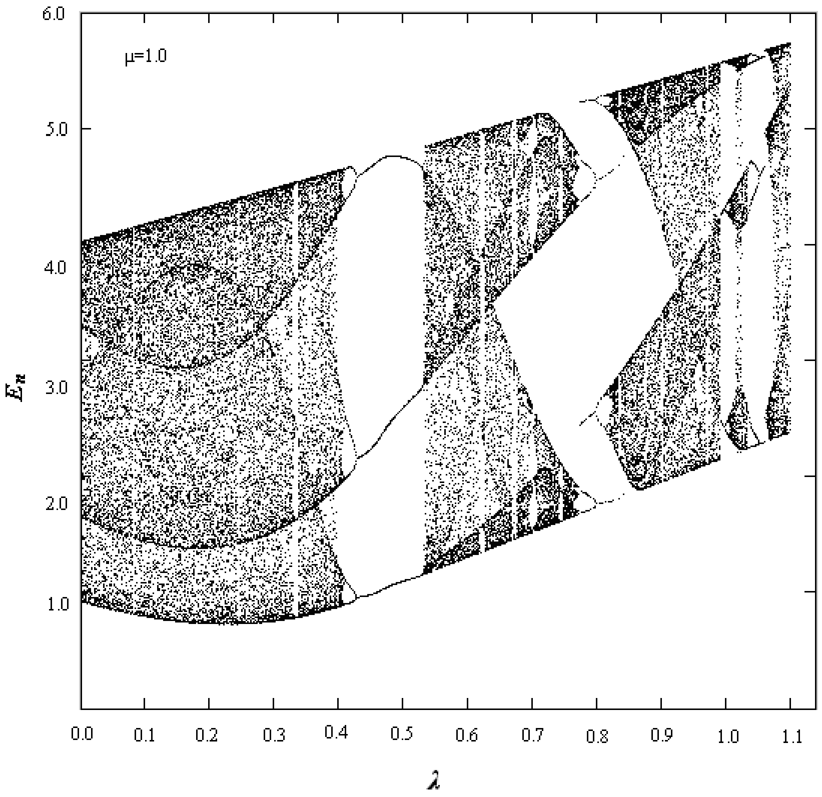

Fig. 6.8 Bifurcation Diagram for $\mu = 1.0$

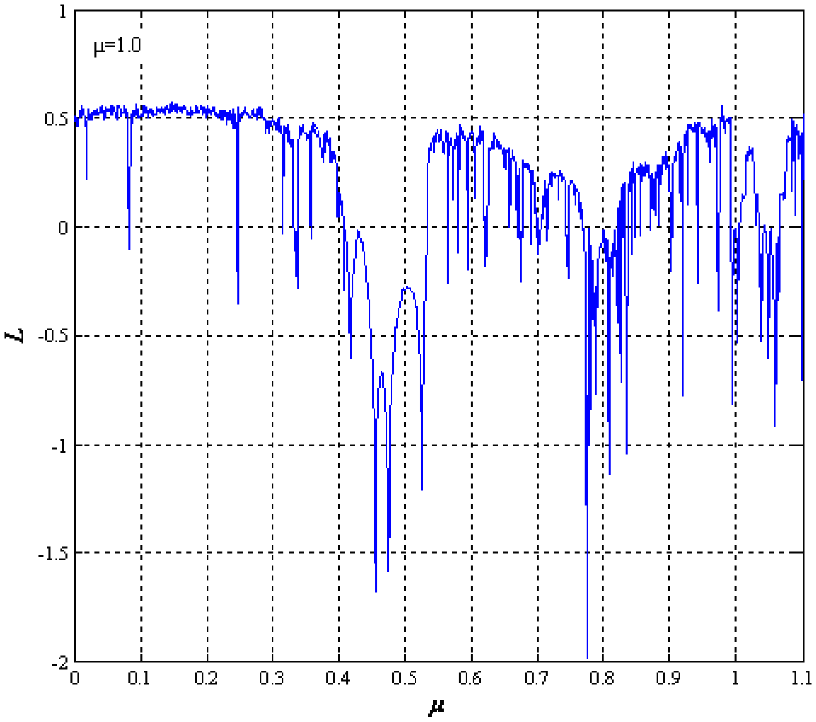

Fig. 6.9 Lyapunov Exponent Diagram for $\mu = 1.0$

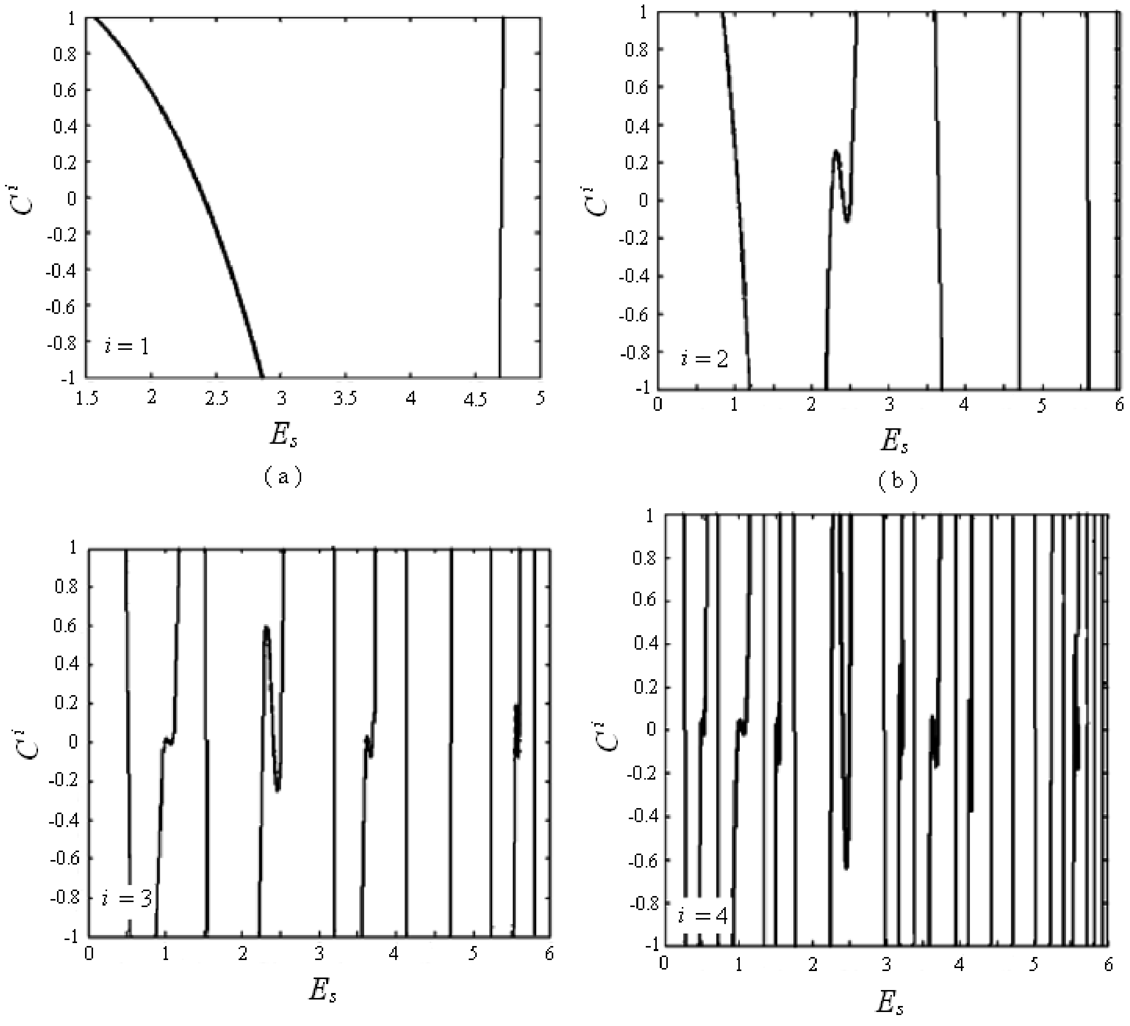

(a) (b)

(c) (d)

Fig. 6.10 Control Curve C^i, $i = 1, 2, 3, 4$, for the Bi-parameter Model with λ=0.7, μ=1.1. The range is restricted to $-1 < C^p(E_s) < 1$ in each case

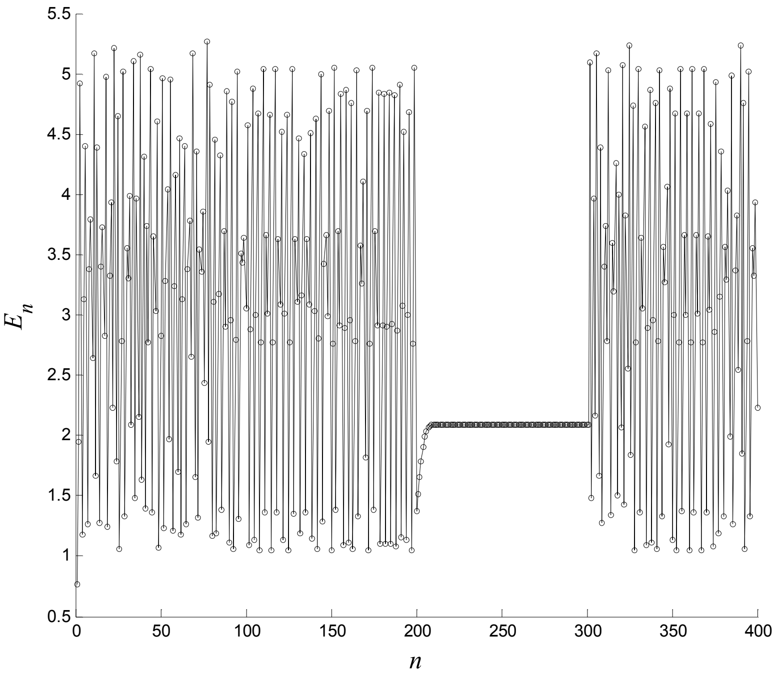

Fig. 6.11 Stabilization of Points of Period One of Bi-parameter Model with λ=0.7, μ=1.1. (E_s=2.0, k=0.410) The control is activated after the 200th iterate and is switched off after the 300th iterate.

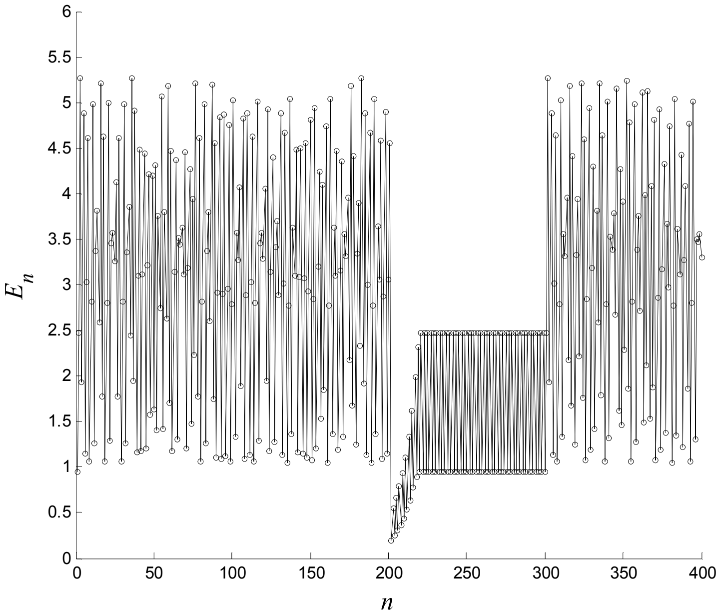

Fig. 6.12 Stabilization of Points of Period Two of Bi-parameter Model with λ=0.7, μ=1.1. (E_s=1.0, k=0.180) The control is activated after the 200th iterate and is switched off after the 300th iterate.

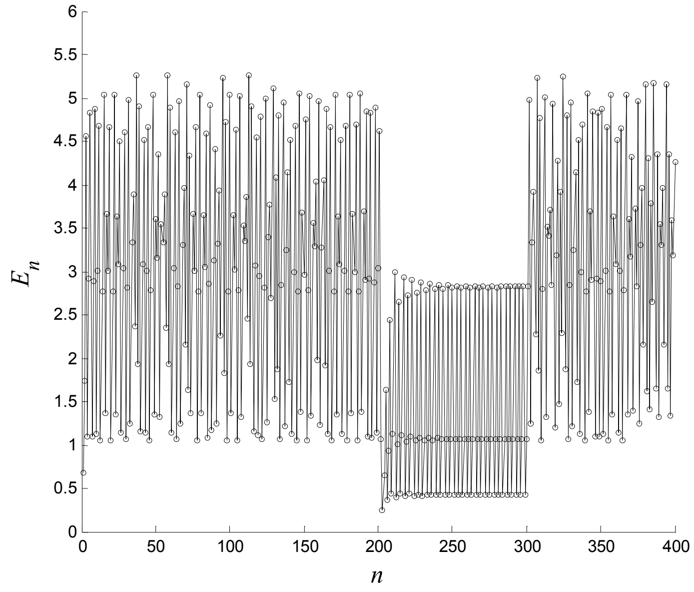

Fig. 6.13 Stabilization of Points of Period Three of Bi-parameter Model with λ=0.7, μ=1.1. (E_s=1.17, k=0.085) The control is activated after the 200th iterate and is switched off after the 300th iterate.

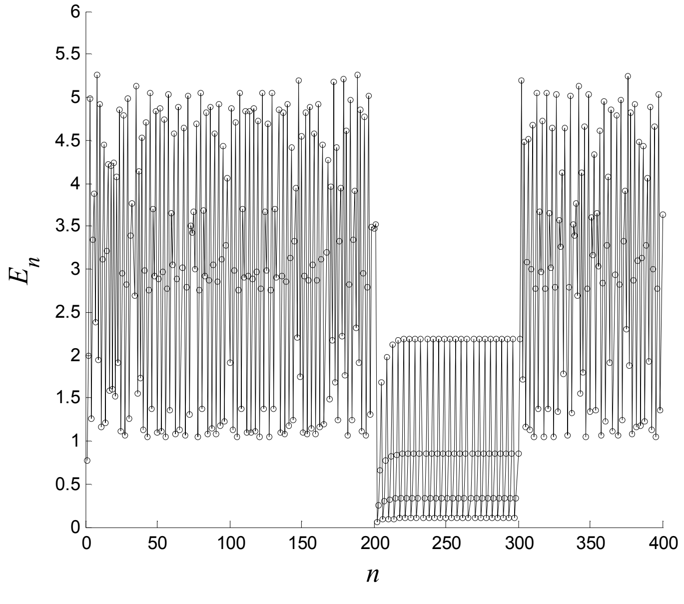

Fig. 6.14 Stabilization of Points of Period Four of Bi-parameter Model with λ=0.7, μ = 1.1. (E_s=3.581, k=0.019) The control is activated after the 200th iterate and is switched off after the 300th iterate.

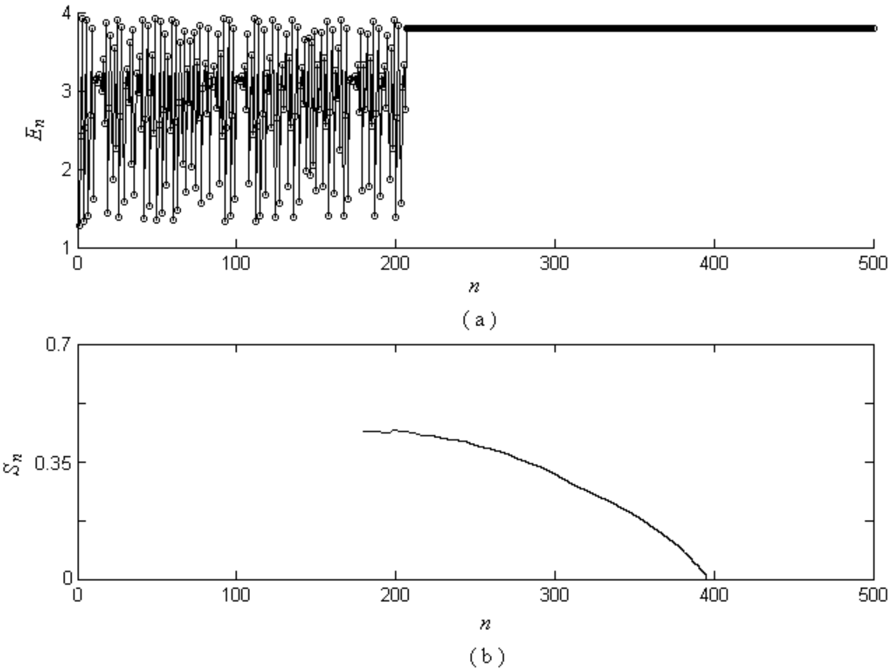

Fig. 6.15 Stabilizing the Fixed Point of the Nonlinear Model of Equation (6.14)

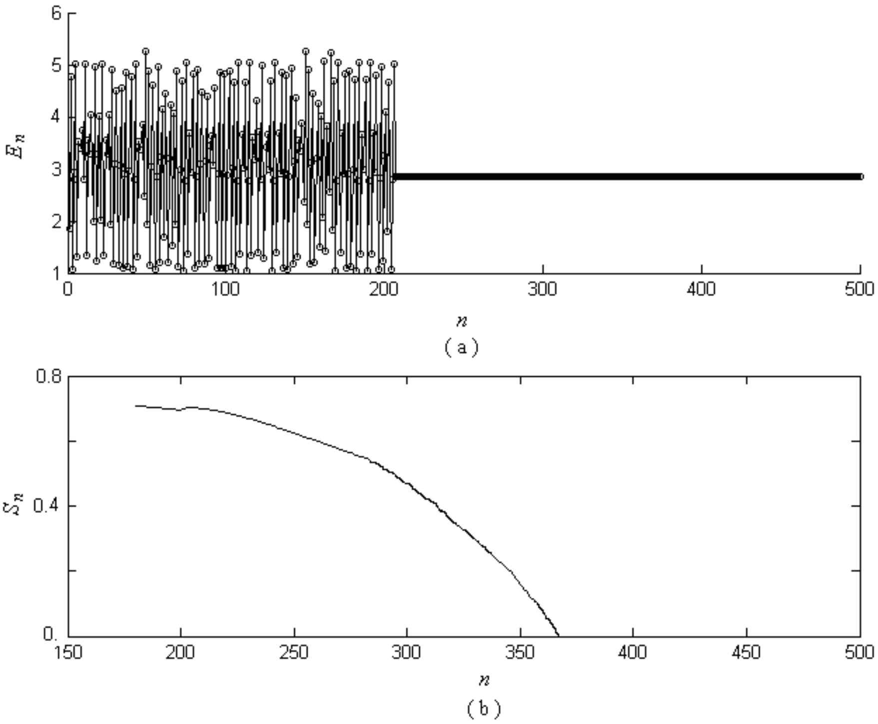

Fig. 6.16 Stabilizing the Fixed Point of the Nonlinear Model of Equation (6.17)

CHAPTER 7

IDENTIFICATION AND CONTROL OF COMBUSTION INSTABILITIES USING NEURAL NETWORKS

7.1 Introduction

In the context of a real gas turbine combustor, the current study in this chapter is primarily dedicated to identifying and predicting combustion dynamics by an artificial neural network (ANN), viz., nonlinear auto-regressive moving average with exogenous input (NARMAX) model, which has in the past been used in a comprehensive manner (Glass and Franchek, 1999). Moreover, based on a nonlinear autoregressive moving average (NARMA-L2) algorithm, a control system is proposed to eliminate the combustion instability in terms of a representative system of interest, which may eventually be extended to practical gas turbine combustors.

7.2 Neural Identification of Combustion Instability

The nonlinear autoregressive moving average with exogenous inputs (NARMAX) model proposed by Chen and Billings (1989), has been adopted to provide a powerful representation for the time series analysis, modelling and prediction owing to its ability to accommodate the dynamic, complex and nonlinear nature of real-world time series prediction problems (Glass, 1999).

$$y(t) = \mathbf{F}\lfloor y(t-1), y(t-1), \ldots, y(t-n_y), x(t-1), x(t-1), \ldots, x(t-n_x)\rfloor \qquad (7.1)$$

where *y*, and *x* are respectively the output and external input for the system model, n_y and n_x are the maximum lags in the output and input, and **F** is an unknown smooth function. Additionally, the output is fed back to the input of the feed forward neural network and consequently, the input to the feed forward network is more accurate.

In terms of training the network, the model receives input vectors and the output is compared with the desired targets corresponding to the inputs. As a result, the weight coefficients associated with the neural network can be recursively updated according to a specific training algorithm. Thus, the function F in Equation (7.1) can be approximated by a neural network, written as,

$$y(t) = \mathbf{NN}\lfloor y(t-1), y(t-1), \ldots, y(t-n_y), x(t-1), x(t-1), \ldots, x(t-n_x)\rfloor \qquad (7.2)$$

If the training of the neural network has been implemented, the model developed could be used to simulate the dynamics of the system of interest.

In this work, the numerical results reported by Steele et al. (2000) are employed to capture the nonlinear behaviour inherent in combustion instability using the neural network developed, where the temporal variations of acoustic pressure were provided in terms of series of cases with different fuel injection locations. For the NARMAX model, a three-layer feed-forward network was developed. The inputs were normalized with respect to the absolute maximums. A sigmoidal transformation was adopted in the second layer. In addition, the lags in the output and input were specified to be 8, which can result in optimal prediction. Figs. 7.1-3 show the comparisons between the numerical results reported by Steele et al. (2000), denoted by circles, and the simulated results obtained by the NARMAX model, denoted by the solid line, respectively. It was found that good agreement between the two is obtained and the nonlinear behaviour and the dynamics associated with the combustion instability can be captured. In addition, in Fig. 7.1, the amplitude of acoustic pressure is being attenuated and the system is stable, whereas Figs. 7.2-3 could potentially indicate that the limit cycles appear due to the coupling of the heat released by the reactions and the acoustics in the combustion chamber. Furthermore, the prediction based on the existing data was implemented for the case with fuel injection location of 7.6 cm and its nonlinear performance could recur. Therefore, the NARMAX model adopted could identify and predict the dynamics of pressure oscillations and, thus, it could be extended to derive a control scheme for the system of interest.

7.3 Neural Dynamic Control of Combustion Instability

Due to the nonlinearities associated with the system under concern, it is relatively difficult to define a control system. In this work, the NARMA-L2 control method proposed by Narendra and Mukhopadhyay (1997) is adopted. The primary basis of the NARMA-L2 controller involves transformation of a nonlinear dynamic system into a linear dynamic system by “appropriate cancellation” of the nonlinearities. Additionally, NARMA-L2 is simply a rearrangement of the neural network for the system to be controlled, which is trained off-line and in a batch form. Firstly, the nonlinear autoregressive moving average (NARMA) is used to represent the general discrete-time nonlinear system as,

$$y(k+d) = N[y(k), y(k-1), \ldots, y(k-n+1), x(k), x(k-1), \ldots, x(k-n+1)] \quad (7.3)$$

where x and y are the system input and output, respectively. If one desires the system output to follow some reference trajectory $y(k+d) = y_r(k+d)$, a nonlinear controller can be developed as,

$$x(k+d) = G[y(k), y(k-1), \ldots, y(k-n+1), y_r(k+d),\ x(k-1), \ldots, x(k-m+1)] \quad (7.4)$$

However, the problem with using this controller is that dynamic back propagation (Hagan et al., 2000) is required to train a neural network to create the function G, which is quite slow. In this regard, an alternative approximate model to represent the system was proposed by Narendra and Mukhopadhyay (1997), given as

$$\begin{aligned} y(k+d) = {} & f[y(k), y(k-1), \ldots, y(k-n+1),\ x(k-1), \ldots, x(k-m+1)] \\ & + g[y(k), y(k-1), \ldots, y(k-n+1),\ x(k-1), \ldots, x(k-m+1)] \cdot x(k) \end{aligned} \quad (7.5)$$

where f and g are functions of only the previous values of the output y. This model is in a suitable form, where the controller input $x(k)$ is not contained inside the nonlinearity. It should be noted that an advantage afforded by this form is that it is possible to solve for the control input that results in the system output to follow the reference y_r. Consequently, the resulting controller can be obtained as

$$u(k+1) = \frac{y_r(k+d) - f[y(k),\ \ldots, y(k-n+1),\ x(k), \ldots, x(k-m+1)]}{g[y(k),\ \ldots, y(k-n+1),\ x(k), \ldots, x(k-m+1)]} \quad (7.6)$$

which is realizable for $d \geq 2$.

In terms of a typical time evolution of acoustic pressures reported by Steele et al. (2000), viz., the case with the fuel injection location of 6.7 cm, a control system is developed as shown in Fig. 7.4. It should be noted that the predictions without the control system shown in Fig. 7.5 highlights the nonlinearity inherent in combustion instability. Initially, linear oscillations appear because the acoustic losses are relatively weak, and then a limit cycle is reached in which nonlinear effects play an important role. Furthermore, the response of the ANN controller developed is also provided in Fig. 7.5. When the control is activated, the amplitude of pressure oscillation is attenuated and eventually reaches an acceptable level.

7.4 Conclusions

In this study, the NARMAX model was used to identify and predict the nonlinear performance associated with combustion instability in terms of the system under investigation. The comparisons for the simulated results with numerical (experimental) results indicate that this model could capture the nonlinear dynamics of the complex system. Moreover, a control system was developed using the NARMA-L2 model and the simulation indicates that the controller is able to suppress the combustion instability effectively. Therefore, the controller developed may be adopted to attenuate the complex interaction between the heat release and the acoustics of combustion chamber in practical gas turbine engines. In particular, the current work in conjunction with Large Eddy Simulation (LES) as reported by Lei and Turan (2010c) may be implemented to control combustion instability in the future work.

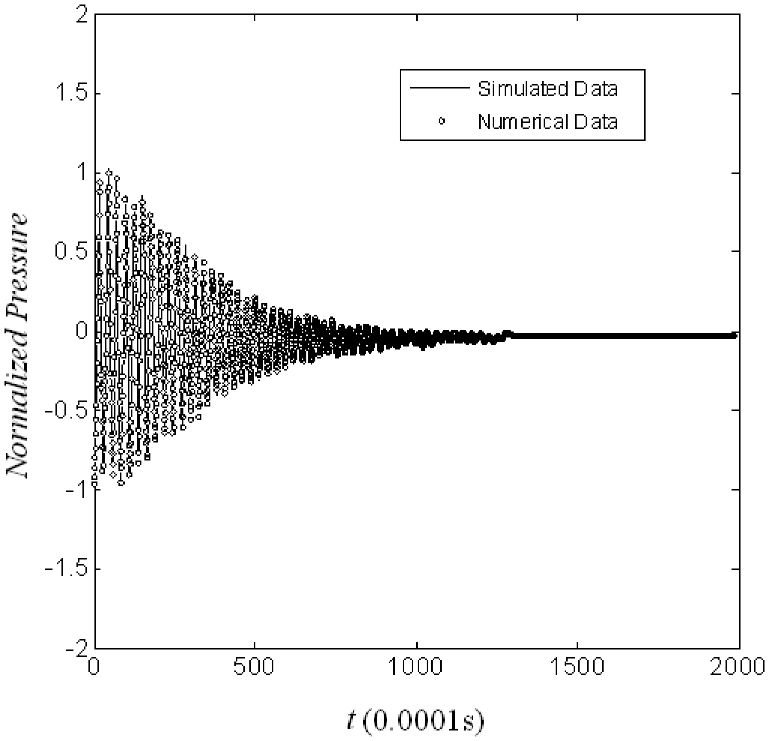

Fig. 7.1 Time History of Pressure at Combustor Mid-Section for Fuel Injection Location of 4.3cm

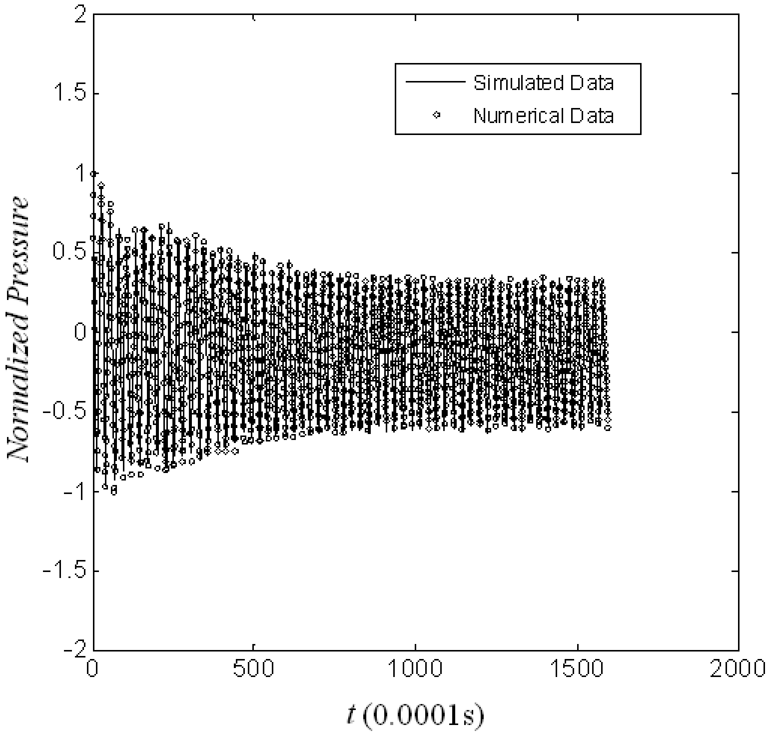

Fig. 7.2 Time History of Pressure at Combustor Mid-Section for Fuel Injection Location of 4.9cm

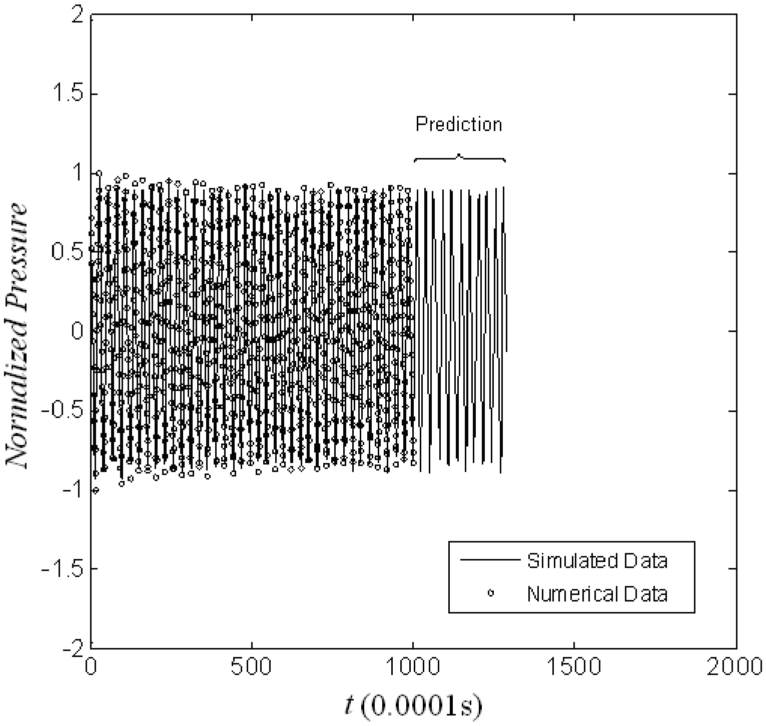

Fig. 7.3 Time History of Pressure at Combustor Mid-Section for Fuel Injection Location of 7.6cm

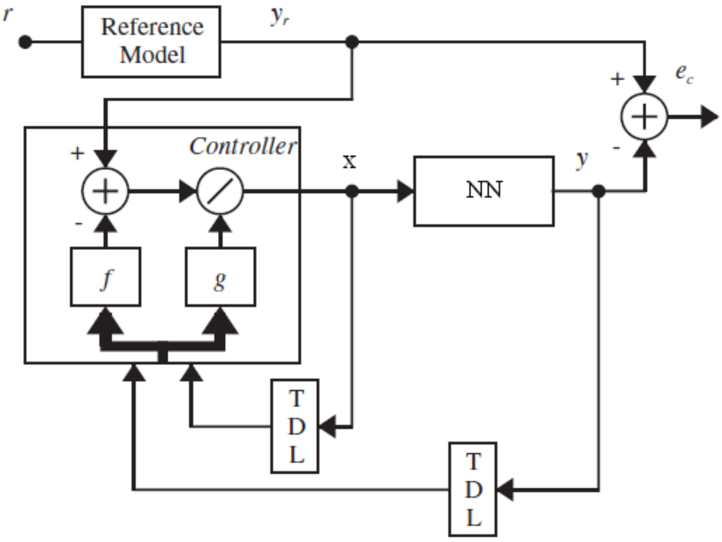

Fig. 7.4 Block Diagram of Applying NARMA-L2

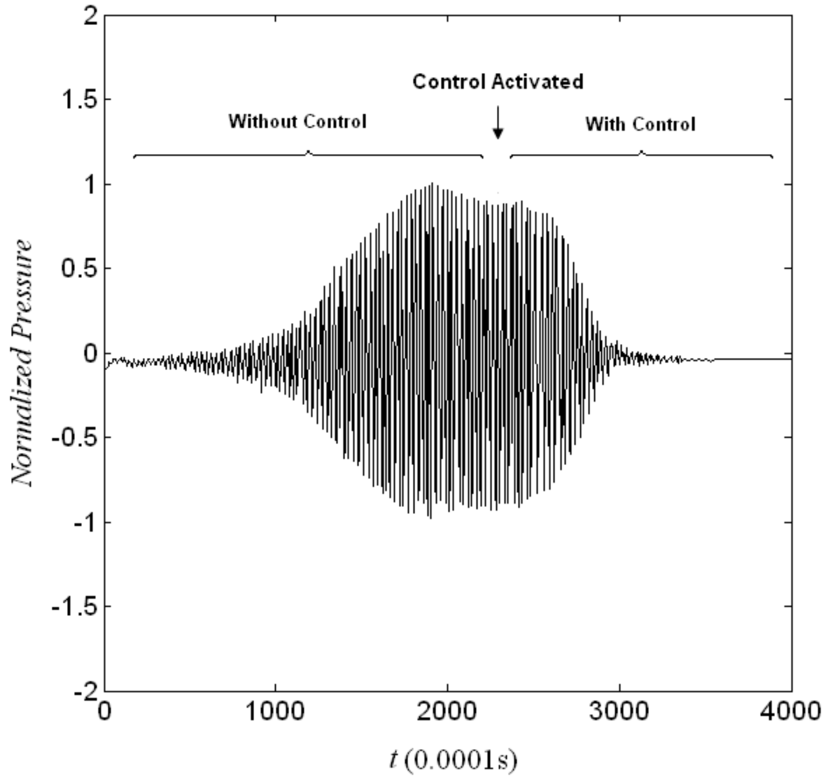

Fig. 7.5 Time History of Pressure at Combustor Mid-Section for Fuel Injection Location of 6.7cm with/without Control

CHAPTER 8

CONCLUSIONS AND FUTURE WORK

The thesis primarily concerns with thermo-acoustic instabilities in liquid fuelled gas turbine combustors and the evaporation process identified as one of the key mechanisms driving thermo-acoustic/combustion instabilities is focussed.

In the first part, numerical methods such as LES have been employed to validate the evaporation of droplets in a realistic gas turbine combustor and good agreement between numerical predictions and experimental data has been obtained. It shows clearly that the current code could capture both the flow behaviour and droplets' characteristics and can thereby be extended to cases of combustion instabilities.

Moreover, a comprehensive method, in which the pressure-velocity-density coupling inherent to the transient evaporation of droplet is taken into consideration, has been developed. A comparative analysis of current numerical predictions and analytical results by hydrodynamic and kinetic methods to the problem under concern has been discussed. It is found out that the hydrodynamic model universally used in computation fluid dynamic (CFD) codes is not suitable for the study of combustion instabilities in liquid-fuelled gas turbine combustors. Additionally, in order to highlight the influence of the practical droplet vaporization process in an unstable combustion environment, the current work is helpful to improve the analytical models in terms of the case of droplet vaporization accounting for both the convective heat transfer and the two-way coupling between vaporization and acoustics.

Furthermore, based on Navier-Stokes equations, two dynamic models have been proposed. In terms of the one-mode dynamic model, which includes a simple harmonic oscillatory behaviour for combustion used in the same manner as that of Sterling (1993), the system exhibits a variety of chaotic behaviours for some select range of the bifurcation parameter. These results are of significance to partially illustrate the emergence of the overshoot zone accompanying the linear zone and the nonlinear limit cycle discovered in pressure trajectory with time. The formulae for the bifurcation parameter and the period at Hopf points have been derived for the two-mode dynamic model. In the range from 0 to -10, the bifurcation parameter and the corresponding period at Hopf points vary rapidly. The limit value of the bifurcation parameter tends to be β, which is one of coefficients in the model. Additionally, it should be noted that the Hopf point computations are important to reveal the bifurcation structure associated with the thermo-acoustic instability in a given system and might result in the occurrence of limit cycle.

In terms of a simplified case, it is found in Equation (5.43) that the coupling and the resulting energy transfer between the acoustic modes are primarily caused by the nonlinear gasdynamics. Additionally, the nonlinear coupling between the acoustic modes can cause an energy cascade and limit cycle consequently occurs. The energy transferred from lower to higher modes results from the terms $\dot{\eta}_i\dot{\eta}_{n-i}$ and $\ddot{\eta}_i\eta_{n-i}$, whereas the terms $\dot{\eta}_i\dot{\eta}_{n+i}$ and $\ddot{\eta}_i\eta_{n+i}$ cause the reverse energy transfer from higher to lower modes.

Considering that combustion occurs unsteadily in a low Mach number flow and consequently the sources owing to combustion and evaporation processes are far larger than the sound resulted from the other source mechanisms, as pointed out by Dowling et al. (1992), discrete dynamic models of the system under consideration are proposed, in which the nonlinearity is associated with the response of the heat release and mass transfer to pressure and/or velocity oscillations. In terms of the first model of delayed combustion response which was originally put forward by Sterling (1993), additional details regarding the nonlinear dynamic performance have been explored. The transformation between a limit cycle, periodic motion and chaos is highlighted. Furthermore, the Feigenbaum constant has been calculated, to be in line with the universally reported value. In addition, the Lyapunov exponent has been obtained and it is found out that for $0<\mu<0.85$, the system is, in general, stable. This exponent may be used to capture the stability of the system of interest numerically and experimentally. Moreover, the more complicated dynamic model which accounts for both the combustion and evaporation processes has been developed. The bifurcation diagrams show that the mass addition can greatly influence the occurrence of bifurcation points and the amplitude of oscillation. For the case of varying λ and $\mu = 1.0$, initially chaotic behaviour arises, reflecting that, under certain circumstances, the vaporization of droplets will strengthen the heat release to drive the combustion instability. Additionally, the Lyapunov exponent calculated may point to the fact that that the chaotic range extent may increase in the presence of the vaporization process.

Finally, the control algorithms including the OGY method and minimum eentropy method are employed to control the chaotic performance of the system. The performance controlled indicates that these methods can be complemented either numerically or experimentally to control the prevailing thermo-acoustic/combustion instability. In addition, the nonlinear behaviours associated with thermo-acoustic instability in terms of the system under investigation have been identified and predicted using the state of the art neural networks and the corresponding controller developed may be adopted to attenuate the interaction between heat released by reactions and the acoustics of combustion chamber in practical gas turbine engines.

In the future, since the mechanisms inducing thermo-acoustic instability primarily result from the interaction of heat release and chamber acoustics, it is of extreme importance to optimize the distribution of heat release in the combustion chamber for non-premixed/premixed gas turbine combustors. Furthermore, more advanced evaporation model oriented to numerically simulating combustion instability will be developed, which can capture the two-way coupling between the vaporization and acoustic fields. Moreover, LES in conjunction with the advanced model discussed above and appropriate boundary conditions such as NSCBC (Navier-Stokes characteristic boundary condition) will be operated in order to indentify the energy transition between acoustic modes and heat release.

APPENDIX A

NUMERICAL METHODS

In this appendix, the numerical methods employed in Chapter 3 including temporal discretization, spatial discretization and pressure-velocity coupling are provided in detail.

AA.1 Gas Phase

The control-volume-based technique is employed in the code, FLUENT, to obtain algebraic equations which can be solved numerically. This technique yields discrete equations satisfying the conservation law on a control volume basis through integrating the transport equations.

In terms of a dependent variable denoted by ϕ, the general transport equation may be written as

$$\frac{\partial}{\partial t}(\rho\phi)+\mathbf{div}(\rho\mathbf{u}\phi)=\mathbf{div}(\Gamma_\phi \mathbf{grad}\phi)+S_\phi \qquad \text{(AA.1)}$$

where ρ is the density, **u** is the velocity vector, Γ_ϕ is the diffusion coefficient and S_ϕ is the source term. Integration of Equation (AA.1) over an arbitrary control volume, *V*, leads to

$$\int_V \frac{\partial}{\partial}(\rho\phi)+\oint \rho\mathbf{u}\phi\cdot d\mathbf{A}=\oint \Gamma_\phi \nabla\phi\cdot d\mathbf{A}+\int_V S_\phi d\mathbf{A} \qquad \text{(AA.2)}$$

in which **A** is the surface area vector. Discretizing Equation (AA.2) on a given cell, one may obtain

$$\frac{\partial}{\partial t}(\rho\phi)\cdot V+\sum_f^{N_{face}}\rho_f \mathbf{u_f}\phi_f\cdot \mathbf{A}_f=\sum_f^{N_{face}}\Gamma_{\phi,f}\nabla\phi_f\cdot\mathbf{A}_f+S_\phi\cdot V \qquad \text{(AA.3)}$$

where N_{face} is the number of faces enclosing cell, $\mathbf{A}_f$ is the area of face *f*, ϕ_f is the value of ϕ convected through face *f*, $\rho_f \mathbf{u_f}\phi_f\cdot\mathbf{A}_f$ is the mass flux through the face f and $\nabla\phi_f$ is the gradient of ϕ at face *f*. Note that the first and second terms on the left side of Equation (AA.3) represent the unsteady and convection ones, respectively, while the first and second terms on the right side denote the diffusion and source ones, respectively. The techniques to numerically express these terms will be discussed in the following sections.

AA.1.1 Temporal Discretization

Considering that the nature of LES simulations is unsteady, a temporal discretization must be implemented for the governing equations. In terms of Equation (AA.3), each terms should be integrated over a time step Δt. A generic expression for the time solution of a variable ϕ can be written as

$$\frac{\partial \phi}{\partial t} = F(\phi) \tag{AA.4}$$

where F represents any spatial discretization with respect to ϕ. Provided that the time derivative is discretized using backward differences, one can obtain the first-order temporal discretization written as

$$\frac{\phi^{n+1} - \phi^{n}}{\Delta t} = F(\phi) \tag{AA.5}$$

and the second-order discretization is given by

$$\frac{3\phi^{n+1} - 4\phi^{n} + \phi^{n-1}}{2\Delta t} = F(\phi) \tag{AA.6}$$

where *n*, *n*+1 and *n*-1 denote the time step at *t*, *t+Δt*, *t-Δt*, respectively.

If $F(\phi)$ is evaluated at the future time level *n*+1, the implicit time integration can be achieved. Thus, the first-order implicit scheme can be obtained from Equation (AA.5)

$$\phi^{n+1} = \phi^{n} + \Delta t \cdot F\left(\phi^{n+1}\right) \tag{AA.7}$$

and, similarly, the second-order implicit scheme derived from Equation (AA.6) is written by

$$\phi^{n+1} = \frac{4}{3}\phi^{n} - \frac{1}{3}\phi^{n-1} + \frac{2}{3}\Delta t \cdot F\left(\phi^{n+1}\right) \tag{AA.8}$$

Note that this implicit scheme is unconditionally stable with respect to time step size. However, the time step size for LES should be appropriately chosen to satisfy that the physical time step size is smaller than the time scale of smallest resolved eddies. In this sense, the *CFL* (Courant-Friedrichs-Lewy) number proposed by Courant et al. (1967) should be kept around 1, given as

$$CFL = \max\left(\frac{u\Delta t}{\Delta x}, \frac{v\Delta t}{\Delta y}, \frac{w\Delta t}{\Delta z}\right)$$

In this work, the first-order implicit scheme is used for RANS simulations which provides the initial conditions for LES, whereas the second-order implicit scheme is employed for LES simulations.

AA.1.2 Spatial Discretization

In the current code, a collocated grid approach is employed, where the values of the scalar ϕ are stored at the cell centres and the face values ϕ_f are obtained through interpolating the cell values for the convection terms in Equation (AA.3). In addition, an upwind scheme is used for RANS, whereas the central-differencing scheme is employed for LES to achieve higher-order accuracy with lower numerical dissipation and diffusion.

Since the initial conditions for LES do not require a rigorously accurate solution, just first/second order upwind schemes are used to generate the initial filed for LES. In terms of the first order upwind scheme, face values are identical to cell values. Thus, the face values ϕ_f are set to be equal to the upstream cell values. In the second-order upwind scheme (SOU), the values of a variable at cell are calculated by a multidimensional linear reconstruction approach developed by Barth and Jespersen (1989). The face value ϕ_f is obtained by

$$\phi_{f,SOU} = \phi + \nabla\phi \cdot \mathbf{r} \tag{AA.9}$$

where ϕ and $\nabla\phi$ are the cell-centred value and its gradient in the upwind cell and $\mathbf{r}$ is the displacement vector from the upstream cell centroid to the face centroid, as shown in Fig. AA.1.

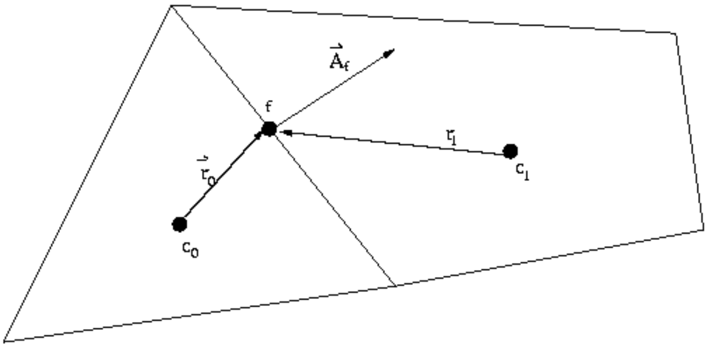

Fig. AA.1 Control Volume for a Scalar Transport Equation

As upwind schemes are relatively dissipative, central differencing schemes are preferred. Nevertheless, these schemes may lead to unphysical wiggles in the solution and consequently result in numerical instabilities. To avoid this problem, the central differencing schemes are generally blended with upwind schemes. For the pure central-differencing (CD) scheme, the face value of a scalar ϕ_f is computed by

$$\phi_{f,CD} = \frac{1}{2}(\phi_0 + \phi_1) + \frac{1}{2}(\nabla\phi_{r,0} \cdot \mathbf{r}_0 + \nabla\phi_{r,1} \cdot \mathbf{r}_1) \qquad \text{(AA.10)}$$

in which the subscripts 0 and 1 refer to the cells sharing face *f*, respectively; $\nabla\phi_{r,0}$ and $\nabla\phi_{r,1}$ are the reconstruction gradients at the cells 0 and 1, respectively. Note that this scheme may very often lead to unphysical fluctuation numerically, as mentioned above. To eliminate these wiggles, in this work, a second-order scheme based on the original MUSCL scheme (Monotone Upstream-Centred Schemes for Conservation Laws) of van Leer (1979) is implemented. It combines both a central differencing scheme and second-order upwind scheme (SOU) and may be written as

$$\phi_f = \theta\phi_{f,CD} + (1-\theta)\phi_{f,SOU} \tag{AA.11}$$

where $\phi_{f,CD}$ is calculated by Equation (AA.10) and $\phi_{f,SOU}$ is calculated using Equation (AA.9). Note that this scheme may be applicable for structured/unstructured meshes.

AA.1.3 Calculation of Gradients

Gradients are also required to numerically calculate secondary diffusion terms and velocity derivatives in Equation (AA.3). In the current code, the Green-Gauss theorem is implemented to obtain the gradient of the scalar ϕ by

$$\nabla\phi = \frac{1}{V}\sum_{f}^{N_{face}} \bar{\phi}_f \cdot \mathbf{A}_f \tag{AA.12}$$

where the face value ϕ_f is calculated using the arithmetic average of the values at the neighbouring cell centres,

$$\bar{\phi}_f = \frac{1}{2}(\phi_0 + \phi_1) \tag{AA.13}$$

or, alternatively, may be obtained by

$$\bar{\phi}_f = \frac{1}{N_f}\sum_{n}^{N_f} \bar{\phi}_n \tag{AA.14}$$

where N_f is the number of nodes on the face and $\bar{\phi}_n$ is the nodal values constructed from the weighted average of the cell values enclosing the nodes according to the approached proposed by Rauch et al. (1991) and Holmes and Connel (1989). Note that this scheme preserves a second-order spatial accuracy.

AA.1.4 Linearization

Considering an arbitrary cell (denoted by *P*), the linearization equation of Equation (AA.3) may be accomplished using the temporal and spatial discretization schemes discussed above with respect to the unknown variables at the cell and its surrounding neighbouring cells, written as

$$a_P \phi_P = \sum_{nb} a_{nb} \phi_{nb} + b \tag{AA.15}$$

where the index *nb* indicates the neighbouring cells; a_p and a_{nb} are the linearized coefficients for the cell variable ϕ_P and the neighbouring cell variables ϕ_{nb} , respectively; *b* represents the source term generated by the numerical manipulations and/or physical processes. Thus, a set of algebraic equations with a coefficient matrix is constructed applying the linearization procedure over every cell in the computational domain. Moreover, the numerical solution of Equation (AA.3) may be obtained by solving the coefficient matrix using a point implicit Gauss-Seidel solver.

AA.1.5 Pressure-Velocity Coupling

To simultaneously satisfy the mass and momentum conservations, the pressure-velocity coupling should be implemented. In this current code, the SIMPLE family of algorithms including SIMPLE, SIMPLEC and PISO based on a typical predictor-corrector process, are employed.

In SIMPLE algorithm, the correlation of velocity with pressure correction is used to enforce mass conservation and then achieve the pressure field. Provided that a guessed pressure field p^* is taken to solve the momentum equation, the face flux J_f^* resulted from the continuity equation, which might not satisfy mass conservation, is written as

$$J_f^* = \hat{J}_f^* + d_f\left(p_{c0}^* - p_{c1}^*\right) \tag{AA.16}$$

where $\hat{J}_f$ accounts for the effects of the velocity in cells and d_f is a function a_p in the discretized continuity equation. If the mass conservation is not satisfied, a correction J'_f is required to compensate the face flux J_f^*. Consequently, one can obtain the corrected face flux J_f to satisfy the continuity equation, written as

$$J_f = J_f^* + J'_f \tag{AA.17}$$

where

$$J'_f = d_f\left(p'_{c0} - p'_{c1}\right) \tag{AA.18}$$

in which p'_{c0} and p'_{c1} are the cell pressure corrections at the cells denoted 0 and 1 shown in Fig. AA.1, respectively. In the SIMPLE algorithm, the substitution of the flux correction equation, both Equation (AA.17) and Equation (AA.18), into the discrete continuity equation leads to a discrete equation for the pressure correction p' for a certain cell as

$$a_P p' = \sum_{nb} a_{nb} p'_{nb} + b \tag{AA.19}$$

where the source term b is the sum of flow rate in the cell, written as

$$b = \sum_{f}^{N_{faces}} J_f^* \mathbf{A}_f \tag{AA.20}$$

The solution of the pressure correction equation, Equation (AA.19), yields the corrected pressure and face flux, given as

$$p = p^{*} + \alpha_{P} p' \qquad \text{(AA.21)}$$

$$J_f = J_f'^{*} + d_f \left(p'_{c0} - p'_{c1} \right) \qquad \text{(AA.22)}$$

where α_P is the under-relaxation factor for the pressure. Note that corrected face flux, J_f, satisfies the discrete continuity equation identically.

In the past, considerable variants of the basic SIMPLE algorithm have been developed, while in this work, the SIMPLEC (SIMPLEC-Consistent) algorithm proposed by Van Doormaal and Raithby (1984) is employed in that it may accelerate convergence in cases of pressure-velocity coupling playing an important role. The SIMPLEC procedure is similar to the SIMPLE procedure outlined above. The only difference is that the coefficient d_f in Equation (AA.17) is defined as a function $\overline{a_P - \sum_{nb} a_{nb}}$ instead of just $\overline{a_P}$.

AA.2 Liquid Phase

Appropriate numerical algorithms are also employed to obtain the trajectory of droplets by solving Equation (3.28) and Equation (3.29). In this work, an automated switch technique between lower-order scheme and higher-order one is used to achieve numerical stability and/or higher accuracy. Implicit Euler algorithm is adopted for the lower-order scheme, which is unconditionally stable, whereas in terms of the higer-order scheme, a 5th order Runge-Kutta scheme developed by Cash and Karp (1990) is implemented, which could provide higher accuracy, however is stable just in a limited range.

APPENDIX B

SUMMARY OF THE EQUATIONS USED FOR CALCULATING PHYSICAL PROPERTIES

AB.1 Density

Density ρ was calculated using the equation of state of an ideal gas,

$$\rho = \frac{p}{R_g T \sum_{i=1}^{N} \left(Y_i / M_i \right)}, \text{ kg/m}^3 \qquad \text{(AB.1)}$$

where R_g is universal gas constant, Y_i is mass fraction of *i*-th species and M_i is molecular weight of *i*-th species.

AB.2 Specific Heat

The formula used specific heat at constant pressure, $C_{p,i}$, reads

$$C_{p,i} = \left(a_0 + a_1 \cdot T + a_2 \cdot T^2 + a_3 \cdot T^3 + a_4 \cdot T^4\right) / M_i \text{ ,J/kg-K} \qquad \text{(AB.2)}$$

where a_0, a_1, a_2, a_3 and a_4 denote the constants. The values of these constants for gaseous species and isopropyl alcohol vapour are presented in Table AB.1.

Table AB.1 Constants in Equation (AB.2) for $C_{p,i}$

	a_0	a_1	a_2	a_3	a_4
Isopropyl Alcohol	2.5535×10^{4}	2.1203×10^{2}	5.3492×10^{-2}	-1.473×10^{-4}	4.9406×10^{-8}
O_2	2.811×10^{4}	-3.680×10^{-3}	1.746×10^{-2}	-1.065×10^{-5}	0
CO_2	1.980×10^{4}	7.344×10^{1}	-5.602×10^{-2}	1.715×10^{-5}	0
H_2O	3.224×10^{4}	1.924×10^{0}	1.005×10^{-2}	-3.596×10^{-6}	0
N_2	3.115×10^{4}	-1.357×10^{1}	2.680×10^{-2}	-1.168×10^{-5}	0

AB.3 Diffusion Coefficient

Wilke's correlation (Reid, Prausnitz and Poling, 1987) is used to calculate the diffusion coefficient, D_i,

$$D_{i,m} = \frac{(1 - X_i)^{-1}}{\sum\limits_{\substack{j=1 \\ j \neq i}}^{N} \frac{X_i}{D_{ij}}} \text{, m}^2\text{/s} \qquad \text{(A2-3)}$$

where X_i is mole fraction of i-th species and D_{ij} is the binary diffusion coefficient that was calculated using Fuller's correlation (Reid, Prausnitz and Poling, 1987) given as,

$$D_{ij} = \frac{0.143\times10^{-6} T^{7/4}}{p^* \sqrt{M_{ij}} \left[(\Sigma_v)_i^{1/3} + (\Sigma_v)_j^{1/3}\right]^2} \text{, m}^2\text{/s}$$

where $M_{ij} = 2[(1/M_i)+ (1/M_j)]^2$, M_i, M_j are molecular weight (g/mol) of species i and j, respectively; p^* is pressure (bar); Σ_v is found for each component by summing atomic diffusion volumes.

AB.4 Thermal Conductivity

Thermal conductivity of the gaseous mixture, k, was calculated by Wassiljewa's equation (Reid, Prausnitz and Poling, 1987) given as,

$$k = \sum_{i=1}^{N} \frac{X_i k_i}{\sum_{j=1}^{N} X_j A_{ij}} \text{, W/m-K} \tag{AB.4}$$

where k_i is thermal conductivity of i-th species; X_i and X_j are mole fraction of i-th and j-th species, respectively; and A_{ij} can be calculated using Lindsay and Bromley correlation (Lindsay and Bromley, 1950) given as

$$A_{ij} = \frac{1}{4}\left[1 + \sqrt{\frac{\mu_i}{\mu_j}\left(\frac{M_j}{M_i}\right)^{3/4} \frac{T+S_i}{T+S_j}}\right]^2 \cdot \frac{T+S_{ij}}{T+S_j}$$

where μ_i and μ_j are viscosity of i-th and j-th species, respectively; S_i, S_j, and S_{ij} are Sutherland constants given by

$$S_i = 1.5T_{b,i}$$

$$S_{ij} = \left(S_i S_j\right)^{\frac{1}{2}}$$

in which $T_{b,i}$ is boiling point of i-th species.

AB.5 Latent Heat of Evaporation

The latent heat of evaporation, $L(T_s)$, is calculated by

$$L(T) = 58.982 \times 10^6 \cdot \frac{\left(1 - \dfrac{T}{508.31}\right)^{0.326}}{M}, \text{ J/kg} \tag{AB.5}$$

where M is molecular weight of liquid fuel.

AB.6 Viscosity

The viscosity of gaseous mixture was calculated by (Reid, Prausnitz and Poling, 1987)

$$\mu = \sum_{i=1}^{N} \frac{X_i \mu_i}{\sum\limits_{j=1}^{N} X_j \Phi_{ij}}, \text{ Pa-s} \tag{AB.6}$$

where X_i and X_j are mole fraction of i-th and j-th species, respectively; and Φ_{ij} can be calculated using Wilke's approximation

$$\Phi_{ij} = \frac{\left[1 + \left(\dfrac{\mu_i}{\mu_j}\right)^{\frac{1}{2}} \cdot \left(\dfrac{M_j}{M_i}\right)^{\frac{1}{4}}\right]^2}{2\sqrt{2\left(1 + \dfrac{M_i}{M_j}\right)}}$$

APPENDIX C

ABSTRACTS OF JOURNAL PAPERS

In this appendix, the titles and abstracts of journal papers published/produced during the PhD research are provided.

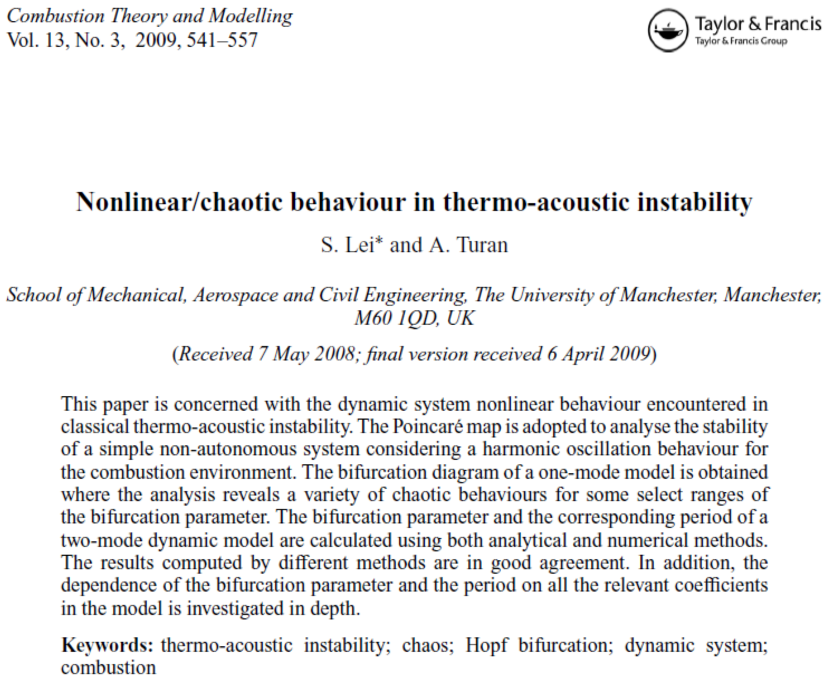

Combustion Theory and Modelling
Vol. 13, No. 3, 2009, 541–557

Nonlinear/chaotic behaviour in thermo-acoustic instability

S. Lei* and A. Turan

School of Mechanical, Aerospace and Civil Engineering, The University of Manchester, Manchester, M60 1QD, UK

(*Received 7 May 2008; final version received 6 April 2009*)

This paper is concerned with the dynamic system nonlinear behaviour encountered in classical thermo-acoustic instability. The Poincaré map is adopted to analyse the stability of a simple non-autonomous system considering a harmonic oscillation behaviour for the combustion environment. The bifurcation diagram of a one-mode model is obtained where the analysis reveals a variety of chaotic behaviours for some select ranges of the bifurcation parameter. The bifurcation parameter and the corresponding period of a two-mode dynamic model are calculated using both analytical and numerical methods. The results computed by different methods are in good agreement. In addition, the dependence of the bifurcation parameter and the period on all the relevant coefficients in the model is investigated in depth.

Keywords: thermo-acoustic instability; chaos; Hopf bifurcation; dynamic system; combustion

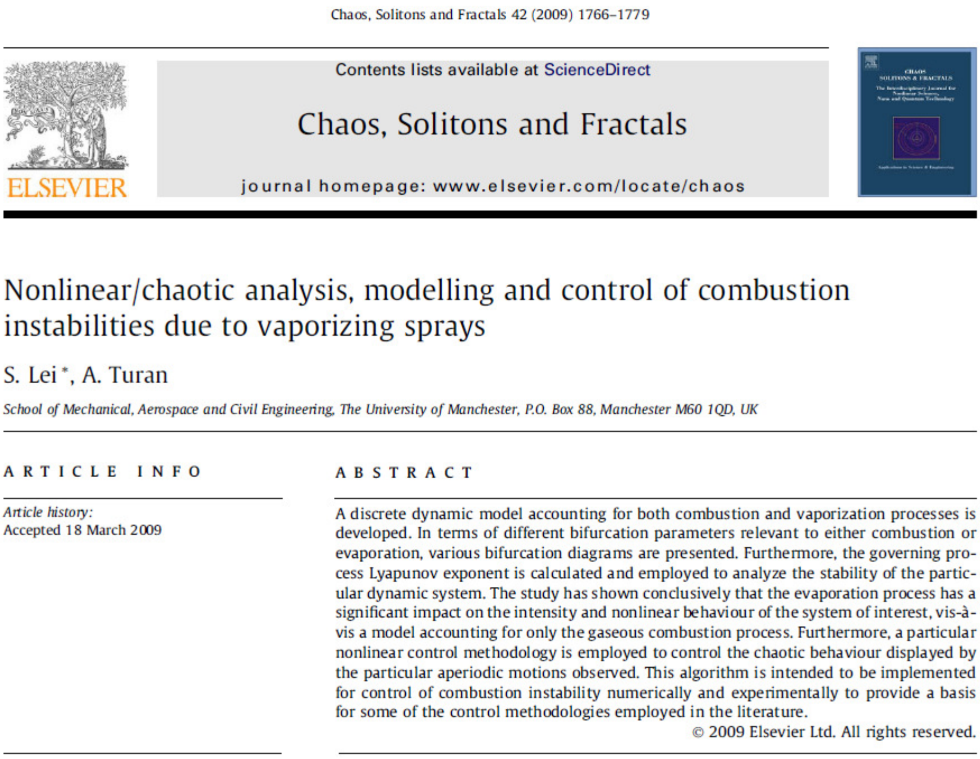

Chaos, Solitons and Fractals 42 (2009) 1766–1779

Contents lists available at ScienceDirect

Chaos, Solitons and Fractals

journal homepage: www.elsevier.com/locate/chaos

Nonlinear/chaotic analysis, modelling and control of combustion instabilities due to vaporizing sprays

S. Lei *, A. Turan

School of Mechanical, Aerospace and Civil Engineering, The University of Manchester, P.O. Box 88, Manchester M60 1QD, UK

ARTICLE INFO

Article history:
Accepted 18 March 2009

ABSTRACT

A discrete dynamic model accounting for both combustion and vaporization processes is developed. In terms of different bifurcation parameters relevant to either combustion or evaporation, various bifurcation diagrams are presented. Furthermore, the governing process Lyapunov exponent is calculated and employed to analyze the stability of the particular dynamic system. The study has shown conclusively that the evaporation process has a significant impact on the intensity and nonlinear behaviour of the system of interest, vis-à-vis a model accounting for only the gaseous combustion process. Furthermore, a particular nonlinear control methodology is employed to control the chaotic behaviour displayed by the particular aperiodic motions observed. This algorithm is intended to be implemented for control of combustion instability numerically and experimentally to provide a basis for some of the control methodologies employed in the literature.

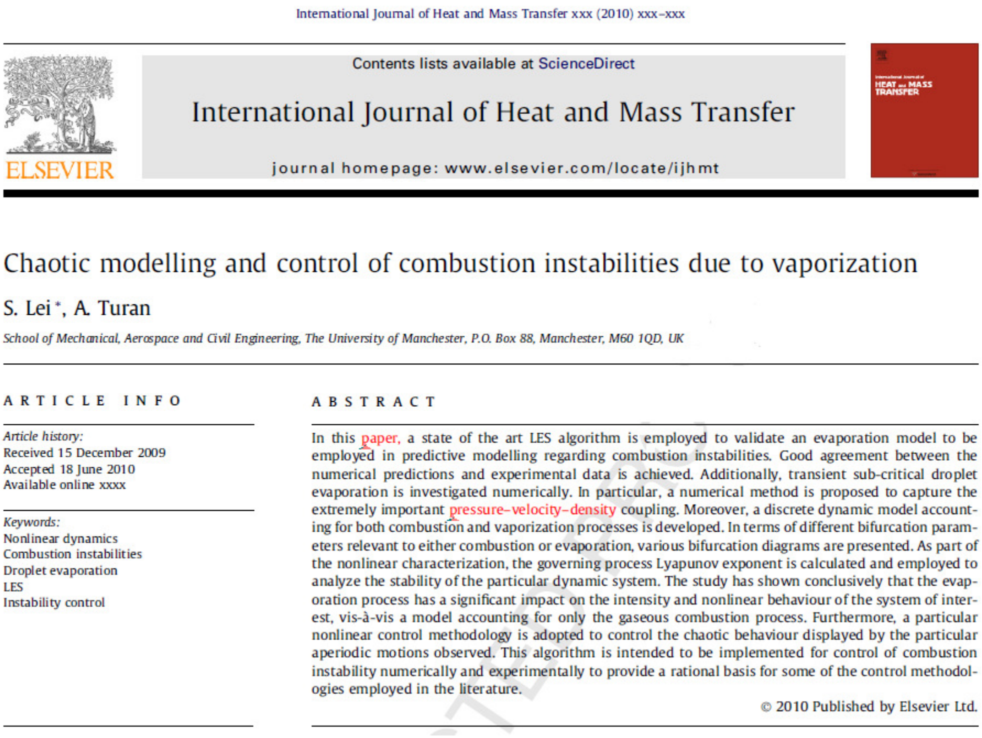

International Journal of Heat and Mass Transfer xxx (2010) xxx–xxx

Contents lists available at ScienceDirect

International Journal of Heat and Mass Transfer

journal homepage: www.elsevier.com/locate/ijhmt

Chaotic modelling and control of combustion instabilities due to vaporization

S. Lei *, A. Turan

School of Mechanical, Aerospace and Civil Engineering, The University of Manchester, P.O. Box 88, Manchester, M60 1QD, UK

ARTICLE INFO

Article history:
Received 15 December 2009
Accepted 18 June 2010
Available online xxxx

Keywords:
Nonlinear dynamics
Combustion instabilities
Droplet evaporation
LES
Instability control

ABSTRACT

In this paper, a state of the art LES algorithm is employed to validate an evaporation model to be employed in predictive modelling regarding combustion instabilities. Good agreement between the numerical predictions and experimental data is achieved. Additionally, transient sub-critical droplet evaporation is investigated numerically. In particular, a numerical method is proposed to capture the extremely important pressure–velocity–density coupling. Moreover, a discrete dynamic model accounting for both combustion and vaporization processes is developed. In terms of different bifurcation parameters relevant to either combustion or evaporation, various bifurcation diagrams are presented. As part of the nonlinear characterization, the governing process Lyapunov exponent is calculated and employed to analyze the stability of the particular dynamic system. The study has shown conclusively that the evaporation process has a significant impact on the intensity and nonlinear behaviour of the system of interest, vis-à-vis a model accounting for only the gaseous combustion process. Furthermore, a particular nonlinear control methodology is adopted to control the chaotic behaviour displayed by the particular aperiodic motions observed. This algorithm is intended to be implemented for control of combustion instability numerically and experimentally to provide a rational basis for some of the control methodologies employed in the literature.

Note that this paper with DOI: 10.1016/j.ijheatmasstransfer.2010.06.045 in *International Journal of Heat and Mass Transfer* is in print.

Identification and Control of Combustion Instabilities Using Neural Networks

S. LEI and A. TURAN

School of Mechanical, Aerospace and Civil Engineering, The University of Manchester,
P.O. Box 88, Manchester, M60 1QD, UK

Abstract– In this paper a state of the art neural network is employed to identify and predict the nonlinear behaviour inherent in combustion instability, and control the ensuing pressure oscillations. Essentially, the NARMAX model is implemented to capture nonlinear dynamics relating the input and output of the system of interest. The simulated results accord with the results reported. Moreover, a control system using the NARMA-L2 algorithm is developed. The simulation conclusively points to the fact that the amplitude of pressure oscillations can be attenuated to an acceptable level and the controller proposed may be implemented in a practical manner.

Key words: Neural Network, Combustion Instabilities, Instability Control, Gas Turbine Combustor

Note that this paper was submited to *AIAA Journal*.

International Journal of Bifurcation and Chaos, Vol. 20, No. 4 (2010) 1–10

DOI: 10.1142/S0218127410026447

NONLINEAR/CHAOTIC MODELING AND CONTROL OF COMBUSTION INSTABILITIES

S. LEI and A. TURAN
School of Mechanical, Aerospace and Civil Engineering,
The University of Manchester, P.O. Box 88,
Manchester, M60 1QD, UK

Received July 10, 2009; Revised September 2, 2009

A discrete dynamic model accounting for both combustion and vaporization processes is proposed. In terms of different bifurcation parameters relevant to either combustion or evaporation, various bifurcation diagrams are presented. Furthermore, the corresponding Lyapunov exponent is calculated and employed to analyze the stability of the particular dynamic system. The study indicates conclusively that the evaporation process has a significant impact on the intensity and nonlinear behavior of the system of interest, *vis-à-vis* a model accounting for only the gaseous combustion process. Moreover, a minimum entropy control method is employed to control the chaotic behavior inherent to the system of interest. This algorithm is intended to be implemented for control of combustion instability numerically and experimentally to provide a basis for some of the control methodologies employed in the literature.

BIBLIOGRAPHY

Abramzon, B. and Sirignano, W.A., 1989, “Droplet Vaporization Model for Spray Combustion Calculations,” Int. J. Heat Mass Transfer, **32**(9), pp. 1605-1618.

Ananthkrishnan, N., Deo, S. and Culick, F. E. C., 2005, “Reduced-order Modelling and Dynamics of Nonlinear Acoustic Waves in a Combustion Chamber,” Combust. Sci. Technol., **177**, pp. 221-248.

Angelberger, C., Veynante, D. and Egolfopoulos, F., 2000, “LES of Chemical and Acoustic Forcing of a Premixed Dump Combustor,” Flow Turbul. Combust., **65**, pp. 205-222.

Apte, S. V.. Gorokhovski, M. and Moin, P., 2003, “LES of Atomizing Spray with Stochastic Modeling of Secondary Breakup,” Int. J. Mdtiphase Flow, **29**, pp.1503-1522.

Barth, J. Ferzier, J. H. and Reynolds, W. C., 1989, “The Design and Application of Upwind Schems on Unstructured Meshes,” Technical Report AIAA-89-0366, AIAA 27th Aerospace Science Meeting, Reno, Nevada, USA.

Baum, J. D. and Levine, J. N., 1982, “Numerical Techniques for Solving Nonlinear Instability Problems in Solid Rocket Motors,” AIAA J., **20**(7), pp. 955-961.

Baum, J. D., Lovine, R. L. and Levine, J. N., 1983, “Pulsing Techniques for Solid-Propellant Rocket Motors: Modeling and Cold-Flow Testing,” J. Spacecr. Rockets, **20**(2), pp. 150-157.

Baum, J.D., Levine, J.N. and Lovine, R.L., 1988, “Pulsed Instability in Rocket Motors: A Comparison between Predictions and Experiments,” J. Prop. Power, **4**(4), pp. 308-316.

Bellucci, V., Flohr, P., Paschereit, C. O., and Magni, F., 2004, “On the Use of Helmholtz Resonators for Damping Acoustic Pulsations in Industrial Gas Turbines,” J. Eng. Gas Turbines Power, **126**, pp. 271-275.

Bloxsidge, G. J., Dowling, A. P., Hooper, N. and Langhorne, P. J., 1988, “Active Control of Reheat Buzz,” AIAA J., **26**, pp. 783-790.

Caraeni, D., Bergstrom, C. and Fuchs, L., 2000, “Modeling of Liquid Fuel Injection, Evaporation and Mixing in a Gas Turbine Burner Using Large Eddy Simulations,” Flow Turbul. Combust., **65**, pp. 223-244.

Cash, J. R. and Karp, A. H., 1990, “A Variable Order Runge-Kutta Method for Initial Value Problems with rapidly Varying Right-hand Sides,” ACM Trans. Math. Softw., **16**, pp. 201-222.

Chen, G., 2000, *Controlling Chaos and Bifurcation in Engineering Systems*, CRC Press, New York.

Chen, S. and Billings, S. A., 1989, “Representations of Non-linear Systems: The NARMAX Model,” Int. J. Control, **49**, pp. 1013-1032.

Chiang, C. H. and Sirignano, W. A., 1993, “Interacting, Convecting, Vaporizing Fuel Droplets with Variable Properties,” Int. J. Heat Mass Transfer, **36**, pp. 875-886.

Chu, B. T., 1965, “On the Energy Transfer to Small Disturbances in Fluid Flow (Part I),” Acta Mech., **1**(3), pp. 215–234.

Cohen, J. M., Banaszuk, A., Hibshman, J. R., Anderson, T. J. and Alholm, H. A., 2008, “Active Control of Pressure Oscillations in a Liquid-Fueled Sector Combustor,” J. Eng. Gas Turbines Power, **130**(5), pp. 051502-1-8.

Coker, A., Neumeier, Y., Zinn, B. T., Menon, S. and Lieuwen, T., 2006, “Active Instability Control Effectiveness in a Liquid Fueled Combustor,” Combust. Sci. Technol., **178**(7), pp. 1251-1261.

Conrad, T., Bibik, A., Shcherbik, D., Lubarsky, E. and Zinn, B. T., 2007, “Feasibility of “Intermittent” Active Control of Combustion Instabilities in Liquid Fueled Combustors using a “Smart” Fuel Injector,” Proc. Combust. Inst., **31**, pp. 2223-2230.

Courant, R., Friedrichs, K. and Lewy, H., 1967, “On the Partial Difference Equations of Mathematical Physics,” IBM J., **11**, pp. 215-234.

Crighton, D. G., Dowling, A. P., Willianms, J. E. Ffowcs, Heckl, M. and Leppington, F. G., 1992, *Modern Methods in Analytical Acoustics*: *Lecture Notes*, Springer-Verlag, London.

Crocco, L and Cheng, S. I., 1972, *Theory of Combustion Instability in Liquid Propellant Rocket Motors*, Buttersworth.

Culick, F. E. C., 1961, “High Frequency Pressure Oscillations in Liquid Rockets,” *Sc.D. Thesis*, M.I.T.

Culick, F. E. C., 1963, “High Frequency Oscillations in Liquid Rockets,” AIAA J., **1**(5), pp. 1097-1104.

Culick, F. E. C, 1976a, “Nonlinear Behaviour of Acoustic Waves in Combustion Chambers-I,” Acta Astr., **3**, pp. 715-734.

Culick, F. E. C, 1976b, “Nonlinear Behaviour of Acoustic Waves in Combustion Chambers-II,” Acta Astr., **3**, pp. 735-757.

Culick, F. E. C., 1988, *Combustion Instabilities in Liquid-fueled Propulsion Systems: an Overview*, Presented at AGARD Conf. Combust. Instabil. Liquid-Fueled Prop. Syst., Seuille-Sur-Seine, France: AGARD, NATO.

Culick, F. E. C., 1990, “Some Recent Results for Nonlinear Acoustics in Combustion Chambers,” AIAA 13th Aeroacoustics Conference, AIAA Paper 90-3927.

Culick, F. E. C. and Yang, V., 1992, “Prediction of the Stability of Unsteady Motions in Solid Propellant Rocket Motors,” *Nonsteady Burning and Combustion Stability of Solid Propellants*, edited by Deluca, L. and Summerfield, M. Vol. 143, Progress in Astronautics and Aeronautics, AIAA, Washington, DC, Chap. 18, pp. 719-780.

Culick, F. E. C. and Yang, V., 1995, “Overview of Combustion Instabilities in Liquid-Propellant Rocket Engines,” *Liquid Rocket Engine Combustion Instability*, edited by Yang, V. and Anderson, W. E., Progress in Astronautics and Aeronautics, AIAA, Washington, DC, Chap.1, pp. 3-37.

Culick, F. E. C., 2006, *Unsteady Motions in Combustion Chambers for Propulsion Systems*, RTO AGARDograph, AG-AVT-039.

Delplanque, J.-P., and Sirignano, W. A., 1993, “Numerical Study of Transient Vaporization of an Oxygen Droplet at Sub- and Super-critical Conditions,” Int. J. Heat Mass Transf., **36**, pp. 303-314.

Dowling, A. P. and Ffowcs Williams, J. E., 1983, *Sound and Sources of Sound*, Ellis Horwood.

Dowling, A. P. and Morgans, A., 2005, “Feedback Control of Combustion Oscillations,” Annu. Rev. Fluid Mech., **37**, pp. 151-182.

Dubinkin, B. N., Natanzon, M. S. and Cham'yan, A. É., 1978, “Two Regimes of Operation in a Combustion Chamber with a Recirculation Zone,” Combust. Explos., **13**, pp. 693-700.

Duvvur, A., Chiang, C. H. and Sirignano, W. A., 1996, “Oscillatory Fuel Droplet Vaporization: Driving Mechanism for Combustion Instability,” J. Propul. Power, **12**, pp. 358-365.

Eaton, J. K. and Fessler, J. R., 1994, “Preferential Concentration of Particles by Turbulence,” Int. J. Multiph. Flow, **20**, pp. 169-209.

Eldredge, J. D. and Dowling, A. P., 2003, “The Absorption of Axial Acoustic Waves by a Perforated Liner with Bias Flow,” J. Fluid Mech., **485**, pp. 307-335.

Elperin, T., and Krasovitov, B., 2006, “Transient Analysis of Sub-critical Evaporation of Fuel Droplet in Non-isothermal Stagnant Gaseous Mixtures: Effects of Radiation and Thermal Expansion,” Heat Mass Transf., **42**, pp. 427-436.

Ferziger, J. H. and Perić, M., 2002, *Computational Methods for Fluid Dynamics* (3rd Ed.), Springer.

FLUENT 6.3 User Guide, 2006, Fluent Inc, Lebanon, USA.

Franceschini, V. and Tebaldi, C., 1979, “Sequences of Infinite Bifurcations and Turbulence in a Five-mode Truncation of the Navier-Stokes Equations,” J. Stat. Phys., **21**, pp. 707-726.

Fuh, C. C. and Tsai, H. H., 2007, “Control of Discrete-time Chaotic Systems via Feedback Linearization,” Chaos, Solit. Fract., **31**, pp. 627-632.

Germano, M., Piomelli, U., Moin, P. and Cabot, W. H., 1991, “A Dynamic Subgrid-Scale Eddy Viscosity Model,” Phys. Fluids, **7**, pp. 1760-1765.

Glass, J. W. and Franchek, M. A., 1999, “NARMAX Modelling and Robust Control of Internal Combustion Engines,” Int. J. Control, **72**, pp. 289-304.

Griewank, A., Reddien, G., 1983, “The Calculation of Hopf Points by a Direct Method,” IMA J. Numer. Anal., **3**, pp. 295-304.

Gysling, D. L., Copeland, G. S., McCormick, D. C. and Proscia, W. M., 2000, “Combustion System Damping Augmentation with Helmholtz Resonators,” J. Eng. Gas Turbines Power, **122**, pp. 269-274.

Hagan, M. T., De Jesus, O. and Schultz, R., “Training Recurrent Networks for Filtering and Control,” Chapter 12 in *Recurrent Neural Networks: Design and Applications*, Medsker, L. and Jain, L.C., Eds., CRC Press, 2000, pp. 311-340.

Harrje, D. J. and Reardon, F. H. E. (Eds.), 1972, *Liquid Propellant Rocket Combustion Instability*, National Aeronautics and Space Administration, NASA SP-194.

Hathout J. P., Fleifil M., Annaswamy A. and Ghoniem A., 2002, “Combustion Instability Active Control using Periodic Fuel Injection,” J. Propul. Power, **18**, pp. 390-399.

He, L. and Clavin, P., 1993, “Premixed Hydrogen-oxygen Flames (Part II): Quasi-isobaric Ignition near the Flammability Limits,” Combust. Flame, **93**, pp. 408-420.

Heckl, M. A. and Howe, M. S., 2007, “Stability Analysis of the Rijke Tube with a Green’s Function Approach,” J. Sound Vibr., **305**, pp. 672-688.

Hinze, J. O., 1975, *Turbulence*, McGraw-Hill.

Hsieh, K. C., Shuen, J. S. and Yang, V., 1991, “Droplet Vaporization in High-pressure Environments. I: Near-critical Conditions,” Combust. Sci. Technol., **76**, pp. 111-132.

Holodniok, M. and Kubíček, M., 1984, “New Algorithms for the Evaluation of Complex Bifurcation Points in Ordinary Differential Equations: A Comparative Numerical Study,” Appl. Math. Comput., **15**, pp. 261-274.

Holmes, D. G. and Connel, S. D., 1989, “Solution of the 2D Navier-Stokes Equations on Unstructured Adaptive Grids,” Presented at the AIAA 9th Computational Fluid Dynamics Conference.

Huang, Y., Wang, Z. and Zhou, J., 2002, “Nonlinear Theory of Combustion Stability in Liquid Engine Based on Chemistry Dynamics,” Sci. China Ser. A-Math., **45**, pp. 373–383.

Huang, Y., Sung, H.-G, Hsieh, S.-Y. and Yang, V., 2003, “Large-Eddy Simulation of Combustion Dynamics of Lean-Premixed Swirl-Stabilized Combustor,” J. Propul. Power, **19**(5), pp. 782-794.

Huang, Y. and Yang, V., 2004, “Bifurcation of Flame Structure in a Lean-premixed Swirl-stabilized Combustor: Transition from Stable to Unstable Flame,” Combust. Flame, **136**, pp. 383-389.

Huang, Y. and Yang, V., 2005, “Effect of swirl on combustion dynamics in a lean-premixed swirl-stabilized combustor,” Proc. Combust. Inst., **30**(2), pp. 1775-1782.

Hubbard, G. L., Denny, V. E. and Mills, A. F., 1975, “Droplet Evaporation: Effects of Transients and Variable Properties,” Int. J. Heat Mass Transf., **18**, pp. 1003-1008.

Jorgensen, D. V. and Rutherford, A., 1983, “On the Dynamics of a Stirred Tank with Consecutive Reactions,” Chem. Eng. Sci., **38**, pp. 45-53.

Joshi, N., Epstein, M., Durlak, S., Marakovits, S. and Sabla, P., 1994, “Development of a Fuel Air Premixer for Aero-Derivative Dry Low Emissions Combustors,” Presented at Conf. No. 94-GT-253, The Hague. New York: ASME.

Kim, W. W. and Menon, S., 1995, “A New Dynamic One-Equation Subgrid-Scale Model for Large Eddy Simulations,” AIAA-95-0356.

Kim, W. W., Menon, S. and Mongia, H. C., 1999, “Large-Eddy Simulation of a Gas Turbine Combustor Flow,” Combust. Sci. Technol., **143**(1), pp. 25-62.

Kubíček, M., Holodniock, M., 1984, “Evaluation of Hopf Bifurcation Points in Parabolic Equations Describing Heat and Mass Transfer in Chemical Reactors,” Chem. Eng. Sci., **39**, pp. 593-599.

Lamb, H., 1945, *Hydrodynamics* (6th Ed.), Dover Publications, New York.

Lang, W., Poinsot, T. and Candel, S., 1987, “Active Control of Combustion Instability,” Combust. Flame, **70**, pp. 281-289.

Langhorne, P. J., Dowling, A. P. and Hooper, N., 1990, “Practical Active Control System for Combustion Oscillations,” J. Propul. Power, **6**, pp. 324-333.

Lee, J.–Y., Lubaarsky, E. and Zinn, B. T., 2005 ““Slow” Active Control of Combustion Instabilities by Modification of Liquid Fuel Spray Properties,” Proceed. Combust. Inst., **30**, pp. 1757-1764.

Lefebvre, A. H., 1989, *Atomization and Sprays*, Hemisphere Publishing Corp., New York.

Lei, S. and Turan, A., 2009a, “Nonlinear/Chaotic Behaviour in Thermo-acoustic Instability,” Combust. Theory Model., **13**, pp. 541-557.

Lei, S. and Turan, A., 2009b, “Nonlinear/Chaotic Analysis, Modelling and Control of Combustion Instabilities due to Vaporizing Sprays,” Chaos Solitons Fractals, **42**, pp. 1766-1779.

Lei, S. and Turan, A., 2010a, “Chaotic Modelling and Control of Combustion Instabilities Due to Vaporization,” Int. J. Heat Mass Transf., in print, 10.1016/j.ijheatmasstransfer.2010.06.045.

Lei, S. and Turan, A., 2010b, “Nonlinear/Chaotic Modelling and Control of Combustion Instabilites,” Int. J. Bifurcation Chaos, **20**(4), pp. 1245-1254.

Lei, S. and Turan, A., 2010c, “Identification and Control of Combustion Instabilities using Neural Networks,” J. Propul. Power, submitted.

Levine, J. N. and Baum, J. D., 1981, “A Numerical Study of Nonlinear Instability Phenomena in Solid Rocket Motors,” AIAA-81-1524.

Lieuwen, T., 2002, “Experimental Investigation of Limit Cycle Oscillations in an Unstable Gas Turbine Combustor,” J. Propul. Power, **18**, pp. 61-67.

Lieuwen T. C. and Yang, V. (Eds.), 2005, *Combustion Instability in Gas Turbine Engines*: *Operational Experience*, *Fundamental Mechanisms, and Modeling*, Progress in Astronautics and Aeronautics, AIAA.

Lilly, D. K., 1966, “On the Application of the Eddy Viscosity Concept in the Inertial Subrange of Turbulence,” NCAR Manuscript 123.

Liu, A. B., Mather, D. and Reitz, R. D., 1993, “Modeling the Effects of Drop Drag and Breakup on Fuel Sprays,” SAE Technical Paper 930072.

Liu, S. T. and Chen, G., 2004, “Nonlinear Feedback-controlled Generalized Synchronization of Spatial Chaos,” Chaos, Solit. Fract., **22**, pp. 35-46.

Lord Rayleigh, 1878, *The theory of sound*, Dover Publication, New York, 1945, Vol. II, pp. 227.

Lynch, S., 2004, *Dynamical systems with applications using MATLAB*, Birkhauser, Boston.

Lynch, S., 2005, “Analysis of a Blood Cell Population Model,” Int. J. Bifurcation Chaos, **15**, pp. 2311-2316.

Mathews, J. H., 1992, *Numerical Methods for Mathematics*, *Science and Engineering* (2nd ed.), Prentice Hall International, London.

Martin, C. E., Benoit, L. and Sommerer, Y., 2006, "Large-Eddy Simulation and Acoustic Analysis of a Swirled Staged Turbulent Combustor," AIAA J., **44**(4), pp. 741-750.

Maxey, M. R. and Patel, B. K., 2001, "Localized Force Representations for Particles Sedimenting in Stokes Flow," Int. J. Multiph. Flow, **27**, pp. 1603-1626.

McIntosh, A. C. and Rylands, S., 1996, "A Model of Heat Transfer in Rijke Tube Burners," Combust. Sci. Technol., **113**, pp. 273-289.

Menon, S. and Patel, N., 2006, "Subgrid Modeling for Simulation of Spray Combustion in Large-Scale Combustors", AIAA J., **44**(4), pp. 709-723.

Moin, P. and Apte, S. V., 2006, "Large-Eddy Simulation of Realistic Gas Turbine Combustors," AIAA J., **44**, pp. 698-708.

Morgans, A. S. and Stow, S. R., 2007, "Model-based Control of Combustion Instabilities in Annular Combustors," Combust. Flame, **150**(4), pp. 380-399.

Morgans, A. S. and Annaswamy, A. M., 2008, "Adaptive Control of Combustion Instabilities for Combustion Systems with Right-Half Plane Zeros," Combust. Sci. Technol., **180**(9), pp. 1549-1571.

Narendra, K. S., and Mukhopadhyay, S., 1997, "Adaptive Control Using Neural Networks and Approximate Models," IEEE Trans. Neural Netw., **8**, pp. 475-485.

Natanzon, M. S. and Men'shikova, O. M., 1992, "Bifurcation of Steady Combustion Regimes and Teir influence on the Onset of High-frequency Oscillations in Combustion Chambers," Combust. Explos., **28**, pp. 326-333.

Nicoud, F. and Ducros, F., 1999, "Subgrid-Scale Stress Modelling based on the Square of Velocity Gradient Tensor," Flow Turbul. Combust., **62**, pp. 183-200.

O'Rourke, J. and Amsden, A. A., 1987, "The TAB Method for Numerical Calculation of Spray Droplet Breakup," SAE Technical Paper 872089, SAE.

Ott, E., Grcbogi, C. and Yorke, J. A., 1990, “Controlling Chaos,” Phys. Rev. Lett., **64**, pp. 1196-1199.

Paschereit, C. and Gutmark, E., 2008, “Combustion Instability and Emission Control by Pulsating Fuel Injection,” J. Turbomach, **130**, pp. 011012-1-8.

Patankar, S. V., 1980, *Numerical Heat Transfer and Fluid Flow*, McGraw-Hill, New York.

Poinsot, T. and Veynante, D., 2005, Theoretical and numerical combustion (2nd Ed.), Edwards, Inc, Philadelphia, PA.

Poling, B. E., Prausnitz, J. M. and O’Connell, J. P., 2001, *The Properties of Gases and Liquids* (5th Ed.), McGRAE-HILL, London.

Pope, S. B., 2000, *Turbulent Flows*, Cambridge University Press.

Putnam, A., 1971, *Combustion Driven Oscillations in Industry*, American Elsevier Pulbishers, New York, NY.

Rauch, R. D., Batira, J. T. and Yang, N. T. Y., 1991, “Spatial Adaption Procedures on Unstructured Meshes for Accurate Unsteady Aerodynamics Flow Computations,” Technical Report, AIAA-91-1106.

Richards, G. A. and Janus, M. C., 1998, “Characterization of Oscillations during Premix Gas Turbine Combustion,” J. Eng. Gas Turbines Power, **120**, pp. 294-302.

Richards, G. A., Straub, D. L. and Robey, E. H., 2003, “Passive Control of Combustion Dynamics in Stationary Gas Turbines,” J. Prop. Power, **19**(5), pp. 795-810.

Richards, G. A., Thornton, J. D., Robey, E. H. and Arellano, L., 2007, “Open-Loop Active Control of Combustion Dynamics on a Gas Turbine Engine,” J. Eng. Gas Turbines Power, **129**, pp. 38-48.

Roose, D. and Hlaváček, V., 1983, “A New Approach for the Computation of Hopf Bifurcation Points,” SIAM J. Appl. Math., **43**, pp. 1075-1085.

Roose, D., Piessens, R., Hlaváček, V. and van Rompay, 1984, “Direct Evaluation of Critical Conditions for Thermal Explosion and Catalytic Reaction,” Combust. Flame, **55**, pp. 323-329.

Roux, S., Lartigue, G., Poinsot, T., Meier, U. and Bérat, C., 2005, “Studies of Mean and Unsteady Flow in a Swirled Combustor using Experiments, Acoustic Analysis, and Large Eddy Simulations,” Combust. Flame, **141**, pp. 40-54.

Roux, A., Gicquel, L., Sommerer, Y. and Poinsot, T., 2008, “Large Eddy Simulation of Mean and Oscillating Flow in a Side-dump Ramjet Combustor,” Combust. Flame, **152**, pp. 154-176.

Salarieh, H. and Alasty, A., 2008, “Stabilizing Unstable Fixed Points of Chaotic Maps via Minimum Entropy Control,” Chaos, Solit. Fract., **37**, pp. 763-769.

Sattinger, S., Neumeier, Y., Nabi, A., Zinn, B. T., Amos, D. and Darling, D., 2000, “Sub-scale Demonstration of the Active Feedback Control of Gas-turbine Combustion Instabilities,” Transact ASME, **122**, pp. 262-268.

Sazhin, S., 2006, “Advanced Models of Fuel Droplet Heating and Evaporation,” Prog. Energy Combust. Sci., **32**, pp. 162-214.

Sazhin, S., Krutitskii, P., Abdelghaffar, W., Mikhalovsky, S., Meikle, S. and Heikal, M., 2004, “Transient Heating of Diesel Fuel Droplet,” Int. J. Heat Mass Transf., **47**, pp. 3327-3340.

Schmitt, P., Poinsot, T., Schuermans, B. and Geigle, K. P., 2007, “Large-Eddy Simulation and Experimental Study of Heat Transfer, Nitric Oxide Emissions and Combustion Instability in a Swirled Turbulent High-Pressure Burner,” J. Fluid Mech., **570**, pp. 17-46.

Selle, L., Lartigue, G., Poinsot, T., Koch, R., Schildmacher, K. –U., Krebs, W., Prade, B., Kaufmann, P. and Venante, D., 2004, “Compressible Large Eddy Simulation of Turbulent Combustion in Complex Geometry on Unstructured Meshes,” Combust. Flame, **137**, pp. 489-505.

Selle, L., Benoit, L., Poinsot, T., Nicoud, F. and Krebs, W., 2006, “Joint Use of Compressible Large-Eddy Simulation and Helmholtz Solvers for the Analysis of Rotating Modes in an Industrial Swirled Burner,” Combust. Flame, **145**, pp. 194-205.

Seydel, R., 1994, *Practical Bifurcation and Stability Analysis*: *From Equilibrium to Chaos* (2nd ed.), Springer-Verlag Inc., New York.

Sirignano, W. A., Delplanque, J. -P., Chiang, C. H., and Bhatia, R., 1994, “Liquid-Propellant Droplet Vaporization: A Rate-Controlling Process for Combustion Instability,” *Liquid Rocket Engine Combustion Instability*, edited by Yang, V. and Anderson, W. E., Progress in Astronautics and Aeronautics, AIAA, Washington, DC, 1995, Chap.11, pp. 307-343.

Sirignano, W. A., 1999, *Fluid Dynamics and Transport of Droplets and Sprays*, Cambridge University Press.

Smagorinsky, J., 1963, “General Circulation Experiments with Primitive Equations. I. The Basic Experiments,” Mon. Weather Rev., **91**, pp. 99-164.

Smith, C. B., Kuszta, B., Lyberatos, G. and Bailey, J. E., 1983, “Period Doubling and Complex Dynamics in an Isothermal Chemical Reaction System,” Chem. Eng. Sci., **38**, pp. 425-430.

Sohn, C. H., Kim, J. S., Chung, S. H. and Maruta, K., 2000, “Nonlinear Evolution of Diffusion Flame Oscillations Triggered by Radiative Heat Loss,” Combust. Flame, **123**, pp. 95-106.

Sommerfeld, M. and Qiu, H. H., 1998, “Experimental Studies of Spray Evaporation in Turbulent Flow,” Int. J. Heat Mass Transf., **19**, pp. 10-22.

Steele, R. C., Cowell, L. H., Cannon, S. M. and Smith, C. E., 2000, “Passive Control of Combustion Instability in Lean Premixed Combustors,” J. Eng. Gas Turbines Power, **122**, pp. 412-419.

Sterling, J. D., 1993, “Nonlinear Analysis and Modelling of Combustion Instabilities in a Laboratory Combustor,” Combust. Sci. Technol., **89**, pp. 167-179.

Strahle, W., 1960, “Unsteady Laminar Jet Flames at Large Frequencies of Oscillation,” AIAA J., **3**, pp. 957-960.

Taylor, G. I., 1963, “The Shape and Acceleration of a Drop in a High Speed Air Stream,” Technical report, In the Scientific Papers of Taylor, ed., G. K. Batchelor, 1963.

Tong, A. Y. and Sirignano, W. A., 1989, “Oscillatory vaporization of fuel droplets in an unstable combustor,” J. Propul. Power, **5**, pp. 257-261.

Tsien, H. S., 1952, “Servo-Stabilization of Combustion in Rocket Combustion,” ARS J., **22**, pp. 256-263.

Turns, S. R., 2000, A*n Introduction to Combustion*: *Concepts and Applications*, McGRAW-HILL, New York.

Van Leer, B., 1979, “Toward the Ultimate Conservative Difference Scheme. IV. A Second Order Sequel to Godunov’s Method,” J. Comput. Phys., **32**, pp. 101-136.

Van Doormaal, J. P. and Raithby, G. D., 1984, “Enhancements of the SIMPLE Method for Predicting Incompressible Fluid Flows,” Numer. Heat Transfer, **7**, pp. 147-163.

Vuillot, F. and Lupoglazoff, N., 1991, “Two-dimensional Numerical Simulation of the Stability of a Solid Propellant Rocket Motor,” In: Proc. AIAA 29th Aerospace Sciences MeetingReno, NV, Jan. 7-10, AIAA, New York, Paper 91-0205 .

Wang, T., 1997, “Modeling of Combustion Dynamics in Gas Turbine Engines,” *Ph.D. Thesis*, The Penn State University.

Yang, V., Kim, S.-I., Culick, F. E. C, 1987, “Third-Order Nonlinear Acoustic Waves and Triggering of Pressure Oscillations in Combustion Chambers, Part I: Longitudinal Modes,” AIAA Paper 87-1973.

Yang, V., Kim, S.-I., Culick, F. E. C, 1988, “Third-Order Nonlinear Acoustic Waves and Triggering of Pressure Oscillations in Combustion Chambers, Part I: Transverse Modes,” AIAA Paper 88-0152.

Yang, V., Kim, S.-I., Culick, F. E. C, 1990, “Triggering of Longitudinal Pressure Oscillations in Combustion Chambers, I: Nonlinear Gasdynamics,” Combust. Sci. Technol., **72**, pp. 183-214.

Yang, V., Wicker, J. M. and Yoon M. W., 1995, “Acoustic Waves in Combustion Instability,” *Liquid Rocket Engine Combustion Instability*, edited by Yang, V. and Anderson, W. E., Progress in Astronautics and Aeronautics, AIAA, Washington, DC, Chap.1, pp. 357-376.

Yi, T. and Gutmark, E. J., 2008, “Adaptive Control of Combustion Instability Based on Dominant Acoustic Modes Reconstruction,” Combust. Sci. Technol., **180**, pp. 249-263.

Yue, H. and Wang, H., 2003, “Minimum Entropy Control of Closed-loop Tracking Errors for Dynamic Stochastic Systems,” IEEE Trans. Automat. Control, **48**, pp. 118-122.

Zeng Y. and Lee C., 2002, “A Preferential Vaporization Model for Multicomponent Droplets and Sprays,” Atom. Sprays, **12**, pp. 163-186.